A TWO PARAMETER CHARACTERIZATION OF EDGE CRACKED NITI SHAPE MEMORY ALLOY UNDER PLANE STRAIN CONDITIONS

by

Oğuzhan Fikri Merde

B.S., Mechanical Engineering, İhsan Doğramacı Bilkent University, 2018

Submitted to the Institute for Graduate Studies in
Science and Engineering in partial fulfillment of
the requirements for the degree of
Master of Science

Graduate Program in Mechanical Engineering
Boğaziçi University

2022

ACKNOWLEDGEMENTS

I would like to express my gratitude and deepest appreciation to my supervisor, Sertan Alkan, who guided me throughout this project. I'm so thankful for his guidance and persistent help for this dissertation. I would also like to thank my friends and especially my family who supported me and gave me the encouragement I needed throughout the study.

ABSTRACT

A TWO PARAMETER CHARACTERIZATION OF EDGE CRACKED NITI SHAPE MEMORY ALLOY UNDER PLANE STRAIN CONDITIONS

Shape memory alloys (SMAs) are metallic systems that exhibit reversible, diffusionless, martensitic phase transformation. Employing finite element analyses, the stress fields and crack tip constraints generated are examined for a NiTi SMA which exhibits superelastic behavior. For this purpose, a single edge cracked configuration satisfying plane strain conditions is subjected to uniform loading. Both pure Mode I and mixed mode (Mode I + Mode II) configurations are elaborated by changing the crack inclination angle. As a novel step, a multi-parameter fracture mechanics approach is adapted to characterize the dependence of stress field components on both asymptotic $r^{-1/2}$ and radial r^o terms around the crack tip. This task is accomplished by generating closed-form fitting expressions for stress components via nonlinear least-square regression of the full field data from finite element analyses. It has been shown that r^o term plays a significant role on the stress field around the crack tip in NiTi SMAs.

In characterization of crack tip constraint in NiTi, stress triaxiality parameter, Q, is utilized in the present work. To quantify the behavior of Q, the material characteristics of NiTi such as transformation start and end stresses, hardening modulus and transformation strain are varied under both pure Mode I and mixed mode configurations. The results show that martensitic transformation has an effect of stress constraint relaxation effect reflected by the decrease of Q parameter. Meanwhile promotion of transformation start stress is found to have a strong contribution in constraining crack tip, the transformation end stress is observed to have negligible effect.

ÖZET

KENAR ÇATLAKLI NITI ŞEKİL HAFIZALI ALAŞIMIN DÜZLEMSEL GERİNİM ALTINDA İKİ PARAMETRELİ KARAKTERİZASYONU

Şekil hafızalı alaşımlar; tersinir, yayınımdan bağımsız, martensit faz dönüşümü gösteren metalik alaşımlardır. Bu çalışmada, sonlu elemanlar analizi kullanılarak süperelastik NiTi şekil hafızalı alaşımda çatlak ucu gerilmesi ve kısıtlaması tetkik edilmiştir. Bu amaçla kenar çatlaklı düzlemsel gerinim şartlarını sağlayan bir numune homojen dağılımlı uzak gerilme alanına tabi tutulmuştur. Hem Mod I hem de karışık modlu (Mod I + Mod II) yükleme rejimi incelenmiştir. Kırılma mekaniğinin çoklu-parametre yaklaşımıyla çatlak ucu gerilmelerinin asimptotik $r^{-1/2}$ ve radyal r^o terimlerine bağıntısı irdelenmiştir. En küçük kareler prensibiyle doğrusal olmayan regresyon metodu, sonlu elemanlar verisi kullanılarak çatlak ucu gerilmelerinin kapalı form olarak ifade edilmesinde kullanılmıştır. r^o teriminin şekil hafızalı alaşımlarda çatlak ucu gerilmelerinin doğru ifadesinde önemli rolü olduğu gösterilmiştir.

Bu çalışmada, NiTi çatlak ucu kısıtlamasının sayısal hesaplanmasında parametre olarak üç boyutlu gerilme hali, Q, kullanılmıştır. Q parametresinin NiTi malzeme özelliklerine bağımlılığı; faz dönüşüm başlangıç ve bitiş gerilmeleri, Mod I ve karışık mod için pekleşme katsayısı ve faz dönüşüm gerinimi kontrollü değiştirilerek saptanmıştır. Sonuçlar, Q parametresinin değerinin azalması itibariyle, martensitik faz dönüşümünün çatlak ucu kısıtlamasını gevşettiğini göstermiştir. Faz dönüşüm gerilmesinin artışı çatlak ucunu daha fazla kısıtlamış, ancak faz dönüşüm bitiş gerilmesinin kısıtlama üzerine etkisi çok düşük seviye kalmıştır.

TABLE OF CONTENTS

LIST OF FIGURES

LIST OF TABLES

LIST OF SYMBOLS

α	Crack inclination angle
ϵ_{ij} (i, j = 1 , 2 , 3)	Strain tensor components
γ_s	Surface energy per unit area
γ_p	Plastic work per unit area
μ	Shear Modulus
$\mathit{\Pi}$	Cracked plate potential energy
$\mathit{\Pi}_0$	Uncracked plate potential energy
$\mathit{\Gamma}$	Closed contour
S_{AS},S_{AF},S_{MS},S_{MF}	Transformation stresses
S_f	Critical fracture stress
S_m	Mean stress
S_{ij} (i, j = 1 , 2 , 3)	Stress tensor components
S_∞	Far-field stress
$\mathit{\Theta}$	Angle set
a	Crack size
A	Projected area
A_s, A_f, M_s, M_f	Transformation temperatures
B	Thickness
E	Young's Modulus
dE	Internal strain energy
G	Griffith parameter
G_c	Critical Griffith parameter
H	Hardening Modulus
h	Height
J	J Integral
K	Stress Intensity Factor
K_{IC}	Fracture Toughness

S	Total surface area
T_i (i = 1 , 2 , 3)	Traction vector components
v	Poisson ratio
u_i (i = 1 , 2 , 3)	Displacement vector components
ds	Length increment
Q	Stress triaxiality
W	Width
W_s	Work done by surface

LIST OF ACRONYMS/ABBREVIATIONS

2D	Two Dimensional
3D	Three Dimensional
CTOD	Crack Tip Opening Displacement
SENT	Single Edge Notch Tensile
SIF	Stress Intensity Factor
SIM	Stress Induced Martensitic Transformation
SMA	Shape Memory Alloy
SME	Shape Memory Effect

1. INTRODUCTION

Shape memory alloys (SMAs) are metallic systems that exhibit reversible diffusionless, martensitic phase transformation. Essentially, in martensitic phase transformation, a high-symmetry austenite phase favors a low-symmetry martensitic phase via mechanical or thermal stimulus [1]. Typical shape memory alloys can be listed as NiTİ, CuZn, CuZnAl, NiCuAl, NiTiCu etc. [2]. They find a vast range of application fields such as biomedical, aerospace, automotive and construction industries. Among them: cardiovascular stents, turbine nozzles, dual shock absorbers can be listed [3]. Therefore, to characterize the performance of SMAs standsout as an important problem in material and mechanical engineering fields.The working regime of SMAs are characterized by four specific temperatures which are called transformation temperatures (A_s, A_f, M_s, M_f). A_s is the austenite start temperature and A_f is austenite finish temperature whereas M_s is martensite start temperature and M_f stands for martensite finish temperature [4]. Below M_f temperature, SMA systems favor a self-accommodated, multi-variant microstructure in which the variants are originated from the same austenite crystal structure but exhibit different orientations in the martensite crystal. If there is no applied load in martensitic phase but only temperature stimulus, self-accommodation of multiple martensitic variants leads to no macroscopic strain change [5]. With applied loading under constant temperature, these variants promote to a single variant via reorientation and/or detwinning mechanisms which result in macroscopic strain. Subsequently, heating an SMA to a temperature above A_s, the martensite phase transforms back to austenite phase and a significant transformation strain, on the order of 2-10 percentage depending on the alloy system, is recovered. This mechanism is named as shape memory effect (SME) or one-way memory effect [10]. In a closely related phenomenon, namely two-way shape memory effect, SMAs subjected to a previous thermomechanical training cycle, favor a single variant under sole stimulus of temperature unlike self-accomadating structure. The resulting microstructure still exhibits shape recovery if transformation is driven back to austenite by heating above A_s [7].

There is also another transformation mechanism driven by applied loading at a temperature regime greater than A_f which is named as pseudoelasticity. Pseudoelasticity is a significant concept associated with stress-induced transformation and results in stress-induced martensite accompanied by a substantial transformation strain favoring one or two variants depending on the alloy system. Upon unloading, the reverse transformation from martensite to austenite tends to recover the transformation strain [8]. In the next section, these transformation mechanisms will be detailed.

1.1. Shape Memory Effect

A typical closed thermomechanical path 1-2-3-4-1, exemplifying SME is shown in Figure 1.1.

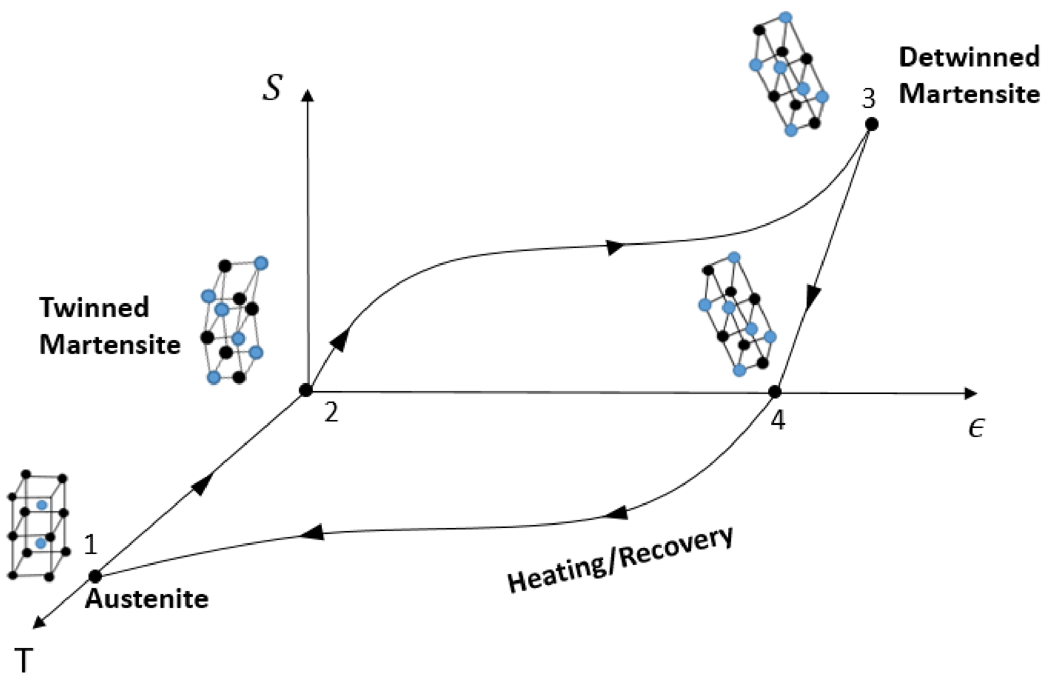

Figure 1.1. Stress strain temperature schematic of the crystallographic changes involved in the shape memory effect.

As can be seen, starting with an initially austenite phase and subsequently cooling it along the path (1-2), SMA transforms to twinned martensite (although there are some exceptions) under the effect of temperature change (self-accommodated structure) with no macroscopic strain. Subsequently, if SMA is loaded via (2-3) path, the applied load at constant temperature initiates stress induced martensitic transformation and introduces significant strain. In this particular configuration, the microstructure is composed of a single variant consuming the other variants. The resulting microstructural phase is denoted as detwinned martensite. As the very same SMA is unloaded by following path (3-4), detwinned martensite is conserved and the corresponding strain is not recovered except the elastic part. Completing the cycle by heating above A_f following (4- 1), the material favors austenite phase again and the detwinning strain is usually recovered at a high extent [6]. This distinguishing property to accommodate deformation reversibly is called one-way shape memory effect (SME) and employed in sensor technologies successfully [10].

1.2. Two-Way Shape Memory Effect

Meanwhile, the two-way shape memory effect is very similar to one-way shape memory effect, it differs by a thermomechanical training cycle before point I of Figure 1.1. To exemplify this, at a constant temperature (70^o C), $Ni_{50}Ti_{50}$ (at. %) is subjected to tensile loading cycle which is reported to exhibit single variant martensite structure upon release of loading and lowering temperature below M_f unlike conventional SMAs which exhibit multi-variant structure [12]. In contrast to conventional SMA samples, this particular sample exhibits a macroscopic transformation strain by favoring a single variant upon cooling below M_f instead of self-accommodated microstructure which induces no macroscopic strain. This sample still exhibits shape recovery up on heating above A_s as in one-way SME. Based on this fact, the corresponding property is distinguished as two-way shape memory effect. It is important to design training conditions properly in achieving the desired SMA performance due to the fact that either insufficient or over-training cycles lead to poor two-way SME [13].

1.3. Pseudoelasticity

Pseudo elasticity is the property of SMAs to undergo a reversible stress-induced martensitic transformation at a constant ambient temperature above A_f [14]. As illustrated in Figure 1.2, applied load at an initially austenitic sample promotes austenite-martensite transformation at martensite start stress level denoted by S_{MS}. The transformation introduces substantial transformation strain (on the order of 2-6 %) in general identified by the region between B point and C point in Figure 1.2. The microstructure is transferred to martensite completely at point C corresponding to martensite finish stress, S_{MF}. Note that, elastic deformation of martensite is observed up on further loading above S_{MF} till plastic yielding. During unloading, the reverse transformation initiates at the critical austenite start stress, S_{AS} (point E) and completes at austenite finish stress, S_{AF} (point F). At the end of the cycle A-B-C-D-E-F-A, the resulting crystal structure favors austenite phase again with a substantial recovery of transformation strain [15]. This phase transformation process exhibits a stress hysteresis, commonly defined as the difference between the stress levels corresponding to 50 percentage martensite volume fraction during forward and reverse transformation reactions reflecting the energy dissipated throughout the cycle. In the next section, in order to establish a strong background for the present proposal statement focusing on fracture response of SMAs, as its title supplies, fundamental concepts in fracture mechanics will be revisited. First of all, Griffith energy balance is described and examined under equilibrium conditions. Following this trend, modified Griffith equation is explained. Further on, the goals of the present work will be detailed.

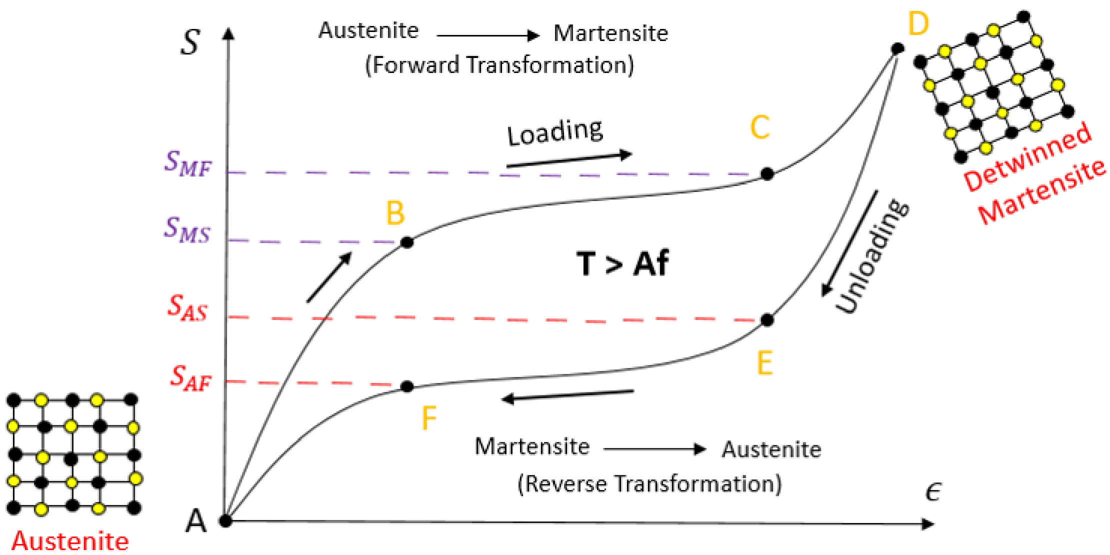

Figure 1.2. Schematic stress-strain curve of super elastic shape memory alloy

2. A REVISIT TO FUNDAMENTAL CONCEPTS IN FRACTURE MECHANICS

2.1. Griffith Energy Balance

Mathematically, crack formation is associated with the removal of the surface tractions acting on crack surfaces. Under quasi-static equilibrium conditions, the total energy change of a closed system including both cracked material and applied loading is zero [17]. From the thermodynamical perspective, critical fracture condition is described as the point where crack grows under equilibrium conditions without any further change in total energy, E. The early studies on fracture mechanics have started with Inglis and Griffith [18,19]. The study of Griffith on glass whiskers have established the underlying energy criterion on crack extension [18]. The subsequent subsection focuses on the energy balance conditions for crack advance under equilibrium quantitatively based on this early literature [19].

2.2. Griffith Energy Balance Under Equilibrium

Consider a plate of width thickness (B=1) that contains a crack of length 2a under constant far field stress, as shown in Figure 2.1. For this 2-D case,plate dimensions are assumed to be much greater than crack size. For stable crack growth, potential energy associated with internal strain energy and applied loading should be sufficient enough to overcome surface energy of the material. Then, the energy balance for an incremental projected crack area growth, dA, under equilibrium conditions can be formulated based on the work of Griffith as

$$\frac{dE}{dA} = \frac{d\Pi}{dA} + \frac{dW_s}{dA} = 0, \tag{2.1}$$

where W_s represents the work required to create the new crack surfaces with extension.

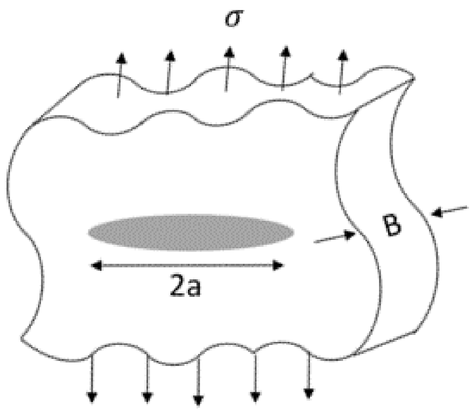

Figure 2.1. A through-thickness crack in an infinitely wide plate subjected to a remote tensile stress.

At this stage, the projected area, A, of the crack is expressed as

$$A = 2aB. \tag{2.2}$$

The total surface area, T_A, of the crack is expressed as

$$T_A = 4aB. \tag{2.3}$$

In order to calculate the critical levels of energy transferred or stress field generated for the system to initiate crack extension, we need precise knowledge on the potential energy stored in the system. However, in general this is a difficult task requiring numerical techniques. On the other hand, in this section, we want to focus on the particular case shown in Figure 2.1 for which Inglis introduced an analytical solution. Note that, this approach assumes linear elastic, homogeneous, isotropic material behavior. Then, the potential energy of the system shown in Figure 2.1 is given explicitly as

$$\mathit{\Pi} = \mathit{\Pi}_0 - \frac{\mathit{\Pi} S^2 a^2 B}{E}. \tag{2.4}$$

In this equation, $\mathit{\Pi}_0$ is uncracked plate potential energy and E is Young's Modulus. Since crack formation requires two new surfaces created, W_s term is expressed as

$$W_s = \frac{4aB}{\gamma_s}, \tag{2.5}$$

where γ_s is the surface energy per unit area and related with W_s as such

$$\gamma_s = \frac{W_s}{T_A}. \tag{2.6}$$

As we focus on infinitesimal crack extension, differentiating W_s term leads to

$$dW_s = 4\gamma_s Bda. \tag{2.7}$$

Therefore, the rate of change in W_s with respect to the projected area A is expressed as

$$\frac{dW_s}{dA} = \frac{(4\gamma_s Bda)}{(2Bda)}. \tag{2.8}$$

For unit thickness (B=1), equation (2.8) is simplified to

$$\frac{dW_s}{dA} = 2\gamma_s. \tag{2.9}$$

Then, as the uncracked potential energy, $\mathit{\Pi}_0$ does not change with crack extension, the potential energy release rate $\frac{-d\mathit{\Pi}}{dA}$ is expressed as

$$\frac{-d\mathit{\Pi}}{dA} = \frac{\pi S^2 a}{E}. \tag{2.10}$$

Therefore, following Griffith energy balance leads to the condition

$$\frac{-d\mathit{\Pi}}{dA} = \frac{dW_s}{dA}. \tag{2.11}$$

This equation dictates that the potential energy release rate with crack extension must be equal to the crack surface energy formation rate. In Griffith approach, a single parameter G is introduced to capture $\frac{-d\Pi}{dA}$ term. Based on this perspective, the crack propagation is governed by the critical level G, namely G_c. For the given particular example, the far-field applied load level promoting G to G_c level corresponds to a far-field stress of $S = S_f$ which is explicitly given as

$$S_f = (\frac{2E\gamma_s}{\pi a})^{1/2}. \tag{2.12}$$

2.3. Modified Griffith Equation

Theoretically, equation (2.12) is valid only for ideally brittle solids in which plastic effects are neglected. Thus, Orowan and Irwin modified Griffith equation for materials that exhibit plastic flow [20,21]. Derivation of a critical fracture stress, S_f, for metals exhibiting plasticity is extended as

$$S_f = (\frac{2E(\gamma_p + \gamma_s)}{\pi a})^{1/2}, \tag{2.13}$$

where γ_p (plastic work per unit area) term is included to capture crack tip plasticity. In fact, modified Griffith equation can be generalized for any type of energy dissipation as expressed

$$S_f = (\frac{2Ew_f}{\pi a})^{1/2}, \tag{2.14}$$

where w_f stands for the combination of energy terms related to plastic, viscoelastic, viscoplastic effects depending on the material type. By appropriate modification, other energy dissipative phenomena such as martensitic transformation can be also incorporated into the model. On the other hand, quantification of the related energy terms is a formidable task and needs elaborate experimental and numerical techniques.

The elastic stress field approach of stress intensity factor is taken into account for linear elastic, homogeneous materials and this fracture mechanics theory is examined elaborately in the following chapter.

2.4. Stress Intensity Factor Approach:

Up on evaluation of the fracture mechanics theory, following Inglis and Griffith [18,19]; Westergaard [22], Williams [23,24] and Irwin [21] have put forward efforts to designate an approach which can capture the stress field generated ahead of the crack tip. To achieve this task, asymptotic techniques within the scope of linear elasticity theory is adopted to cracked bodies in which case the crack tip is regarded as a geometric singularity. Within this framework, the possible loading configurations acting far-field on the cracked samples are classified into three modes: Mode I (opening), Mode II (sliding) and Mode III (tearing) as illustrated in Figure 2.2.

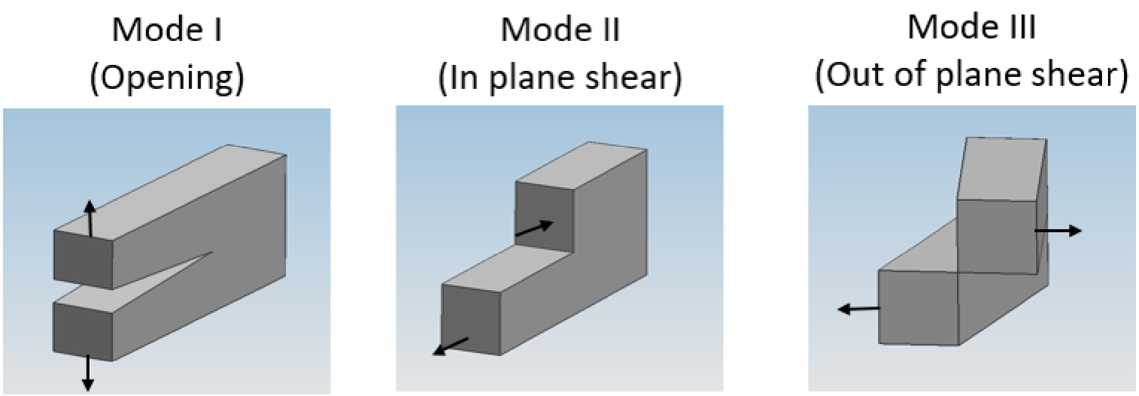

Figure 2.2. Three loading modes of crack surface displacements.

Near the crack tip, each loading mode generates the $1/\sqrt{r}$ singularity at the crack tip with an angular dependence, θ, captured by $f_{ij}\ (\theta)$ function based on the polar coordinate frame attached to the crack tip in Figure 2.3.

The general form of stress fields ahead of crack tip for Mode I are expressed as

$$\lim_{r\to 0} S^{I}_{ij} = \frac{K_I}{\sqrt{2\pi r}} f^{I}_{ij}(\theta). \tag{2.15}$$

The general form of stress fields ahead of crack tip for Mode II are expressed as

$$\lim_{r\to 0} S_{ij}^{II} = \frac{K_{II}}{\sqrt{2\pi r}} f_{ij}^{II}(\theta). \tag{2.16}$$

The general form of stress fields ahead of crack tip for Mode III are expressed as

$$\lim_{r\to 0} S_{ij}^{III} = \frac{K_{III}}{\sqrt{2\pi r}} f_{ij}^{III}(\theta), \tag{2.17}$$

where each of the parameters K_I, K_{II}, K_{III} are denoted as stress intensity factor for the corresponding loading mode. Note that K parameter is linearly proportional to applied loading S. On the other hand, the exact relation between S and K requires the solution of the boundary value problem associated with the crack configuration at hand.

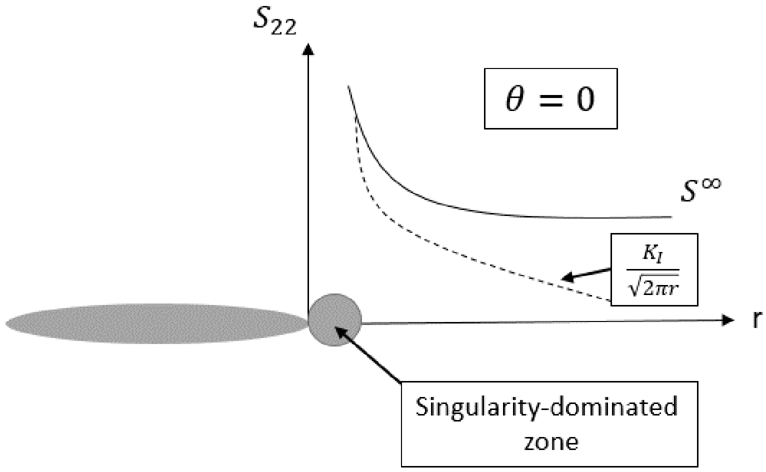

Figure 2.3. Stress normal to the crack plane S_{22} with respect to the distance from the crack tip (r).

Singular stress fields and crack tip displacements for Mode I and Mode II in linear elastic, isotropic materials are tabulated in Table 2.1 and Table 2.2 in terms of Cartesian coordinates (with origin at the crack tip).

Table 2.1. Crack tip displacement fields for modes I and II (linear, elastic materials)

	MODE I	**MODE II**
u_x	$\frac{K_I}{2\mu}\sqrt{\frac{r}{2\pi}}\cos(\frac{\theta}{2})[\kappa-1+2\sin^2(\frac{\theta}{2})]$	$\frac{K_I}{2\mu}\sqrt{\frac{r}{2\pi}}\sin(\frac{\theta}{2})[\kappa+1+2\cos^2(\frac{\theta}{2})]$
u_y	$\frac{K_I}{2\mu}\sqrt{\frac{r}{2\pi}}\sin(\frac{\theta}{2})[\kappa+1-2\cos^2(\frac{\theta}{2})]$	$-\frac{K_I}{2\mu}\sqrt{\frac{r}{2\pi}}\cos(\frac{\theta}{2})[\kappa-1-2\sin^2(\frac{\theta}{2})]$

In Table 2.1, κ is calculated by the formula of 3-4ν under plane strain conditions and (3-ν)/(1+ν) under plane stress conditions.

Table 2.2. Stress and displacement fields ahead a crack tip for modes I, II.

	Mode I	**Mode II**
(S_{xx})	$\frac{K_I}{\sqrt{2\pi r}}\cos(\frac{\theta}{2})$ [1-$\sin(\frac{\theta}{2})sin(\frac{3\theta}{2})$]	$-\frac{K_{II}}{\sqrt{2\pi r}}\sin(\frac{\theta}{2})$ [2+$\cos(\frac{\theta}{2})cos(\frac{3\theta}{2})$]
(S_{yy})	$\frac{K_I}{\sqrt{2\pi r}}\cos(\frac{\theta}{2})$ [1+$\sin(\frac{\theta}{2})sin(\frac{3\theta}{2})$]	$\frac{K_{II}}{\sqrt{2\pi r}}\sin(\frac{\theta}{2})$ $\cos(\frac{\theta}{2})cos(\frac{3\theta}{2})$
(τ_{xy})	$\frac{K_I}{\sqrt{2\pi r}}\cos(\frac{\theta}{2})$ $\sin(\frac{\theta}{2})cos(\frac{3\theta}{2})$	$\frac{K_{II}}{\sqrt{2\pi r}}\cos(\frac{\theta}{2})$ [1-$\sin(\frac{\theta}{2})sin(\frac{3\theta}{2})$]
(S_{zz})	v(S_{xx}+S_{yy})(Plane Strain)	v(S_{xx}+S_{yy}) (Plane Strain)
(S_{zz})	0 (Plane Stress)	0 (Plane Stress)
(τ_{xz})	0	0
(τ_{yz})	0	0

Within the scope of engineering implementations, usually a combination of these three modes are encountered which is denoted as mixed mode. In a mixed-mode problem, linear superposition principle is invoked and contribution of each loading mode is superposed in calculating the resultant stress tensor acting at the crack tip and it is expressed as

$$S_{ij}^{total} = S_{ij}^{I} + S_{ij}^{II} + S_{ij}^{III}. \tag{2.18}$$

The corresponding approach leads to a critical K value concept to describe the crack extension which is denoted as fracture toughness $K_{critical}$. Note that $K_{critical}$ values are determined from experiments under plane strain conditions. The underlying reasons will be detailed in the following sections.

2.5. Effect of Finite Size

At this stage, we should emphasize that the asymptotic analysis introduced so far governs on the crack tip region and it is derived based on an infinite domain assumption. However, it does not consider the free surface boundaries existing in finite size samples. This implies that the disturbance in the stress-strain-displacement fields must be accommodated by adjusting the independent K factors properly for these general configurations. Below, Figure 2.4 illustrates the effect of finite and infinite width on the crack tip stress distribution, which is represented by lines of force. In the Figure 2.4, the local stress state is directly related to the spacing between lines of force. It is salient that local stress near the crack tip is higher than far-field value. Also, due to the fact that a tensile stress cannot be transmitted through a crack, the lines of force are diverted around the crack. In Figure 2.4a, the line of force at a distance W from the crack centerline has force components in x and y directions. On the other hand, if the plate width is restricted to 2W as in Figure 2.4b, the traction along x direction is to be trivially zero at the free edge; this boundary condition causes the lines of force to be localized, which results in higher stress magnitude at the crack tip. As exemplified in Figure 2.4, the effect of finite size should be taken into account for accurate K factor calculations. Meanwhile, analytical approaches are successful in certain cases; in general, numerical methods need to be implemented to solve for stress, strain and displacement fields. We should note that the theory we revised so far considers no dissipative mechanisms such as plasticity or martensitic transformation. As the main focus of the present study is on SMA fracture response, in the following section plasticity effects on crack tip fields will be discussed briefly.

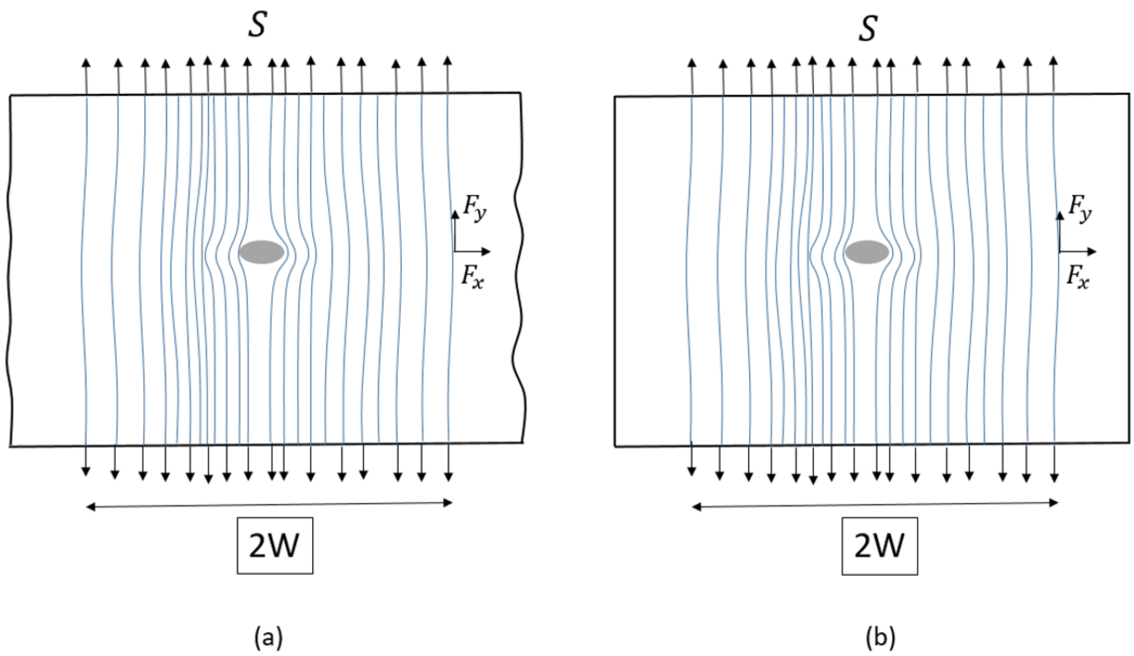

Figure 2.4. Stress concentration effects due to a through crack in finite and infinite width plates: (a) infinite plate and (b) finite plate

3. PLASTICITY EFFECTS IN FRACTURE MECHANICS

The asymptotic K field is disturbed by the presence of plastic deformation. Therefore, it is important to provide a background on the earlier studies in this section, as the effects of plasticity exhibit close resemblence to the martensitic transformation. Therefore, developing an understanding on crack tip plasticity effects stands out as an important step towards understanding the change of K with dissipative processes. Based on this perspective, we are going to list the prominent studies in the field below emphasizing the main contributions of them in the theory.

Table 3.1. Plasticity theories

Irwin Model	**Strip-Yield (Dugdale) Model**
$\mathrm{K}_{eff} = \frac{S\sqrt{\pi a}}{\sqrt{1-\frac{S^2}{2(S_{ys})^2}}}$	$\mathrm{K}_{eff} = S\sqrt{\pi a sec(\frac{\pi S}{2S_{ys}})}$
$\delta = \frac{4}{\pi}\frac{K_I^2}{S_{ys}E}$	$\delta = \frac{8S_{ys}a}{\pi E} In\sec(\frac{\pi S}{2S_{ys}})$
$\mathrm{r}_y = \frac{1}{2\pi}(\frac{K_I}{S_{ys}})^2$	$\rho = \frac{\pi}{8}(\frac{K_I}{S_{ys}})^2$
$\mathrm{r}_p = \frac{1}{\pi}(\frac{K_I}{S_{ys}})^2$	

In Table 3.1; K_{eff} defines effective stress intensity factor, δ defines crack tip opening displacement, r_y defines nominal crack tip, r_p and ρ defines plastic zone size within the scope of plasticity theories conducted by Irwin and Dugdale [26]. Following the establishment of K field approach, Cherapanov [29] and Rice [31] have proposed an integral line, called J integral, which stands out to be of constant value taken around a crack tip for elastic systems and is capable of characterizing the crack tip conditions by using elastic far field values. Below, the mathematical background for J Integral is briefly discussed as it is of significant use in characterizing crack tip fields within presence of plasticity effects.

3.1. J as a Path-Independent Line Integral

J integral is formulated using repeating indices summation convention

$$J = \int w dy - T_i \frac{\partial u_i}{\partial x} ds. \tag{3.1}$$

In this expression, w is strain energy volumetric density, T_i is traction vector components, u_i is displacement vector components where i is varying from 1 to 3 and ds is length increment along the contour as illustrated in Figure 3.1.

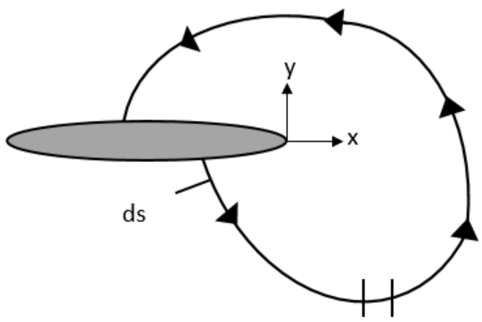

Figure 3.1. Arbitrary contour around the tip of a crack.

Among these terms, strain energy density, w, is expressed as

$$w = \int_0^{\epsilon} S_{ij} d\epsilon_{ij}, \tag{3.2}$$

where S_{ij} is the stress tensor and ϵ_{ij} is the strain tensor. Similarly, the traction vector components T_i are defined as

$$T_i = S_{ij} n_j, \tag{3.3}$$

where n_j is the i^{th} components of the unit vector normal to Γ.

As aforementioned, J integral is independent of the path of integration around the crack for linear elastic, isotropic, homogeneous systems. Furthermore, it can be shown that J integral and energy release rate, G, are equal to each other and expressed for Mode I explicitly as

$$J = \int wdy - T_i \frac{\partial u_i}{\partial x} ds = G = \frac{K_{\scriptscriptstyle 1}^2}{E}. \tag{3.4}$$

3.2. Evaluation of the J Integral as a Domain Integral

Precise quantification of the fracture metrics at the crack tip for materials undergoing dissipative deformation processes such as metal plasticity or martensitic transformation still stands out as a major challenge in fracture mechanics community. Among different techniques proposed, J integral is classified as a prominent figure with its broad capability in capturing the energy release rate with crack extension, especially for monotonic loading conditions in dissipative media under the conditions frequently named as J dominant zone. J dominant zone is located outside the process zone, where the HRR field accurately describes the deformation. On the other hand, adaptation of the line integral definition of J integral into finite element analysis framework is of limited success due to its high sensitivity with the interpolated field variables. Thus, domain integrals are incorporated to achieve accurate computation of energy release rate at the crack tip. Within this context, we will be focusing on the quasi-static (where the inertial effects are assumed to be equal to zero) problems with a general dissipative constitutive response encompassing both elastic and plastic as well as transformation induced deformation mechanisms. The generalized definition of J integral, stated in equation (3.5) requires that the contour $\mathit{\Gamma}_0$ surrounding the crack tip be vanishingly small in order to characterize the crack tip fracture mechanics metrics where T is the kinetic energy density and w is the stress work density. J Integral is expressed as

$$J = \lim_{\mathit{\Gamma}_0 \to 0} \int_{\mathit{\Gamma}_0} [(w^* + T)\delta_{1i} - S_{ij} \frac{\partial u_j}{\partial x_1}] n_i d\mathit{\Gamma}. \tag{3.5}$$

In the particular case of materials undergoing a reversible martensitic transformation, within the absence thermal and inertial effects (T=0) and unloading, total strain, ϵ_{ij}^{total}, can be assumed to be linearly decomposed as elastic, ϵ_{ij}^{e}, and transformation induced, ϵ_{ij}^{tr}, portions in equation (3.6).

$$\epsilon_{ij}^{total=}\epsilon_{ij}^{e}+\epsilon_{ij}^{tr}. \tag{3.6}$$

Thus, the stress work term can be formulated as

$$w^{*}=\int_{0}^{\epsilon}S_{ij}d\epsilon_{ij}^{total}. \tag{3.7}$$

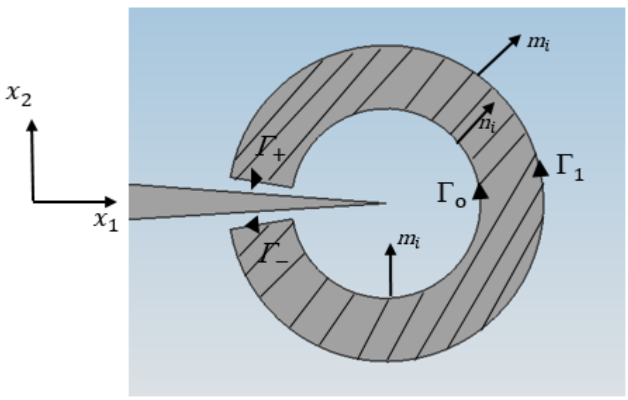

Figure 3.2. Inner ($\mathit{\Gamma}_o$) and outer ($\mathit{\Gamma}_1$) contours, which form a closed contour around the crack tip when connected by $\mathit{\Gamma}_+$ and $\mathit{\Gamma}_-$ on the crack surfaces.

The generalized formulation of J Integral is not appropriate for numerical fracture mechanics analyses as obtaining an accurate mechanical field poses a challenging task along with the presence of crack tip singularity. To overcome this problem, two closed contours, excluding but near the crack tip named as inner $\mathit{\Gamma}_0$ and outer $\mathit{\Gamma}_1$ contours, are traversed and connected by $\mathit{\Gamma}_+$ and $\mathit{\Gamma}_-$ as illustrated in Figure 3.2.

Noting that, outer Γ_1 contour is finite and Γ_0 is imposed to be vanishingly small, the J integral along the closed contour Γ^*, ($\Gamma^* = \Gamma_1 + \Gamma_+ + \Gamma_-$ - Γ_0), is stated as

$$J = \int_{\Gamma^*} [S_{ij}\frac{\partial u_j}{\partial x_1} - w\delta_{1i}]qm_i d\Gamma - \int_{\Gamma_+ + \Gamma_-} [S_{2j}\frac{\partial u_j}{\partial x_1}]qd\Gamma, \tag{3.8}$$

where m_i is the outward unit normal on Γ^*. Note that q=0 on Γ_1 and q=1 on Γ_0. Furthermore, m_i=-n_i on Γ_0. Additionally, m_1=0 and m_2=$\pm$1 on Γ_+ and Γ_-. When there are no tractions on crack faces, second integral vanishes in second equation. Invoking for the divergence theorem, leads to equation (3.9) as

$$J = \int_{A^*} \frac{\partial}{\partial x_i}([S_{ij}\frac{\partial u_j}{\partial x_1} - w\delta_{1i}]q)dA, \tag{3.9}$$

where A^* is the area enclosed by Γ^*. In the end, J integral is expressed as

$$J = \int_{A^*} [S_{ij}\frac{\partial u_j}{\partial x_1} - w\delta_{1i}]\frac{\partial q}{\partial x_i}dA + \int_{A^*} [\frac{\partial}{\partial x_i}(S_{ij}\frac{\partial u_j}{\partial x_1}) - \frac{\partial w}{\partial x_1}]qdA. \tag{3.10}$$

3.3. Crack Tip Triaxiality

So far, only a 2D specimen geometry is considered but no thickness effect is taken into account. Consider a cracked plate with thickness B subject to in-plane loading in Figure 3.3. Hence, the material at the crack tip tries to contract in the x and z directions because of the large stress normal to the crack plane. However, contraction is prevented by the surrounding material. This constraint results in a triaxial state of stress near the crack tip as a function of thickness (z coordinate) which is not considered in detail in the earlier discussion. The variation of S_{33} versus z is shown in Figure 3.4. At the interior plate, triaxial stress effect is high and the stress state essentially converges to plane strain state (i.e. S_{33} = v(S_{11}+S_{22})). In contrast, triaxial stress effect is suppressed at free surface and the stress state converges to pure plane stress state such that $S_{33} = 0$.

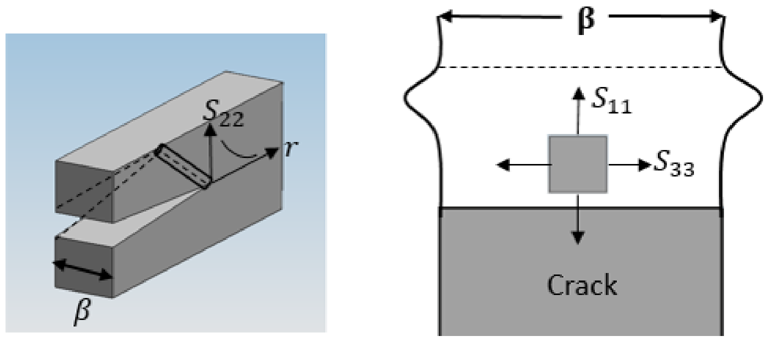

Figure 3.3. Three-dimensional deformation at the tip of a crack.

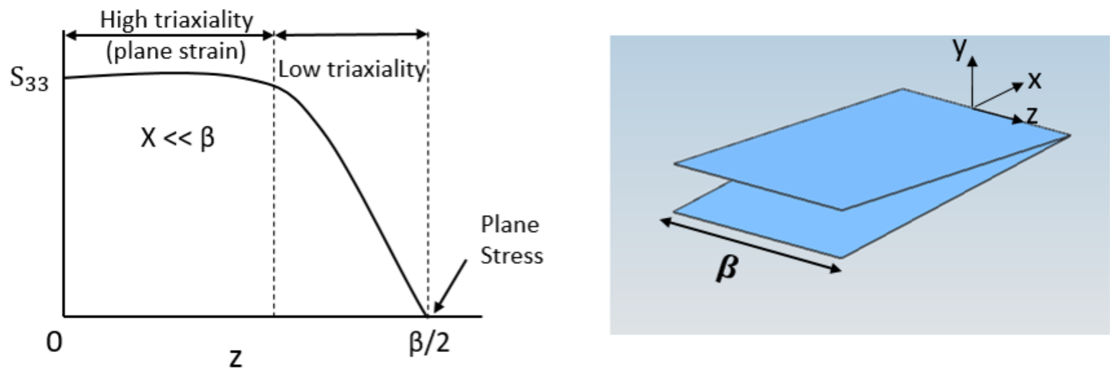

Figure 3.4. Schematic variation of transverse stress and strain through the thickness at a point near the crack tip.

3.4. Effect of Thickness on Apparent Fracture Toughness

As aforementioned, thickness dependence of fracture toughness levels are critical in material design. K_{crit} which is a measure of critical fracture toughness value associated with crack advancement, is a function of specimen thickness and reaches to a steady-state level which is named as plane strain fracture toughness $K_{\rm Ic}$.

In general, K_{1c} value is employed as the critical level based on the thickness dependence of K_{crit}. The decreasing trend in K_{crit} with thickness is attributed to triaxiality effect governing on crack tip response in ductile materials. To this end, the material is said to exhibit crack tunneling effect. The underlying mechanism can be detailed such that as a specimen is loaded monotonically, the mid-section of the crack front will advance first,and the free surfaces lead to 45^o angle to the applied load as seen in Figure 3.5. The resulting fracture model exhibits a flat region in the center and 45^o shear lips on the edges. Fractography of brittle materials do not exhibit any shear lips as plastic mechanisms are suppressed.

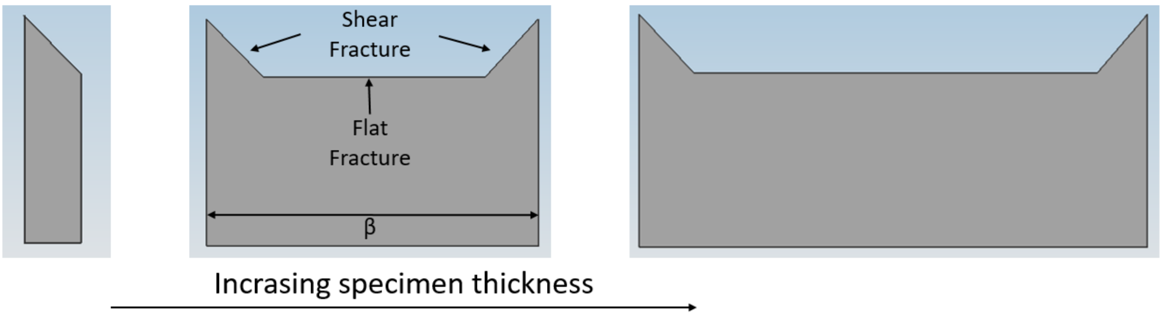

Figure 3.5. Effect of specimen thickness on fracture surface morphology for materials that exhibit ductile crack growth.

3.5. Plastic Zone Effect

There is no direct relationship between the plastic zone size and the plane strain conditions near the crack tip. According to 3D elastic-plastic finite element analysis for fracture toughness specimens, high degree of triaxiality persists near the crack tip even the entire specimen cross-section yields [28]. Since both plastic and elastic zones contribute to K level, the single parameter approaches based on small-scale yielding cannot be directly employed under fully plastic conditions. In order to overcome this difficulty, more elaborate criterion covering the plastic energy dissipation needs to be incorporated in calculations.

On physical grounds, J integral or crack tip opening displacement (CTOD) terms can be used as they are directly related with potential energy release rate. At low K values, the plastic zone shape exhibits dominantly plane strain character and at higher K values plastic zone converges to a plane-stress shape. It is known that plane strain conditions exist near the crack tip inside the interior plate. This corresponds to the fact that plastic zone shape exhibits plane strain character as plasticity effects dominate approximately half the plate thickness. This trend illustrates that high triaxiality zone at the crack tip can persist even in the presence of large-scale plasticity conditions. Based on this perspective, a single parameter approach either considering solely plane-strain or plane-stress is not sufficient to capture the crack tip fracture response in presence of large-scale plasticity. As SMA systems tend to exhibit large transformation strain levels around the crack tip zone, a similar behavior for SMAs are expected as observed in ductile materials. This introduces a necessity for a two parameters analysis.

In Figure 3.6, the general crack tip field is characterized based on the dominance of yielding conditions such as large strain region enclosed by J dominated zone which in turn surrounded by K dominant field. Among these, the region where stress varies with $1 / \sqrt{r}$ singularity is called K-dominated region. Linear elastic fracture mechanics techniques prevail in this outermost domain. Closer to the crack tip, J dominated region occurs inside a plastic region which on theoretical grounds, can be approximated by a strain-hardening plastic model enabling explicit calculation of the critical J value, J_c associated with crack advancement.

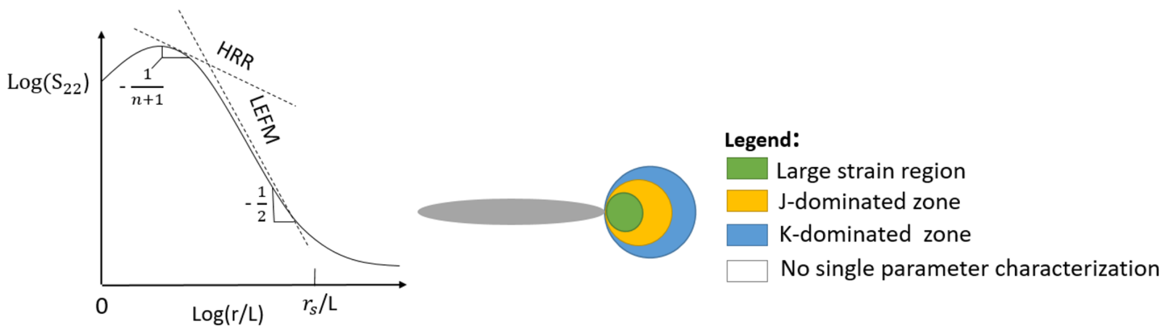

Figure 3.6. Effect of plasticity on the crack tip stress fields: (a) small-scale yielding.

Closer to crack tip, a large strain zone of fully plastic forms. In this zone, the presence of large-scale yielding exceeds the capabilities of single parameter fracture mechanics and necessitates additional parameters. In this case, use of T stress or Q term is suggested in the earlier literature [33]. In the next section, these approaches will be introduced briefly.

3.5.1. T-Stress

Meanwhile, the asymptotic $r^{-0.5}$ term in in crack tip stress field is governed by K term, as detailed by the work of Williams [28], the following term of 0^o captures the S_{11} term and this term is expressed as

$$S_{11} = \frac{K_I}{\sqrt{2\pi r}} f_{11}(\theta) + T. \tag{3.11}$$

Considering the plane-strain conditions governing at the interior of the cracked samples of finite thickness, T stress term has a direct contribution on S_{33} field. This contribution in T stress magnitude promotes strong triaxiality effects at the crack tip. Therefore, T stress term can be employed to consider triaxiality governing at the crack tip accurately. The promotion of T stress, increases crack-tip triaxiality. At this stage, it should be emphasized, T stress term exhibit strong dependence on geometry similar to K term.

3.5.2. J-Q Theory

The second approach in developing two-parameter fracture mechanics involves J-Q theory. J-Q theory is valid for nonlinear material response embracing crack tip plasticity. In this theory, Q parameter is added as a hydrostatic stress field shift in front of crack tip. It is very similar to T stress which considers r^0 term but the significant point is that Q parameter dominates only in front of crack tip while T stress prevails over a larger domain and stress field is expressed as

$$S_{ij} \approx S_{ij(T=0)} + QS_0\delta_{ij} \mid \theta \mid \leq \frac{\pi}{2}. \tag{3.12}$$

In this equation, Q term is defined as

$$Q = \frac{S_{22} - (S_{22})_{T=0}}{S_0} \tag{3.13}$$

at $(r,\theta) = (r^*, 0)$. The radial coordinate r^* satisfies

$$r^* = \frac{2J}{S_0}. \tag{3.14}$$

3.6. Fracture Mechanics of SMAs

With the emerging need for functional materials in industrial, military and transportation applications, the fracture behavior of SMAs has been a popular research area [2-4], [15]. The crack tip stress components, S_{ij}, based on linear elastic fracture mechanics (LEFM) theory for mode I loadings can be expressed in terms of the cylindrical coordinates as following equation, (3.15),

$$S_{ij}(r,\theta) = \frac{K_I}{\sqrt{2\pi r}} f_{ij}(\theta). \tag{3.15}$$

In this perspective, K_I is explicitly denoted as K_I^{∞} standing out as remote stress intensity factor based on LEFM [43]. This is important in a sense that the crack tip martensitic transformation is likely to introduce toughening effect that reduces the actual tip stress intensity factor compared to remote stress intensity factor. Figure 3.7 shows that stress induced martensite (SIM), occurring near crack tip of NiTi alloys, results in a rather complicated stress distribution with a constant stress regime stemming from the transformation plateau. Three different regions are observed near the crack tip. The first region is austenitic or untransformed region for $r > r_A$, (S_e<S^{tr}). The second region is transformation zone for $r_M < r < r_A$, (S_e≈S^{tr}). The third region is martensitic or fully transformed region for $r < r_M$, (S_e>S^{tr}).

In these regions, S_e is defined as an equivalent stress based on the transformation criterion employed with r_A and r_M representing the boundaries of fully martensitic and fully austenitic regions connected with a partially transformed domain. Within this scope, principal stress components in the austenitic region for θ=0 under plane stress condition denoted by S_{Ai}(r) is formulated [42].
S_{A1}(r) is expressed as

$$S_{A1}(r) = \frac{K_{Ie}}{\sqrt{2\pi r}}. \tag{3.16}$$

S_{A2}(r) is stated as

$$S_{A2}(r) = \frac{K_{Ie}}{\sqrt{2\pi r}}. \tag{3.17}$$

S_{A3}(r) is identified as

$$S_{A3}(r) = 0, \tag{3.18}$$

where K_{Ie} is defined as Mode I effective stress intensity factor defined based on an artificial effective crack length a_e that is expressed as a function of transformation stress and transformation zones. Based on this approach, the principal stress components in the martensitic region for θ=0, denoted by S_{Mi}(r) is formulated.
S_{M1}(r) is expressed as

$$S_{M1}(r) = \frac{1}{2(1-v) + (\alpha^{-1} - 1)}[2(1-v)\frac{K_{Ie}}{\sqrt{2\pi r}} + (\alpha^{-1} - 1)S^{tr} - \epsilon_L E_A]. \tag{3.19}$$

S_{M2}(r) is defined as

$$S_{M2}(r) = \frac{1}{2(1-v) + (\alpha^{-1} - 1)}[2(1-v)\frac{K_{Ie}}{\sqrt{2\pi r}} + (\alpha^{-1})S^{tr} - \epsilon_L E_A]. \tag{3.20}$$

S_{M3}(r) is evaluated as

$$S_{M3}(r) = 0. \tag{3.21}$$

In these equations, α is expressed as

$$\alpha = \frac{E_M}{E_A}. \tag{3.22}$$

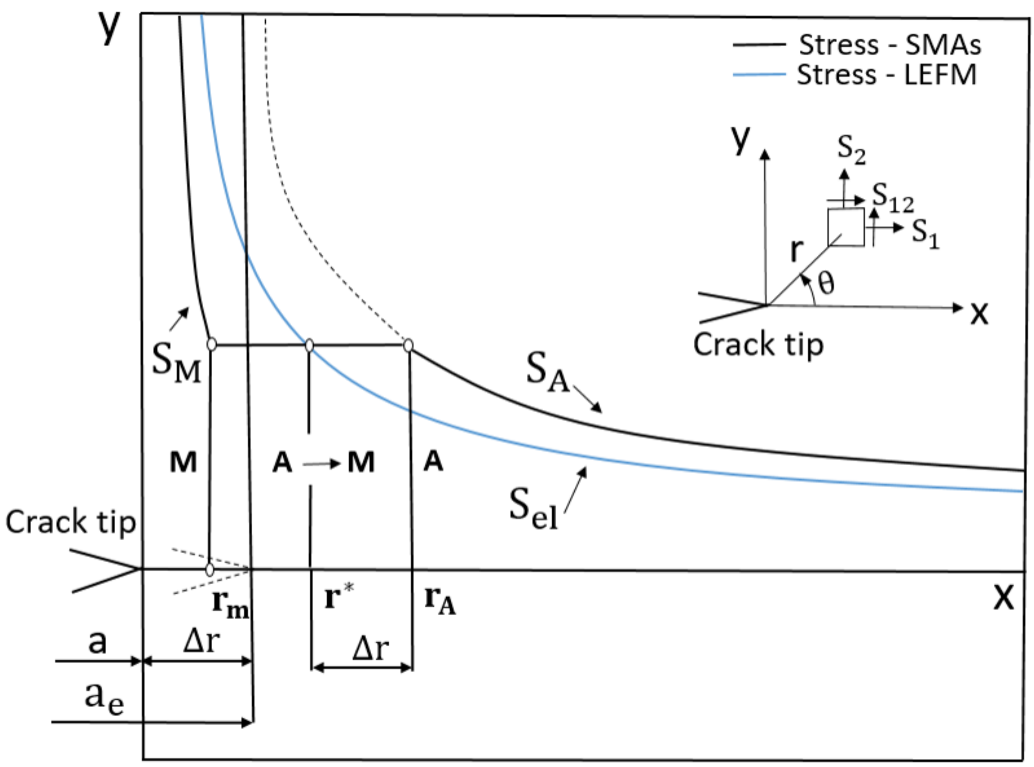

Figure 3.7. Schematic depiction of the stress distribution and phase transformation in the crack tip region of NiTi alloys

Within the scope of this analytical approach, the martensitic transformation results in a lower effective stress intensity factor resulting from the energy dissipation during transformation at the crack tip.

Therefore, the martensitic transformation contribution on the crack tip fields is substantial and needs to be considered in any rigorous design effort. Moreover, the results in the literature have mainly focused on Mode I configuration. On the other hand, mixed mode problems are also frequently encountered in real-life engineering applications. Based on this motivation, within the scope of the present study, pure Mode I and mixed mode (Mode I+ Mode II) stress fields for NiTi SMA will be elaborated employing finite element analysis in the following section.

4. METHODOLOGY AND RESULTS

4.1. Problem Geometry

As an initial step towards characterizing the stress fields evolved around the crack tip in an SMA material of NiTi, using finite element modelling environment of ABAQUS software, a single edge cracked specimen under plane strain conditions of height h = 100 mm and the width W = 100 mm is introduced. A straight edge crack of size a = 25 mm is included in the model. The plate is made of an isotropic linear elastic material with a Young's modulus of E = 70 GPa and Poisson's ratio $v = 0.35$. A symmetric, uniform far-field tensile stress field of $S^{\infty} = 40$ MPa is applied. Additional displacement boundary conditions are imposed such that no in-plane displacement or rotation about the out-of plane axis is allowed at the far-field edge point lying at the intersection of the crack plane extension and specimen surface as illustrated in Figure 4.1.(a).

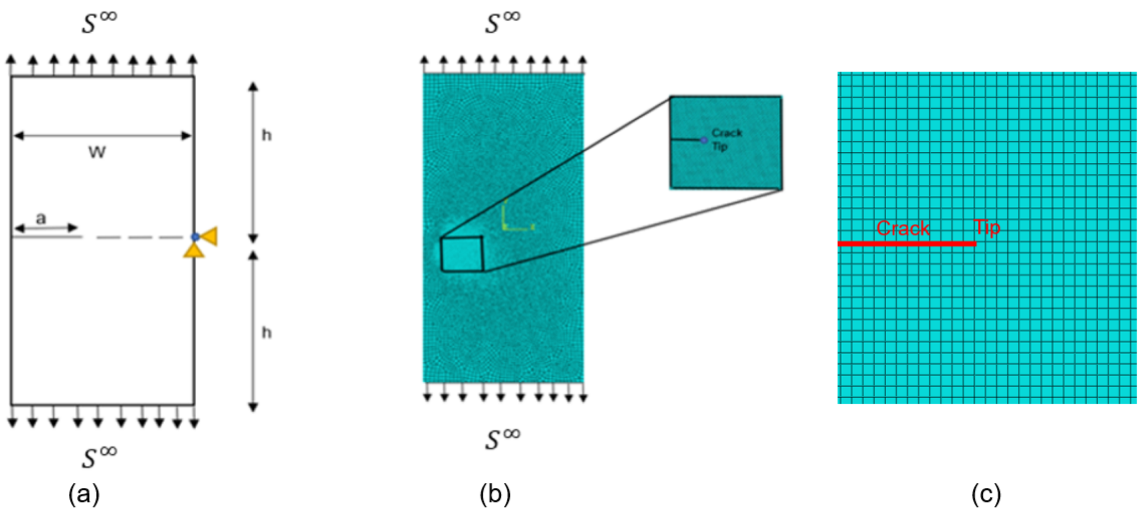

Figure 4.1. (a) Single edge notch specimen geometry and dimensions are illustrated. (b) Meshed configuration of the specimen. (c) Square meshes around the crack tip zone.

ABAQUS calculations provided the displacement and stress fields as well as the J contour integral values. As demonstrated in the earlier sections, the contour integral values can be expressed in terms of elastic constants and stress intensity factor values for linear elastic materials. In order to calibrate the model parameters in ABAQUS, the analytical geometric factor, F, formulation proposed by Gross (1964) and Brown (1966) based on the least square fitting given as [45]

$$F = 0.265(1-\frac{a}{W})^4 + (0.857 + 0.265\frac{a}{W})/(1-\frac{a}{W})^{3/2}. \tag{4.1}$$

Noting that (a/W) ratio is equal to 0.25 for the configuration focused, the corresponding geometric factor is calculated as F=1.505. Similarly, the resulting theoretical stress intensity factor,K_I^{theo}, is evaluated as 533.609 MPa$\sqrt{m}$. On the other hand, noting that J contour integral values are path independent in the present configuration, the resulting J value from ABAQUS modelling is calculated as 3.530 J/mm^2. This value corresponds to a stress intensity factor of K_I= 530.663 MPa$\sqrt{m}$. As can be seen, the analytical and the numerical ABAQUS solutions for Mode I stress intensity factor differs only by 0.552 %. This result exhibits the accuracy level of the modelling parameters embodied in ABAQUS environment. Based on this high level of agreement between theoretical prediction and finite element calculations, the present meshing scheme is adopted also for the following analyses.

4.2. Inclined Crack Configuration

As a second step in modelling efforts of the linear elastic (identical properties as with the straight cracked geometry) sample (similarly exhibiting austenite NiTi elastic response) using ABAQUS, an inclined edge crack in a rectangular plate under plane strain conditions of height h = 100 mm and width W = 100 mm is subjected to the same far-field stress field and displacement boundary conditions as in the straight crack which is illustrated in Figure 4.2 (a). As in the previous case, the crack size a is set to be equal to 25 mm making an angle of $\alpha = \{10^o, 20^o, 30^o\}$ in clockwise sense.

For non-zero α values, the elastic conditions at the crack tip exhibit both Mode I and Mode II, i.e. mixed mode, characteristics. Thus, neither K_I nor K_{II} terms vanish in the asymptotic expansion formulation discussed above.

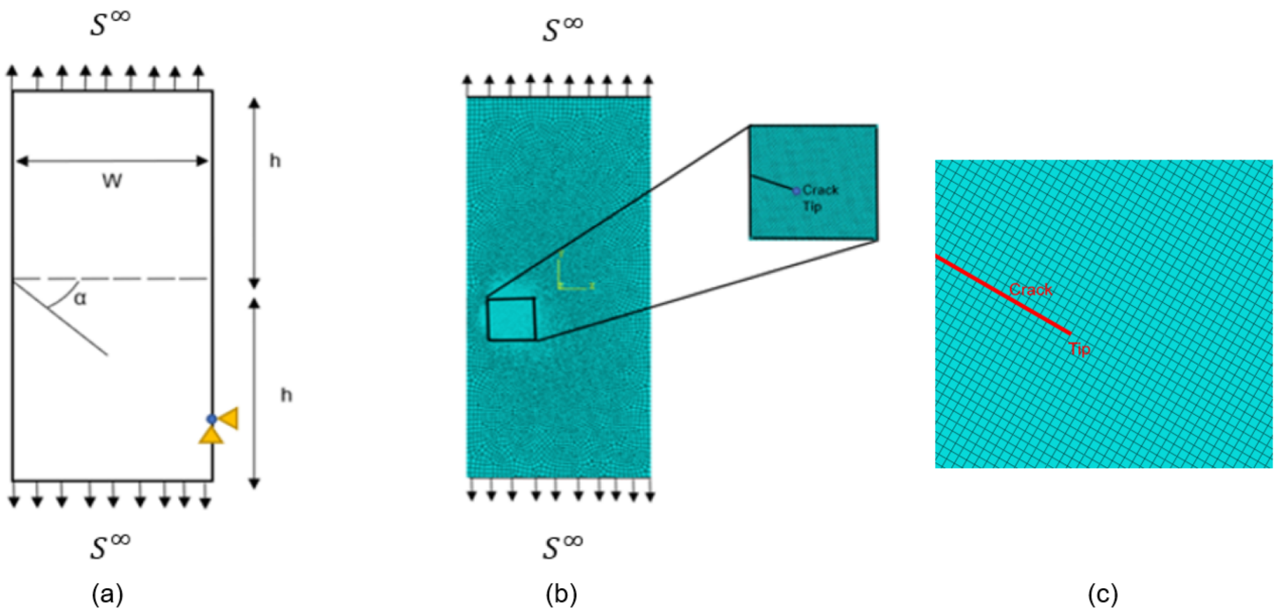

Figure 4.2. (a) Single edge specimen geometry of an inclined edge crack. (b) Meshed configuration for the specimen with an inclined crack. (c) Square meshes around the crack tip zone.

On the other hand, the contour independent J Integral stands out as an instrumental tool in describing the potential energy release rate for both straight and inclined crack configurations in linear elastic, homogeneous materials. Based on this motivation, the J contour integral values are evaluated for the set of α angles of $\{10^o, 20^o, 30^o\}$ and tabulated in Table 4.1. For comparison reasons, $\alpha = 0$ case is also invoked. The results indicate that the J contour integral values, being equal to the potential energy release rates also for this material, exhibit a decreasing trend up on increasing the crack inclination angle α.

Table 4.1. The variation of J contour integral with the crack inclination angle α for various transformation strain levels. The J integral units are in J/mm^2.

Crack Angle α	0^o	10^o	20^o	30^o
J for ϵ^L = %4	3.592	3.431	2.990	2.373
J for ϵ^L = %6	3.595	3.430	2.990	2.375
J for ϵ^L = %8	3.597	3.436	2.993	2.375

4.3. Modelling Single Edge Crack Behavior for NiTi Shape Memory Alloy

In adaptation of superelastic response in ABAQUS platform, the built-in superelastic NiTi SMA constitutive material model, based on Auricchio's model, is employed. The austenite phase behaves as an isotropic, linear elastic material with a Young's modulus of $E_A = 70$ GPa and Poisson's ratio $v = 0.35$. The martensitic phase starts to form at S_{MS} and arrives at a completion by the stress level of S_{MF}. The Young's modulus of martensite phase, E_M, is set equal to 35 GPa meanwhile the Poisson ratio is taken as same as austenite.

From a mechanical point of view, the elastic predictor-plastic corrector algorithm is employed to solve for the multiaxial stress tensor, $\boldsymbol{S}$, the total strain tensor $\boldsymbol{\epsilon}$ and the martensite phase volume fraction ξ. In the material model utilized (based on small strain approach), in 3D the total strain increment tensor, $\boldsymbol{\Delta\epsilon}$, is composed of the elastic strain increment, $\boldsymbol{\Delta\epsilon^{el}}$, and the transformation strain increment $\boldsymbol{\Delta\epsilon^{L}}$ such that (using repeating index summation convention with i, j = 1 to 3)

$$\Delta\epsilon_{ij} = \Delta\epsilon_{ij}^{el} + \Delta\epsilon_{ij}^{L}. \tag{4.2}$$

The transformation strain increment tensor $\boldsymbol{\Delta\epsilon^{L}}$ is evaluated based on the gradient of the transformation flow potential G^{tr} which is defined as

$$G^{tr} = S^{eq} - C_{tr}T. \tag{4.3}$$

In this expression, S^{eq} is von-Mises equivalent stress, C_{tr} is a material parameter dependent on the hardening modulus H, martensite start stress S_{MS} as well as transformation strain ϵ_L. Based on the normality condition, $\Delta\epsilon_{ij}^L$ components are determined as

$$\Delta\epsilon_{ij}^L = \Delta\xi \frac{\partial G^{tr}}{\partial S_{ij}} \tag{4.4}$$

with an increment of martensite volume fraction $\Delta\xi$. The model follows generalized plasticity framework and the corresponding austenite-martensite transformation surface, F^{tr}, is adapted as

$$F^{tr} = \sigma^{eq} - C_M T = 0. \tag{4.5}$$

In this expression, C_M is a material parameter dependent on temperature sensitivity of S_{MS} and T is the ambient temperature chosen as 40^{o}C in the present work. The identical geometry introduced earlier for the single edge cracked plate under plane strain conditions of the height h = 100 mm and the width W = 100 mm height is used. A straight edge crack of size a = 25 mm is included in the model. A symmetric, uniform far-field tensile stress field of S^∞ = 40 MPa is applied. The same displacement boundary conditions as in the linear elastic case is adapted in order to restrict rigid body rotation. It is to be noted that no unloading is considered throughout the present work. Thus, martensite to austenite transformation does not come in to play.

As conventional linear elastic fracture mechanics do not provide a direct methodology for the stress intensity factor and the other higher order stress field terms around a crack tip in an SMA undergoing martensitic transformation, the stress data evaluated by finite element analysis are employed generate a closed-form approximation. For this purpose, a 10 x 10 square element cluster surrounding crack tip is generated forming eleven node paths as shown in Figure 4.3. Stress components in the default ABAQUS coordinate frame (S_{11}, S_{12}, S_{21}, S_{22}, S_{33}), varying with the corresponding radial distance, r, and azimuthal angle, θ, are obtained in finite element model for each node.

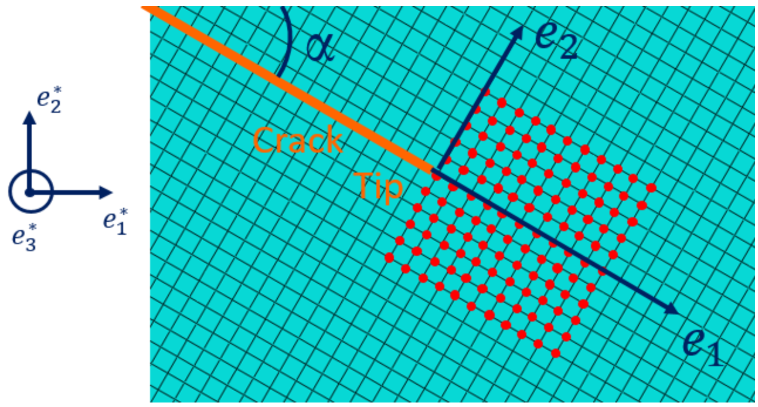

Figure 4.3. 10 x 10 square element cluster contains eleven node path shown with red marks.

The non-zero stress tensor components of S_{11}, S_{12} $(= S_{21})$, S_{22} and S_{33} in default ABAQUS Cartesian coordinate frame defined with the base vectors $e_1^* - e_2^* - e_3^*$ are transformed into a locally defined Cartesian coordinate frame having base vectors of $e_1 - e_2 - e_3$ by rotating a clockwise angle of α equal to $0^o, 10^o, 20^o, 30^o$ as the illustrated in Figure 4.3 and Figure 4.4 for the particular case of 20^o.

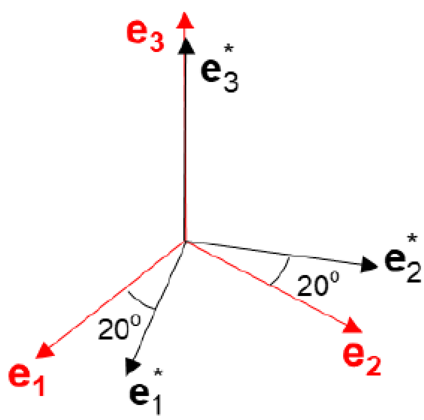

Figure 4.4. Example of transformed coordinate system for 20^o case.

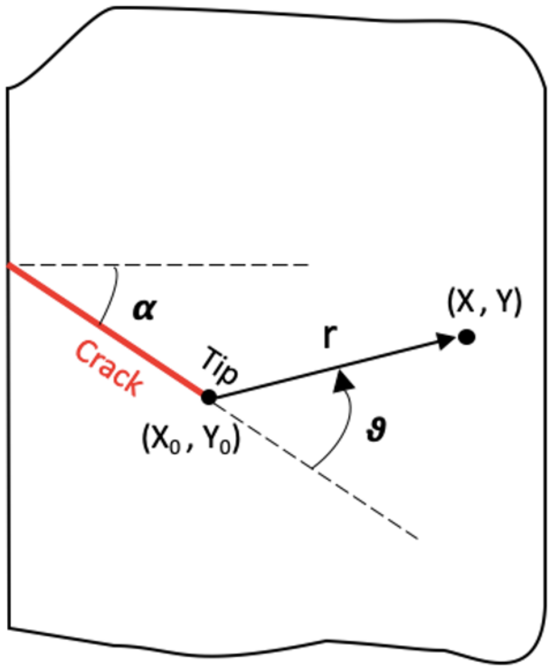

Figure 4.5. Inclined crack configuration of NiTi

Following the transformation operation, the collected discrete stress component data are cast into a continous form using the asymptotic function set. In the computational scheme employed, stress transformation operations are conducted by firstly by expressing the crack tip coordinates of (X_0, Y_0) as illustrated in Figure 4.5. Afterwards node coordinate positions, except crack tip, are denoted as (X, Y). Radial distance, r values of each node inside path are calculated as

$$r = \sqrt{(X - X_0)^2 + (Y - Y_0)^2}. \tag{4.6}$$

Similarly the azimuthal angle, θ, is defined as below

$$\theta = \arctan(\frac{Y - Y_0}{X - X_0}) + \frac{2\pi\alpha}{360}, \tag{4.7}$$

where α is crack inclination angle.

In order to accomodate for the angular variation of stress fields around the crack tip, the set of trigonometric parameters $\{m_{ij}, n_{ij}, v_{ij}, w_{ij}\}$ are introduced where the subscripts i,j = 1,2. As a further step to embrace the radial term effect other than asymptotic term, r^o terms denoted as A_{ij}, with i,j = 1,2, are introduced in the fit functions. The fit functions of stress components are listed in equations (4.8), (4.9), (4.10), respectively.

S_{11}^{fit} is expressed as

$$S_{11}^{fit} = \frac{K^{eq}}{\sqrt{(2\pi r)}}[sin(m_{11}\theta)cos(n_{11}\theta) + sin(v_{11}\theta) + cos(w_{11}\theta)] + A_{11}. \tag{4.8}$$

S_{12}^{fit} is expressed as

$$S_{12}^{fit} = \frac{K^{eq}}{\sqrt{(2\pi r)}}[sin(m_{12}\theta)cos(n_{12}\theta) + sin(v_{12}\theta) + cos(w_{12}\theta)] + A_{12}. \tag{4.9}$$

S_{22}^{fit} is expressed as

$$S_{22}^{fit} = \frac{K^{eq}}{\sqrt{(2\pi r)}}[sin(m_{22}\theta)cos(n_{22}\theta) + sin(v_{22}\theta) + cos(w_{22}\theta)] + A_{22}, \tag{4.10}$$

where S_{12}^{fit} component is equal to S_{21}^{fit} due to symmetry of the stress tensor. The corresponding error functions for each stress component are introduced as the difference between the transformed stress component and the fit function value as expressed in equation (4.11), (4.12), (4.13) and (4.14).

f_{error}^{11} is expressed as

$$f_{error}^{11} = S_{11} - S_{11}^{fit}. \tag{4.11}$$

f_{error}^{12} is expressed as

$$f_{error}^{12} = S_{12} - S_{12}^{fit}. \tag{4.12}$$

f^{21}_{error} is expressed as

$$f^{21}_{error} = S_{21} - S^{fit}_{21}. \tag{4.13}$$

f^{22}_{error} is expressed as

$$f^{22}_{error} = S_{22} - S^{fit}_{22}. \tag{4.14}$$

The individual fitting operations are employed in order to extract the equivalent stress intensity factor levels, K^{eq} , evaluate the stress triaxiality, Q. These parameters are dependent on the extent of hardening during transformation, the effects of transformation start and end stresses and transformation strains.

5. STRAIN HARDENING EFFECT

5.1. Role of Strain Hardening Modulus

In this chapter, strain hardening effect is elaborated to build an understanding on the response in crack tip fields to the hardening level changes during transformation. For this purpose, both the collected stress component data from ABAQUS S_{11}, S_{12} and S_{22} and fit stress components S_{11}^{fit}, S_{12}^{fit} and S_{22}^{fit} are visualized under different hardening modulus conditions. Hardening modulus, H, is formulated as

$$H = \frac{S_{MF} - S_{MS}}{\epsilon^L}, \tag{5.1}$$

where S_{MS} and S_{MF} are martensite start and finish stresses along with the transformation strain ϵ^L of NiTi as illustrated in Figure 5.1 .

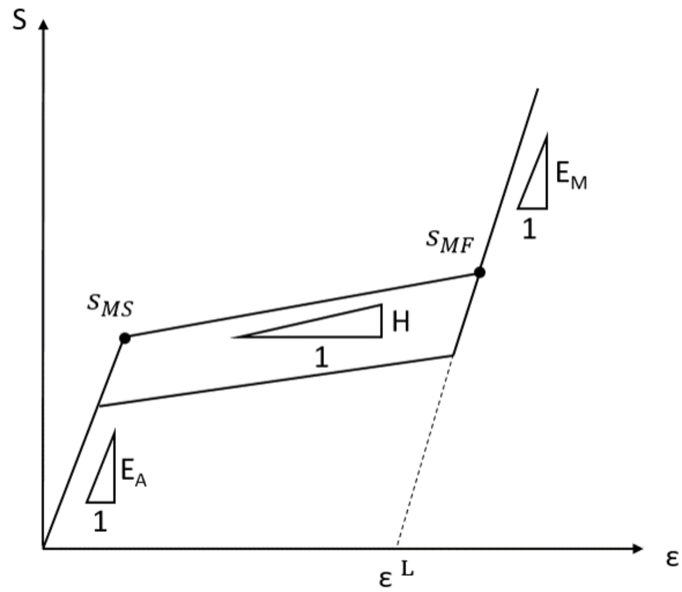

Figure 5.1. Uniaxial response of a superelastic material

5.2. 625 MPa Hardening Modulus Case

To generate a hardening modulus, H, equal to 625 MPa, the start and end stress levels of forward transformation are chosen as 200 MPa and 250 MPa for a given ϵ^L magnitude of 0.08, summarized in Table 5.1. The hardening modulus is explicitly calculated as

$$\mathrm{H} = \frac{250 - 200}{0.08}\mathrm{MPa} = 625\ \mathrm{MPa}. \tag{5.2}$$

Table 5.1. Superelastic material properties of H=625 MPa NiTi

Transformation Strain	0.08
Forward Transformation Start Stress	200 MPa
Forward Transformation End Stress	250 MPa

In order to extract K^{eq} level as a function of varying levels and crack angle α, a nonlinear fitting scheme is introduced in the previous section. For the fitting variables $\{K^{eq}, m_{ij}, n_{ij}, v_{ij}, w_{ij}\}$ based on the algorithm followed, initial values are to be assigned. In this case the set of initial values are chosen as $\{0.1\mathrm{MPa\ m}^{-1/2}, 1.1, 1.2, 1.5, 1\}$, respectively. Stress intensity factor values for 625 MPa hardening modulus is tabulated in Table 5.2 along with the tabulated fitting parameters as a function crack angle α in Tables 5.3 to 5.6.

Table 5.2. K^{eq}, A_{11}, A_{12}, A_{22} values with respect to crack angle α given H=625 MPa

α	0^o	10^o	20^o	30^o
K^{eq} [MPa$\sqrt{m}$]	170	150	140	130
A_{11} [MPa]	1.9	3.4	3.9	2.7
A_{12} [MPa]	-181.95	-151.55	-173	-161.62
A_{22} [MPa]	46.1	20.1	54.8	20.5

Table 5.3. Fit parameter values for straight crack angle of H=625 MPa

m_{11}	n_{11}	v_{11}	w_{11}
0.0006	1.769	0.0004	-0.8182
m_{12}	n_{12}	v_{12}	w_{12}
2.9500	6.1000	9.0500	1.3400
m_{22}	n_{22}	v_{22}	w_{22}
-0.0006	2.653	-0.00047	0.000064

Table 5.4. Fit parameter values for 10^o degrees crack angle of H=625 MPa

m_{11}	n_{11}	v_{11}	w_{11}
0.2800	1.3900	0.3500	-0.6100
m_{12}	n_{12}	v_{12}	w_{12}
2.6000	-1.4600	9.4000	1.0600
m_{22}	n_{22}	v_{22}	w_{22}
1.0800	1.0200	0.0600	-0.0003

Table 5.5. Fit parameter values for 20^o degrees crack angle of H=625 MPa

m_{11}	n_{11}	v_{11}	w_{11}
0.0880	1.7300	0.1900	-0.8400
m_{12}	n_{12}	v_{12}	w_{12}
0.3500	0.0000	0.3500	1.1800
m_{22}	n_{22}	v_{22}	w_{22}
0.3800	-0.6700	-0.2800	0.2300

Table 5.6. Fit parameter values for 30^o degrees crack angle of H=625 MPa

m_{11}	n_{11}	v_{11}	w_{11}
0.1300	0.8700	0.1500	-0.8500
m_{12}	n_{12}	v_{12}	w_{12}
1.2800	0.0000	-2.2500	1.0700
m_{22}	n_{22}	v_{22}	w_{22}
1.7600	4.1900	2.4300	0.0000

Both the raw and fit data for stress components, S_{ij} and S_{ij}^{fit} with i,j = 1,2 , for H=625 MPa level are plotted as function of radial coordinate, r and θ for each set of crack inclination angle set of $\{0^o, 10^o, 20^o, 30^o\}$. In Figure 5.2 to 5.4, the raw and fit stress components are plotted for a straight crack configuration, $\alpha = 0^o$. In the following plots, the blue circles represents fit stress component values meanwhile red points represent the raw stress component values collected from ABAQUS.

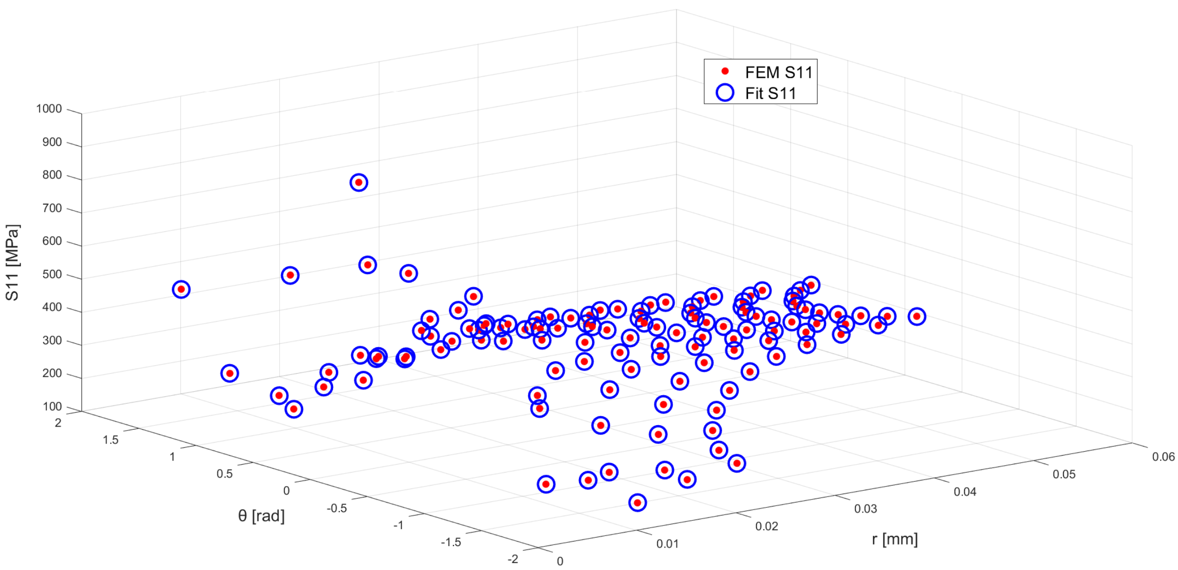

Figure 5.2. S_{11} in H=625 MPa case for straight crack.

For Figure 5.2, the maximum difference between S_{11} and S_{11}^{fit} is less than 1 MPa and this corresponds to only 0.1 % relative difference with respect to maximum of S_{11} data. Similarly, for Figure 5.3, the maximum gap between S_{12} and S_{12}^{fit} amounts less than 1 MPa for which the relative error ratio is 0.3 % with respect to the maximum S_{12}. The error margins are also very similar between S_{22} and S_{22}^{fit} data set as illustrated in Figure 5.4.

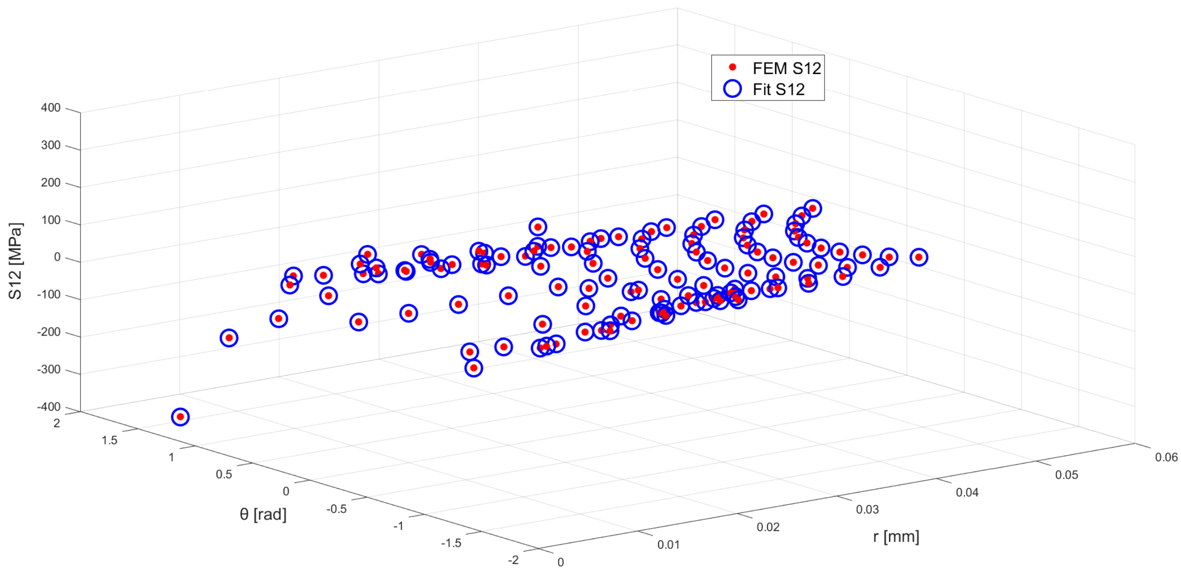

Figure 5.3. S_{12} in H=625 MPa case for straight crack.

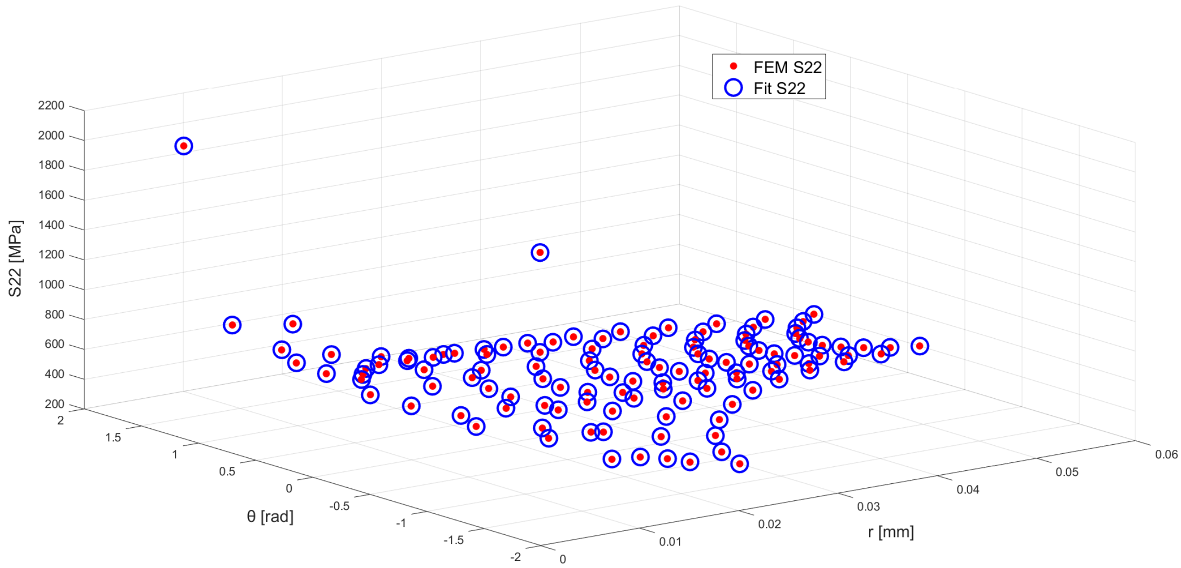

Figure 5.4. S_{22} in H=625 MPa case for straight crack.

In Figure 5.5 to 5.7, the raw and fit stress components are plotted for a straight crack configuration, $\alpha = 10^o$. In the following plots, the blue circles represents fit stress component values meanwhile red points represent the raw stress component values collected from ABAQUS. Meanwhile, for Figure 5.5, the maximum error between S_{11} and S_{11}^{fit} is only 2 MPa; it is only 1.5 MPa in the case of S_{12} and S_{12}^{fit} data sets. Furthermore, the error does not exceed 1.4 MPa between S_{22} and S_{22}^{fit}. To this end, the fitting functions for stress components are regarded as sufficiently accurate around the crack tip.

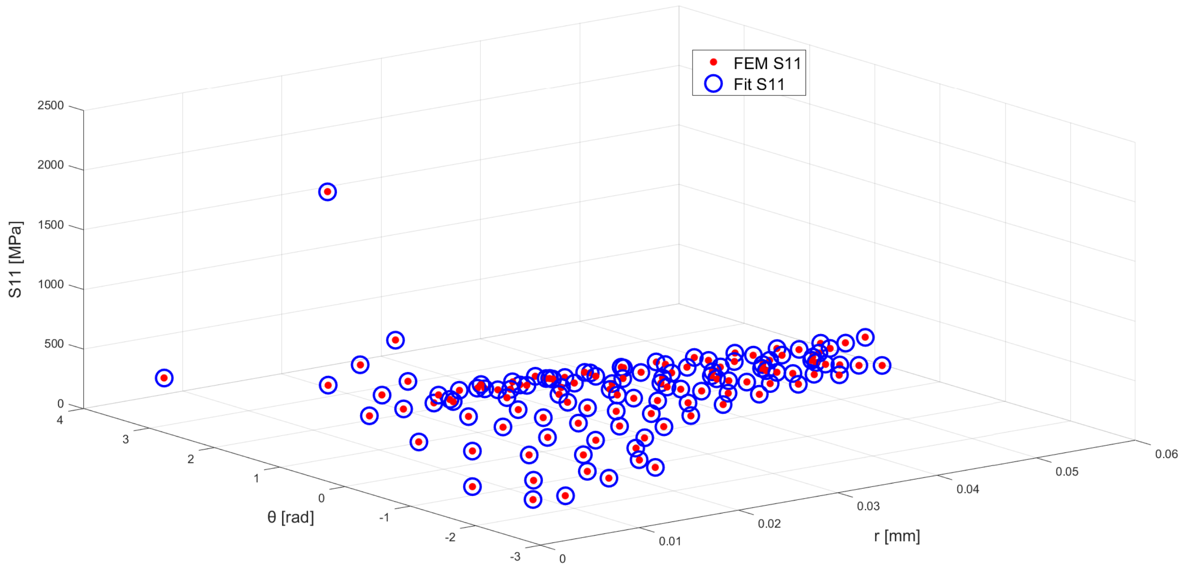

Figure 5.5. S_{11} in H=625 MPa case for 10^o degrees inclined crack.

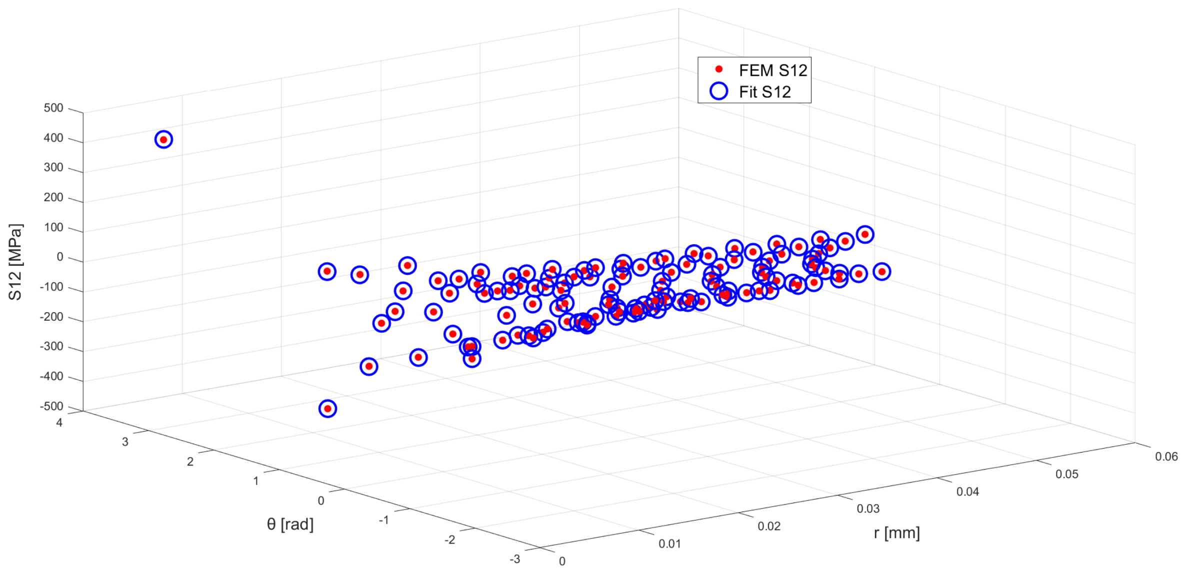

Figure 5.6. S_{12} in H=625 MPa case for 10^o degrees inclined crack.

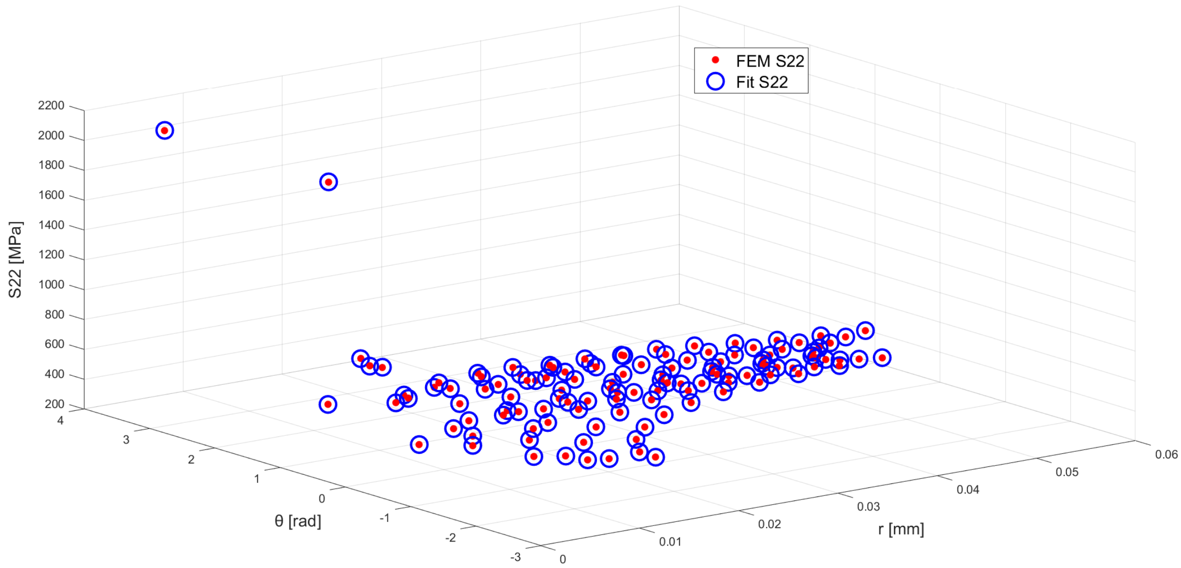

Figure 5.7. S_{22} in H=625 MPa case for 10^o degrees inclined crack.

In Figure 5.8 to 5.10, the raw and fit stress components are plotted for a straight crack configuration, $\alpha = 20^o$. In the following plots, the blue circles represents fit stress component values meanwhile red points represent the raw stress component values collected from ABAQUS. For these three stress components, S_{11}, S_{12} and S_{22}, the maximum differences between the fit values do not exceed 1 MPa.

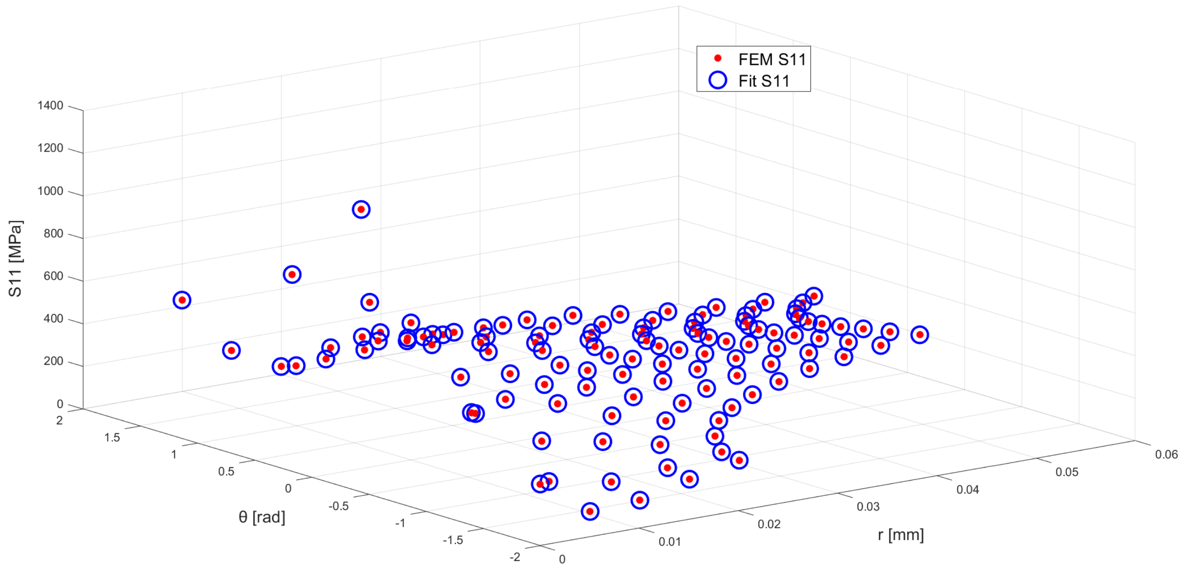

Figure 5.8. S_{11} in H=625 MPa case for 20 degrees inclined crack.

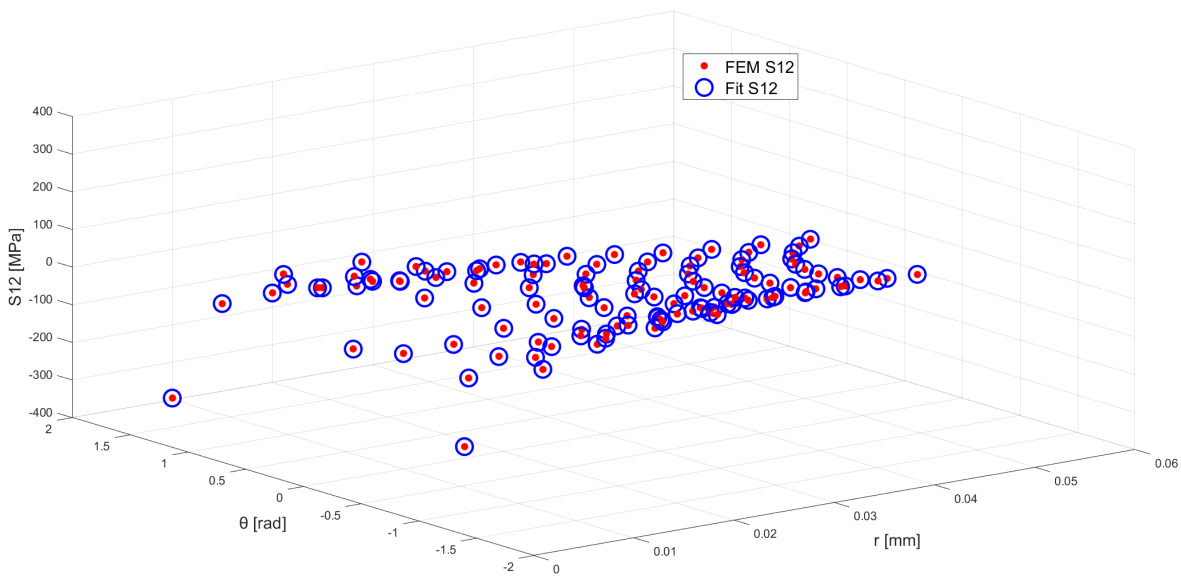

Figure 5.9. S_{12} in H=625 MPa case for 20^o degrees inclined crack.

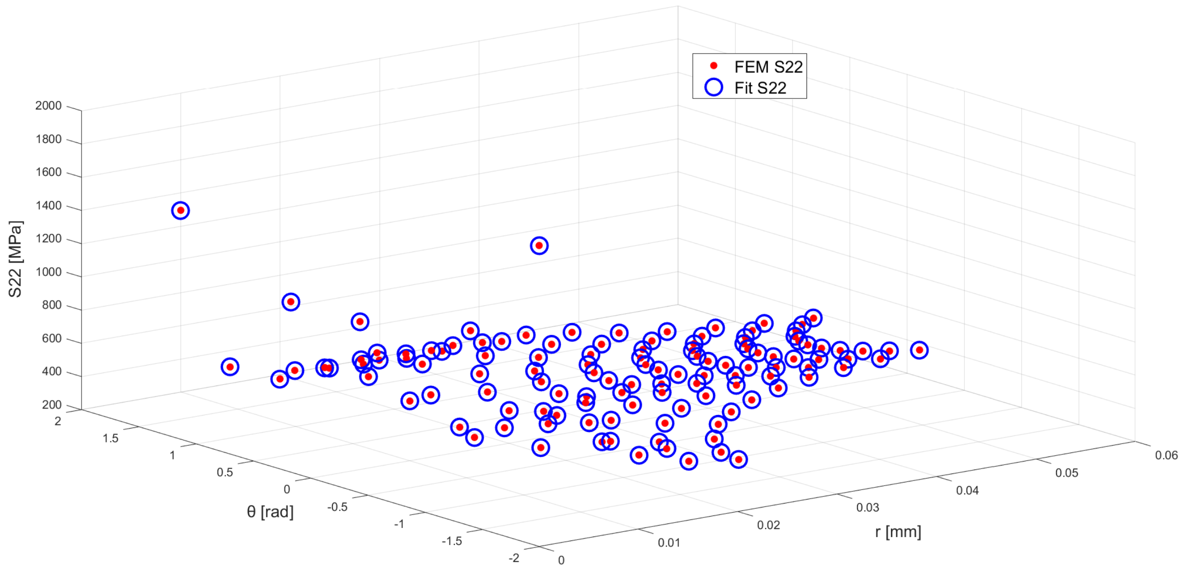

Figure 5.10. S_{22} in H=625 MPa case for 20^o degrees inclined crack.

In Figure 5.11 to 5.13, the raw and fit stress components are plotted for a straight crack configuration, $\alpha = 30^o$. In the following plots, the blue circles represents fit stress component values meanwhile red points represent the raw stress component values collected from ABAQUS. Similar to the previous discussions for other α values; in this case, the maximum errors between stress components S_{ij} and S_{ij}^{fit} for i,j = 1,2 are less than 1 MPa.

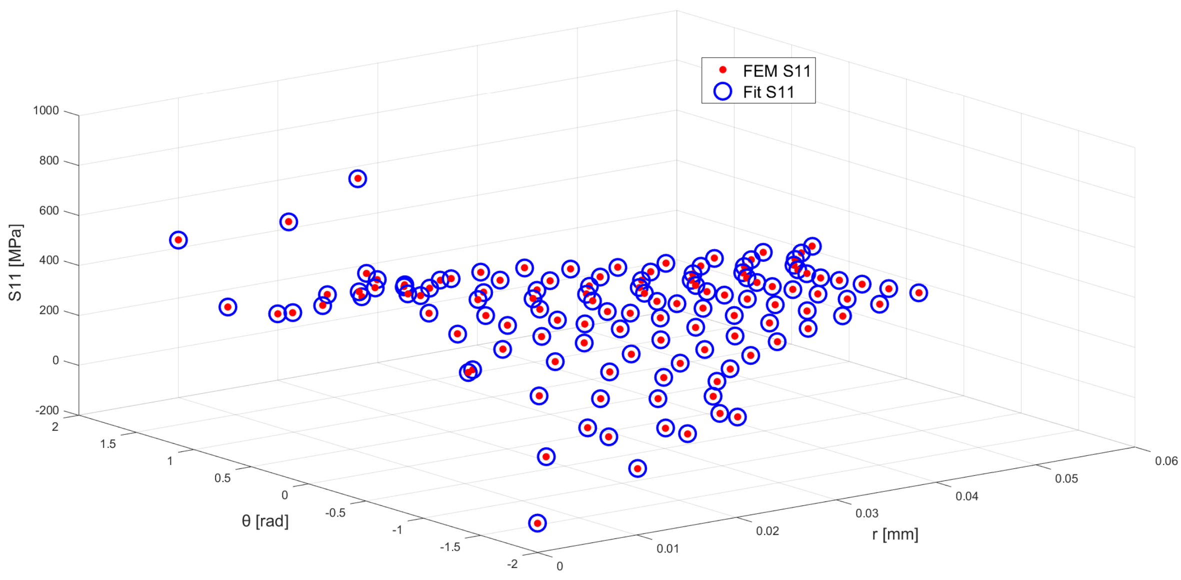

Figure 5.11. S_{11} in H=625 MPa case for 30^o degrees inclined crack.

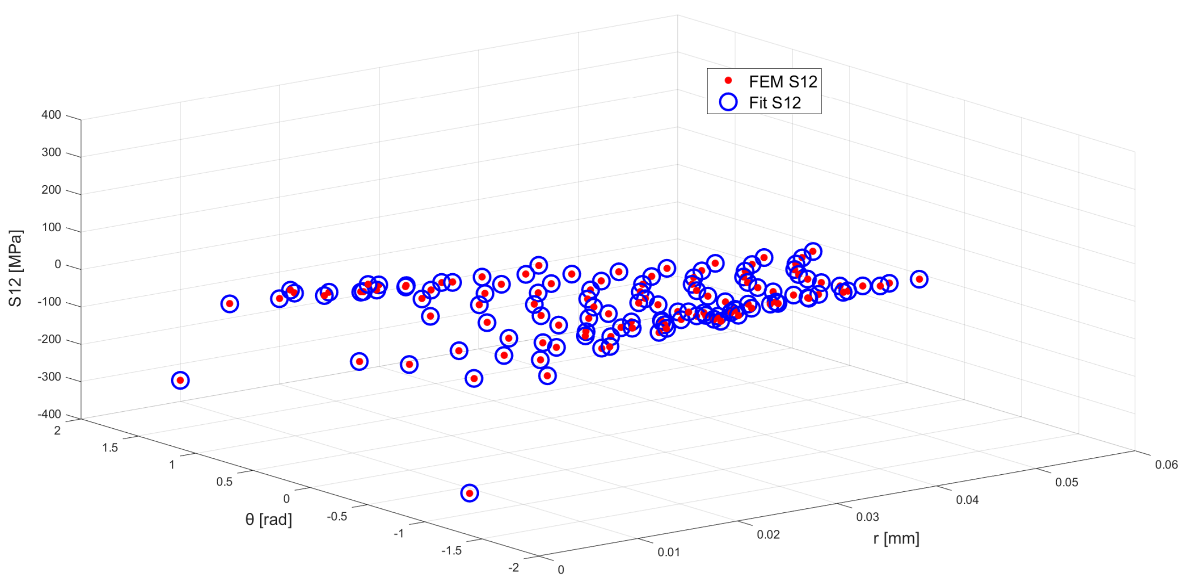

Figure 5.12. S_{12} in H=625 MPa case for 30^o degrees inclined crack.

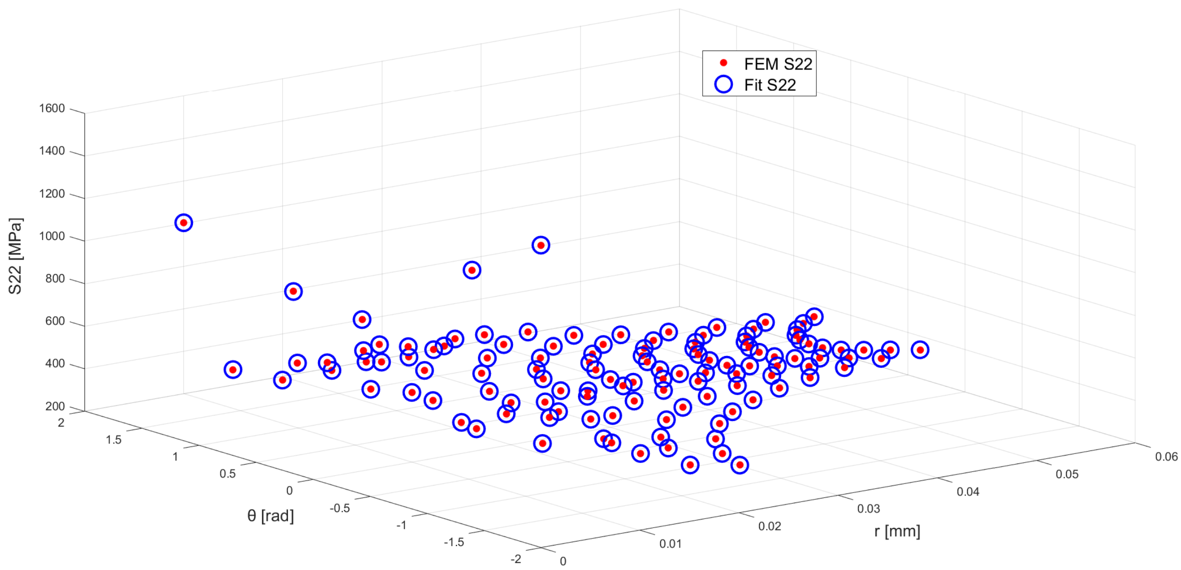

Figure 5.13. S_{22} in H=625 MPa case for 30^o degrees inclined crack.

5.3. 833 MPa Hardening Modulus Case

To generate a hardening modulus, H, equal to 833 MPa, the start and end stress levels of forward transformation are chosen as 200 MPa and 250 MPa for a given ϵ^L magnitude of 0.06, summarized in Table 5.7. The hardening modulus is explicitly calculated as

$$\mathrm{H} = \frac{250 - 200}{0.06}\mathrm{MPa} = 833\ \mathrm{MPa}. \tag{5.3}$$

Table 5.7. Super elastic material properties of NiTi with H=833 MPa

Transformation Strain	0.06
Forward Transformation Start Stress	200 MPa
Forward Transformation End Stress	250 MPa

For the fitting variables $\{K^{eq}, m_{ij}, n_{ij}, v_{ij}, w_{ij}\}$ based on the algorithm followed, initial values are to be assigned. In this case the set of initial values are chosen as $\{0.1\mathrm{MPa\ m}^{-1/2}, 1.1, 1.2, 1.5, 1\}$, respectively. Stress intensity factor values for 833 MPa hardening modulus is tabulated in Table 5.8 along with the tabulated fitting parameters as a function crack angle α in Tables 5.9 to 5.12.

Table 5.8. K^{eq}, A_{11}, A_{12}, A_{22} values with respect to crack angle α given H=833 MPa

α	0^o	10^o	20^o	30^o
K^{eq} [MPa$\sqrt{m}$]	180	140	160	130
A_{11} [MPa]	0.3	1.9	5.3	4.2
A_{12} [MPa]	-166.9	-147	-178.3	-161.4
A_{22} [MPa]	33.4	27.1	15.3	38.1

Table 5.9. Fit parameter values for straight crack angle of H=833 MPa

m_{11}	n_{11}	v_{11}	w_{11}
0.0007	1.9700	0.0006	0.8400
m_{12}	n_{12}	v_{12}	w_{12}
3.0936	3.9220	11.0780	1.3472
m_{22}	n_{22}	v_{22}	w_{22}
-0.0011	2.5700	-0.0009	0.0005

Table 5.10. Fit parameter values for 10^o degrees crack angle of H=833 MPa

m_{11}	n_{11}	v_{11}	w_{11}
0.2300	1.4800	0.3200	-0.6500
m_{12}	n_{12}	v_{12}	w_{12}
1.5068	-7.8555	9.3623	1.0421
m_{22}	n_{22}	v_{22}	w_{22}
1.0300	0.9800	0.0500	0.0000

Table 5.11. Fit parameter values for 20^o degrees crack angle of H=833 MPa

m_{11}	n_{11}	v_{11}	w_{11}
0.0900	2.1200	0.2100	0.9000
m_{12}	n_{12}	v_{12}	w_{12}
-9.0705	-9.7569	8.8848	1.1377
m_{22}	n_{22}	v_{22}	w_{22}
1.8200	5.9200	4.1000	-0.0001

Table 5.12. Fit parameter values for 30^o degrees crack angle of H=833 MPa

m_{11}	n_{11}	v_{11}	w_{11}
0.0800	1.9900	0.2800	0.8900
m_{12}	n_{12}	v_{12}	w_{12}
0.2297	0.0000	0.2297	1.0696
m_{22}	n_{22}	v_{22}	w_{22}
-3.5000	4.4800	-0.4900	0.0000

Both the raw and fit data for stress components, S_{ij} and S_{ij}^{fit} with i,j = 1,2 , for H=833 MPa level are plotted as function of radial coordinate, r and θ for each set of crack inclination angle set of $\{0^o, 10^o, 20^o, 30^o\}$. In Figure 5.14 to 5.16, the raw and fit stress components are plotted for a straight crack configuration, $\alpha = 0^o$. In the following plots, the blue circles represents fit stress component values meanwhile red points represent the raw stress component values collected from ABAQUS. In each fitting operation, the maximum error is confined to the interval [0.5, 2] MPa.

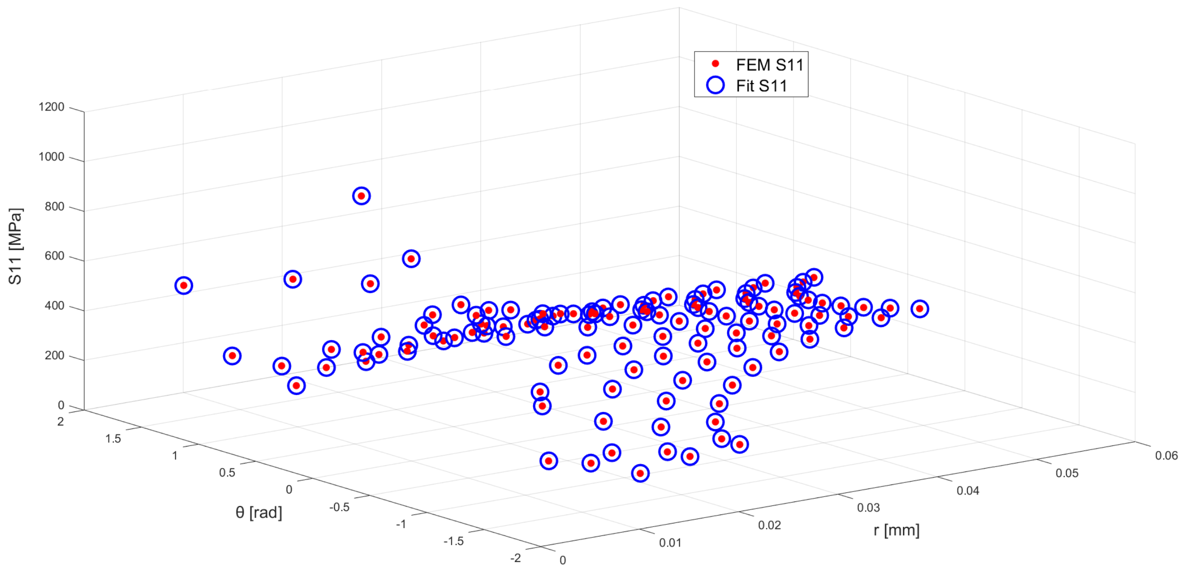

Figure 5.14. S_{11} in H=833 MPa case for straight crack.

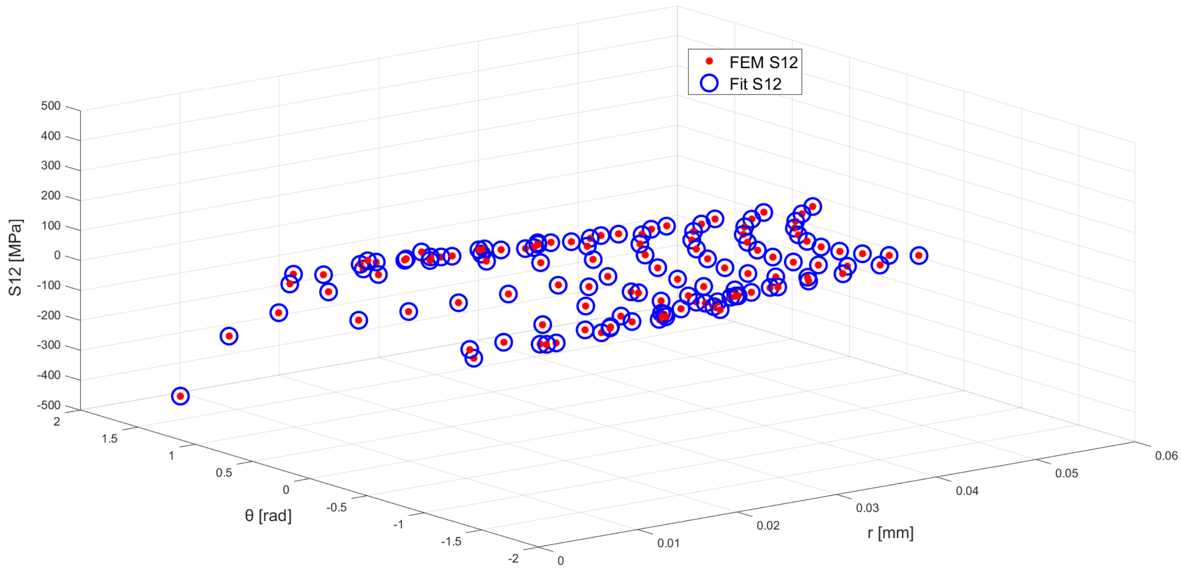

Figure 5.15. S_{12} in H=833 MPa case for straight crack.

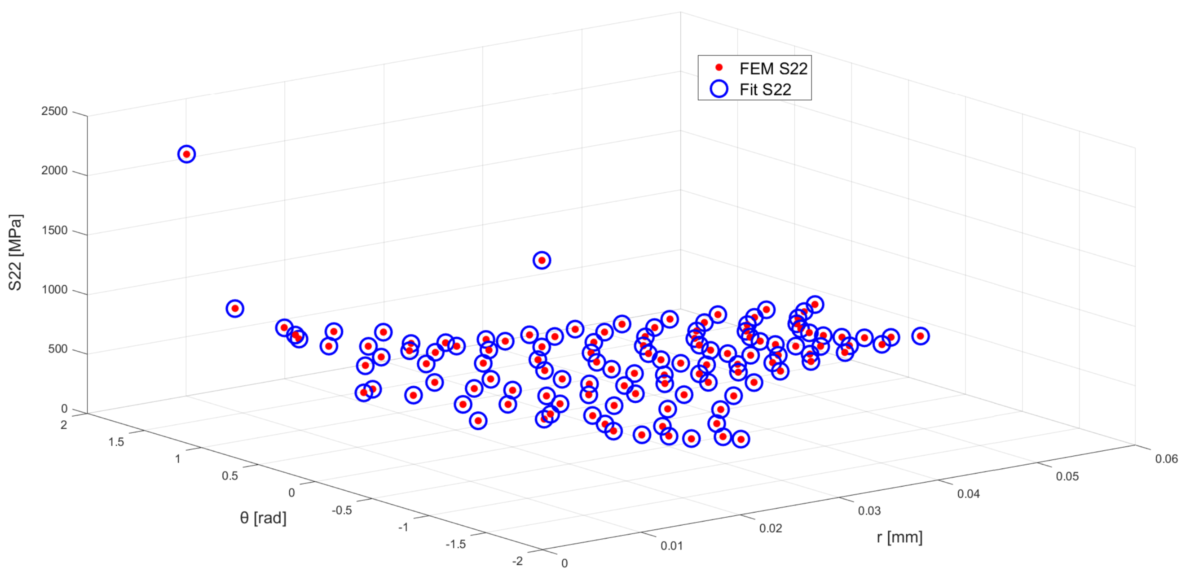

Figure 5.16. S_{22} in H=833 MPa case for straight crack.

In Figure 5.17 to 5.19, the raw and fit stress components are plotted for a straight crack configuration, $\alpha = 10^o$. In the following plots, the blue circles represents fit stress component values meanwhile red points represent the raw stress component values collected from ABAQUS. In these plots, the maximum error remains less than 2 MPa.

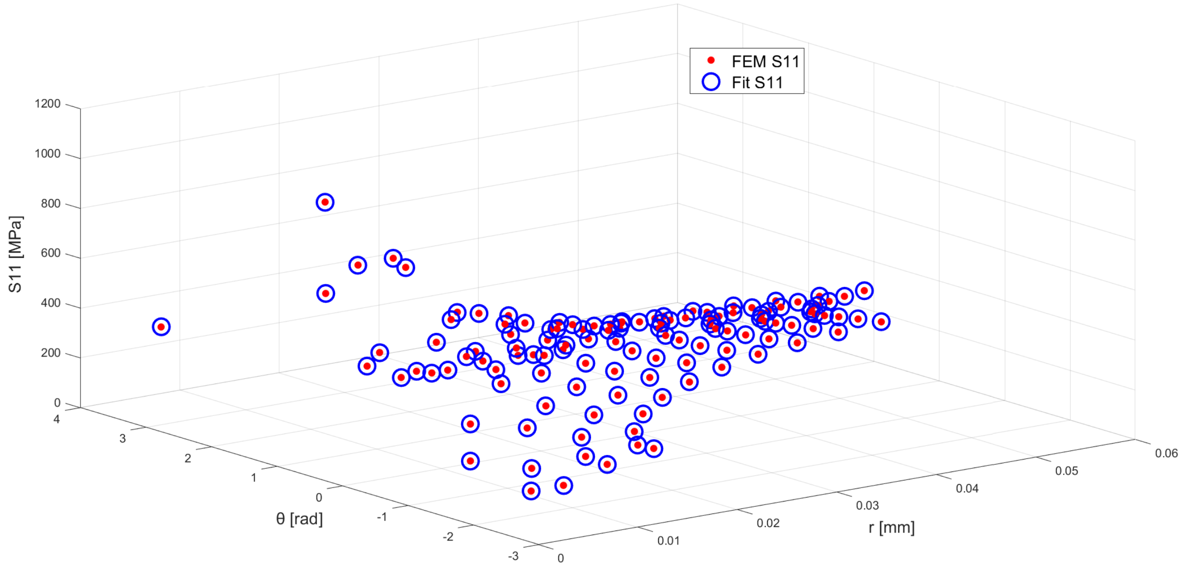

Figure 5.17. S_{11} in H=833 MPa case for 10^o degrees inclined crack.

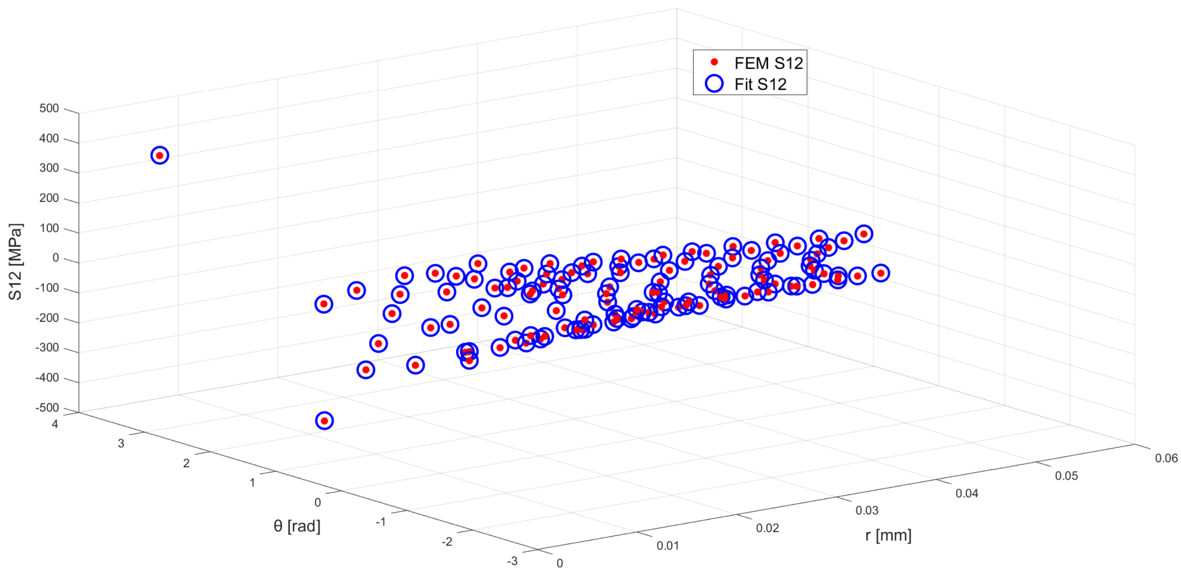

Figure 5.18. S_{12} in H=833 MPa case for 10^o degrees inclined crack.

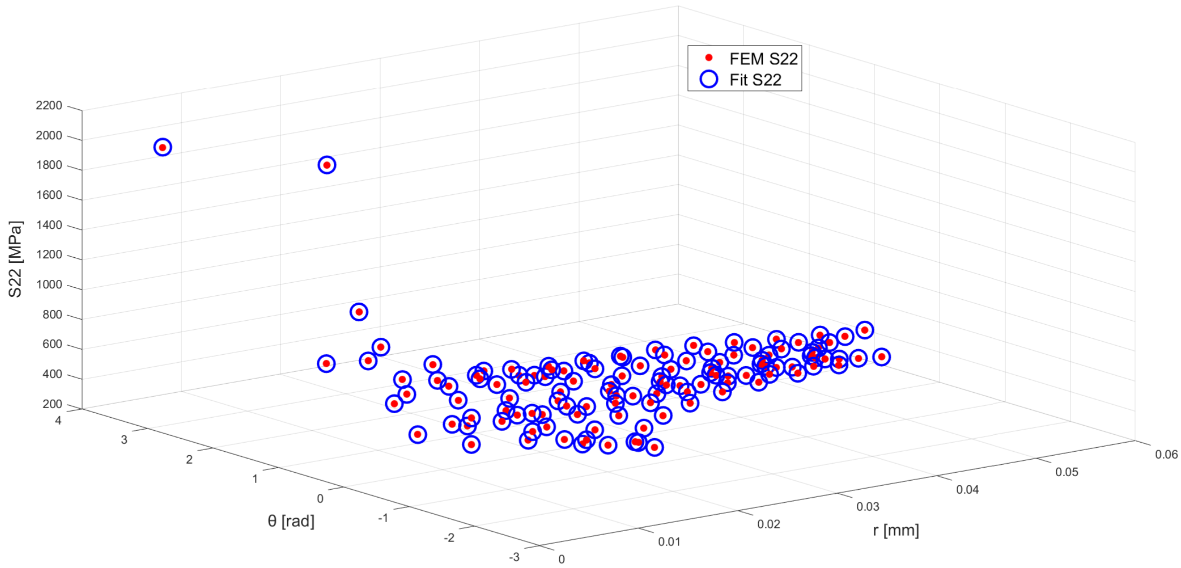

Figure 5.19. S_{22} in H=833 MPa case for 10^o degrees inclined crack.

In Figure 5.20 to 5.22, the raw and fit stress components are plotted for a straight crack configuration, $\alpha = 20^o$. In the following plots, the blue circles represents fit stress component values meanwhile red points represent the raw stress component values collected from ABAQUS. In each stress component, the maximum relative error does not exceed 0.2% with respect to the maximum stress level.

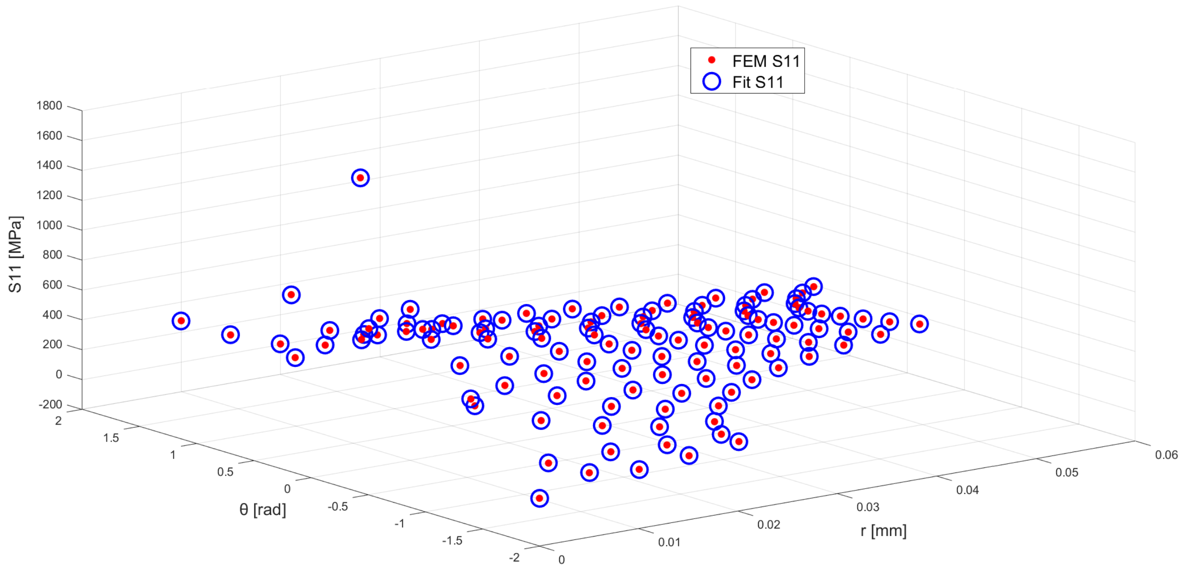

Figure 5.20. S_{11} in H=833 MPa case for 20^o degrees inclined crack.

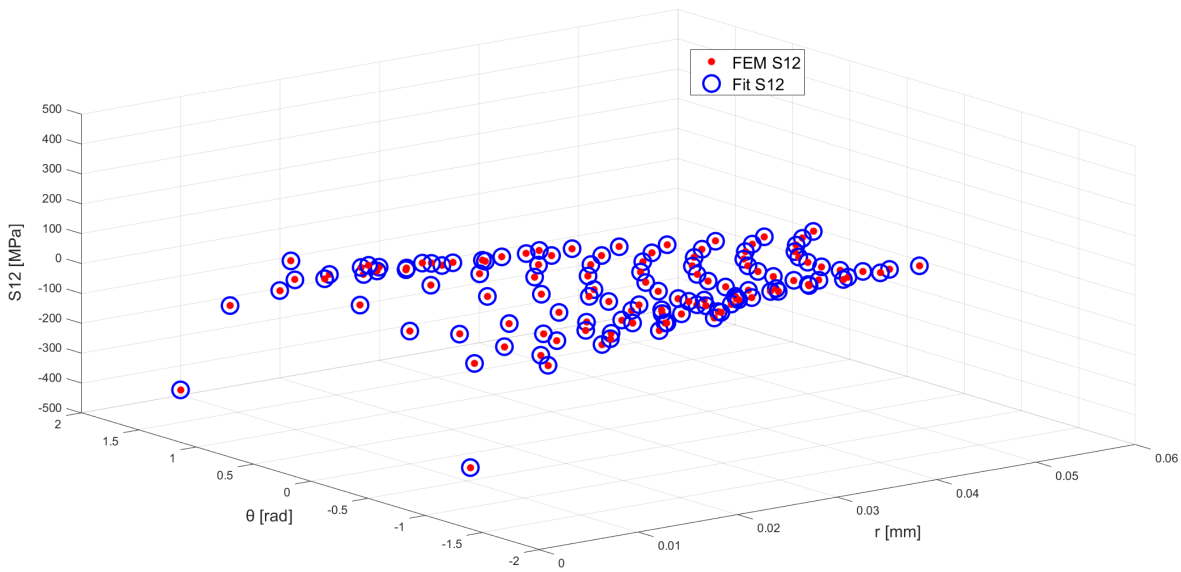

Figure 5.21. S_{12} in H=833 MPa case for 20^o degrees inclined crack.

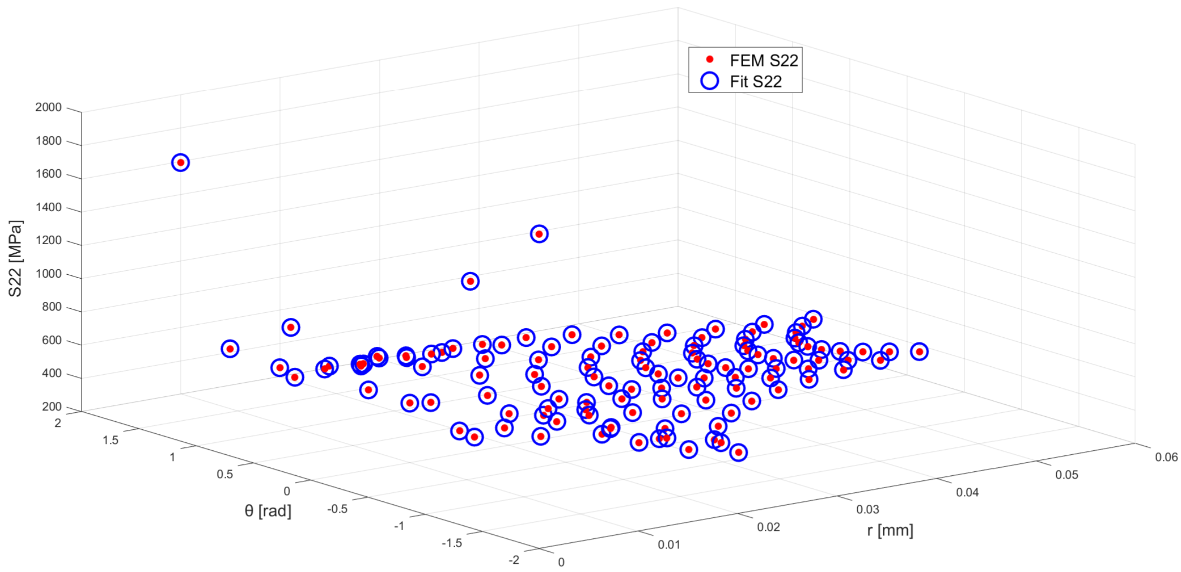

Figure 5.22. S_{22} in H=833 MPa case for 20^o degrees inclined crack.

In Figure 5.23 to 5.25, the raw and fit stress components are plotted for a straight crack configuration, $\alpha = 30^o$. In the following plots, the blue circles represents fit stress component values meanwhile red points represent the raw stress component values collected from ABAQUS. The absolute value for the maximum error in fitting of each stress component does not exceed 1 MPa.

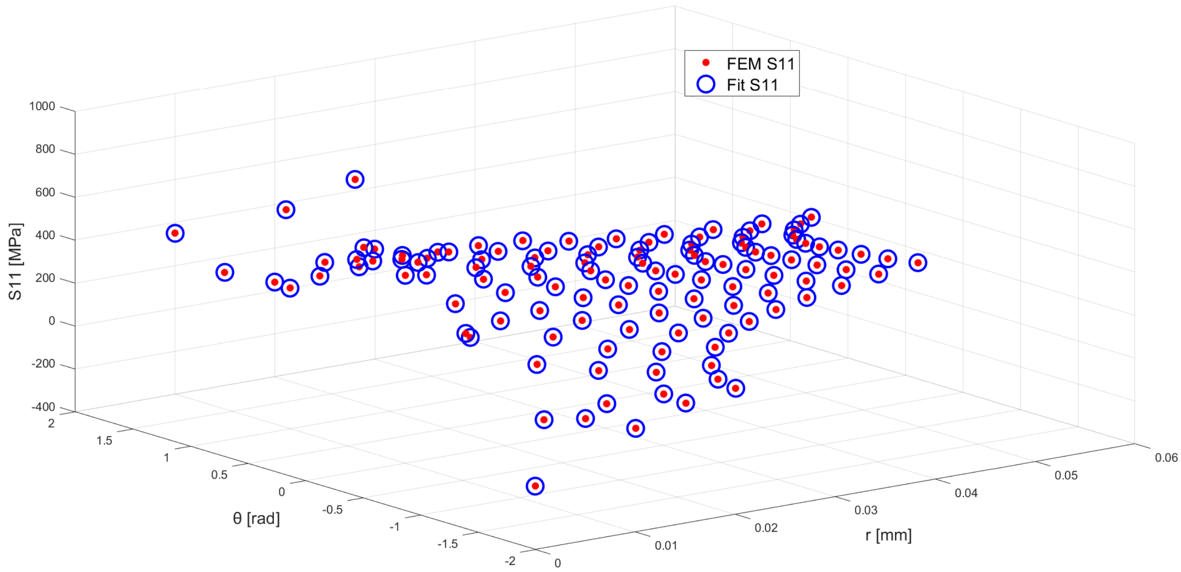

Figure 5.23. S_{11} in H=833 MPa case for 30^o degrees inclined crack.

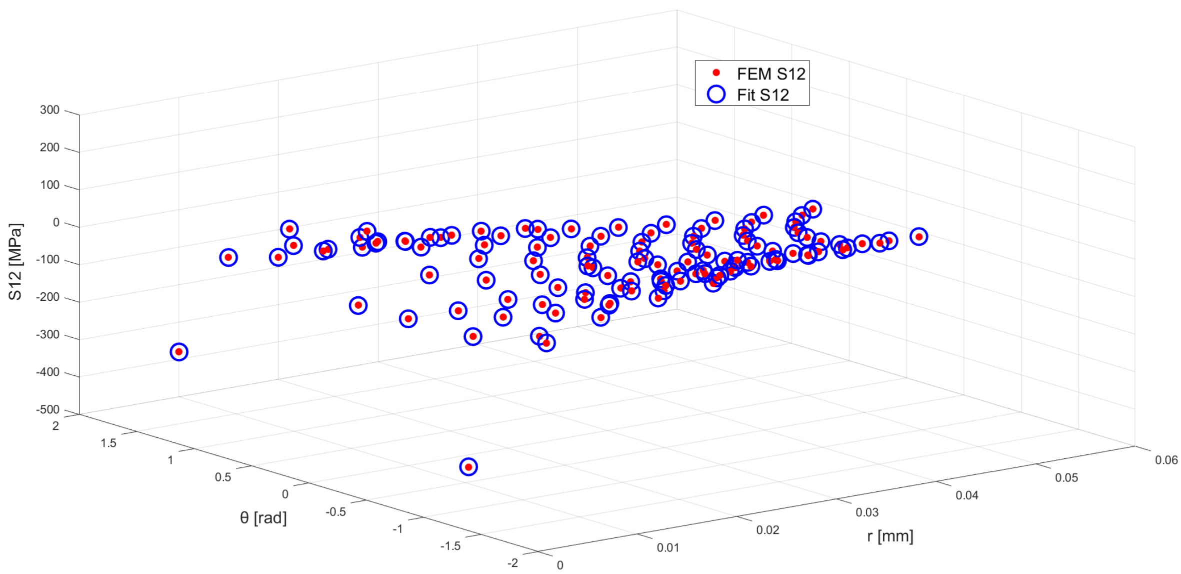

Figure 5.24. S_{12} in H=833 MPa case for 30^o degrees inclined crack.

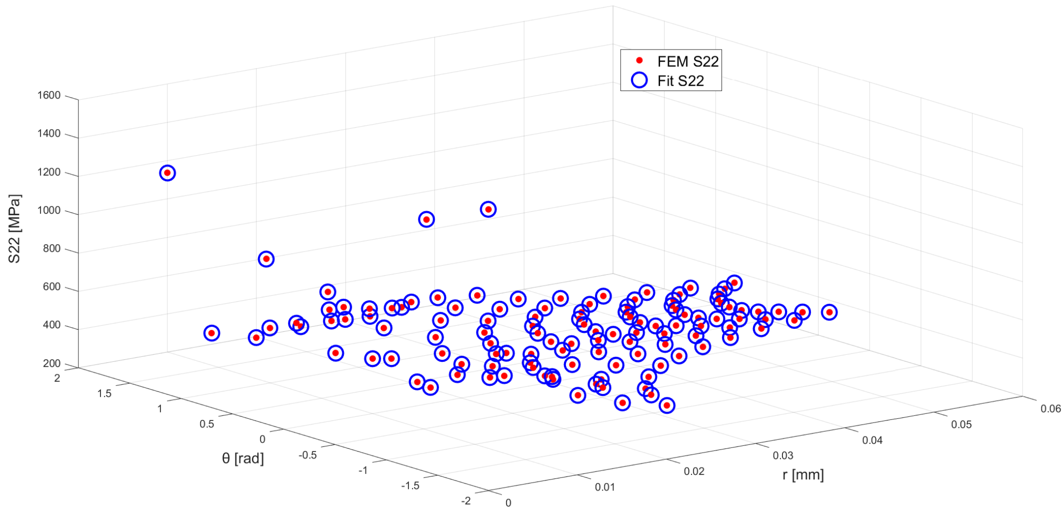

Figure 5.25. S_{22} in H=833 MPa case for 30^o degrees inclined crack.

5.4. 1250 MPa Hardening Modulus Case

To generate a hardening modulus, H, equal to 1250 MPa, the start and end stress levels of forward transformation are chosen as 200 MPa and 250 MPa for a given ϵ^L magnitude of 0.06, summarized in Table 5.13. The hardening modulus is explicitly calculated as

$$\mathrm{H} = \frac{250 - 200}{0.04}\mathrm{MPa} = 1250\ \mathrm{MPa}. \tag{5.4}$$

Table 5.13. Superelastic material properties of NiTi with H=1250 MPa

Transformation Strain	0.04
Forward Transformation Start Stress	200 MPa
Forward Transformation Start Stress	250 MPa

For the fitting variables $\{K^{eq}, m_{ij}, n_{ij}, v_{ij}, w_{ij}\}$ based on the algorithm followed, initial values are to be assigned. In this case the set of initial values are chosen as $\{0.1\mathrm{MPa\ m}^{-1/2}, 1.1, 1.2, 1.5, 1\}$, respectively. Stress intensity factor values for 1250 MPa hardening modulus is tabulated in Table 5.14 along with the tabulated fitting parameters as a function crack angle α in Tables 5.15 to 5.18.

Table 5.14. K^{eq}, A_{11}, A_{12}, A_{22} values with respect to crack angle α given H=1250 MPa

α	0^o	10^o	20^o	30^o
K^{eq} [MPa$\sqrt{m}$]	200	150	170	130
A_{11} [MPa]	5.68	5.2	6.75	9.7
A_{12} [MPa]	-185	-164.2	-196.5	-153
A_{22} [MPa]	25.44	27.6	11.05	34.94

Table 5.15. Fit parameter values for straight crack angle of H=1250 MPa

m_{11}	n_{11}	v_{11}	w_{11}
0.0018	2.3700	0.0015	0.8870
m_{12}	n_{12}	v_{12}	w_{12}
3.1606	3.9075	11.0557	1.3469
m_{22}	n_{22}	v_{22}	w_{22}
-0.0006	2.4400	-0.0002	-0.0005

Table 5.16. Fit parameter values for 10^o degrees crack angle of H=1250 MPa

m_{11}	n_{11}	v_{11}	w_{11}
0.3100	1.4200	0.3700	-0.6600
m_{12}	n_{12}	v_{12}	w_{12}
2.9742	-1.9683	9.2601	1.0715
m_{22}	n_{22}	v_{22}	w_{22}
1.0500	1.0000	0.0500	0.0000

Table 5.17. Fit parameter values for 20^o degrees crack angle of H=1250 MPa

m_{11}	n_{11}	v_{11}	w_{11}
0.1740	2.3500	0.3000	0.9000
m_{12}	n_{12}	v_{12}	w_{12}
-0.8448	1.9023	-2.7472	1.0551
m_{22}	n_{22}	v_{22}	w_{22}
1.4600	4.1500	2.7000	0.0000

Table 5.18. Fit parameter values for 30^o degrees crack angle of H=1250 MPa

m_{11}	n_{11}	v_{11}	w_{11}
0.1400	-2.3400	0.3600	0.9200
m_{12}	n_{12}	v_{12}	w_{12}
-7.1637	16.1593	5.4754	-0.8564
m_{22}	n_{22}	v_{22}	w_{22}
1.8600	5.9700	4.1100	0.0000

Both the raw and fit data for stress components, S_{ij} and S_{ij}^{fit} with i,j = 1,2, for H = 1250 MPa level are plotted as function of radial coordinate, r and θ for each set of crack inclination angle set of $\{0^o, 10^o, 20^o, 30^o\}$. In Figure 5.26 to 5.28, the raw and fit stress components are plotted for a straight crack configuration, $\alpha = 0^o$. In the following plots, the blue circles represents fit stress component values meanwhile red points represent the raw stress component values collected from ABAQUS. The maximum error levels do not exceed 1 MPa between the collected S_{ij} and fitting values of S_{ij}^{fit}, for i, j = 1,2.

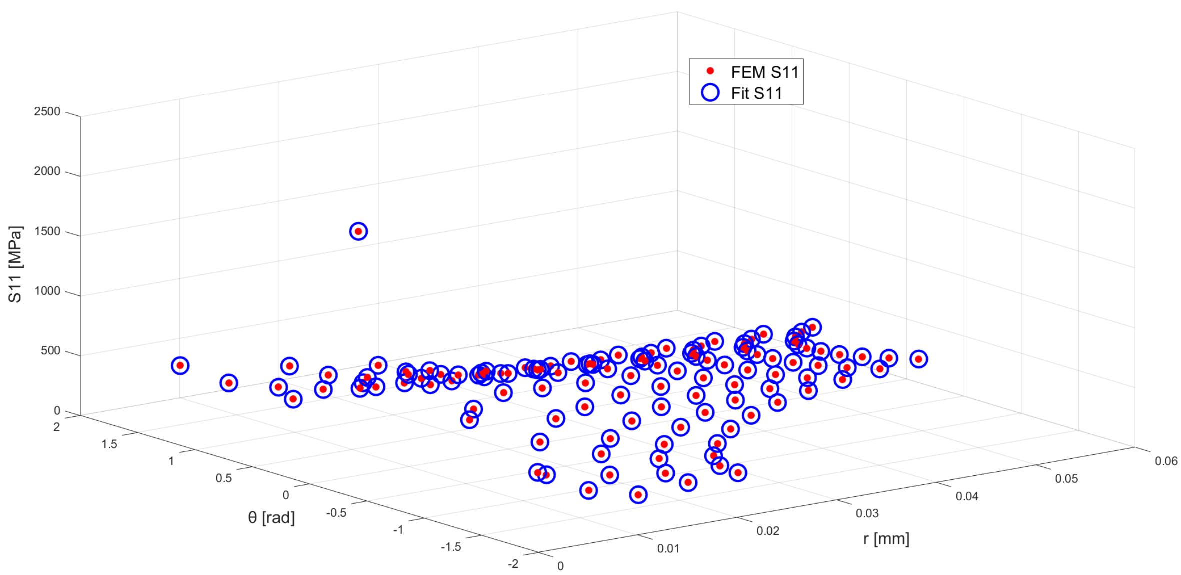

Figure 5.26. S_{11} in H=1250 MPa case for straight crack.

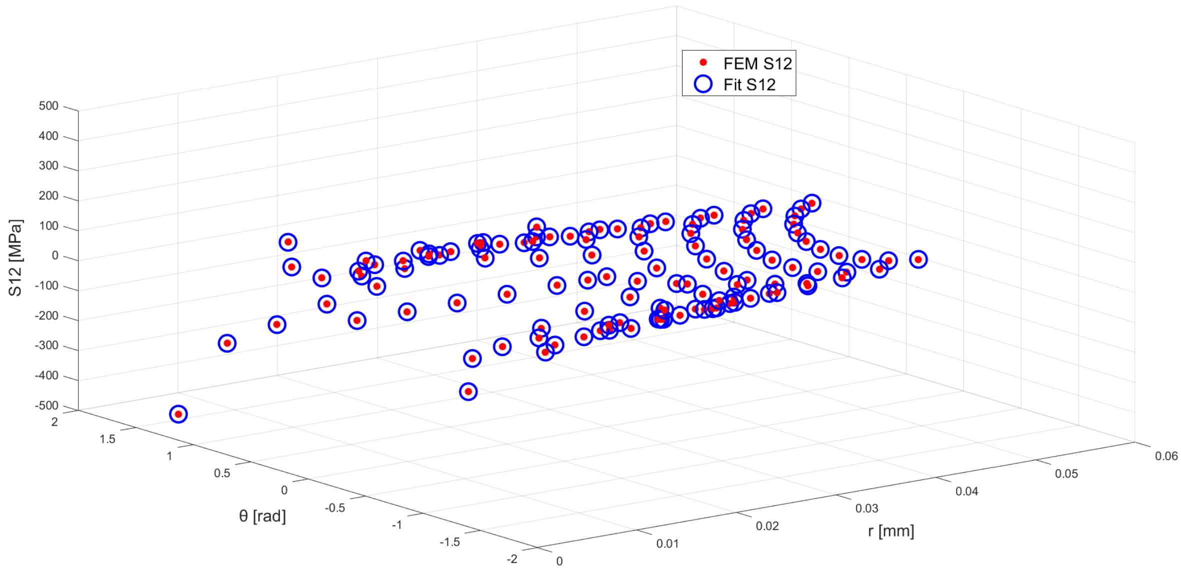

Figure 5.27. S_{12} in H=1250 MPa case for straight crack.

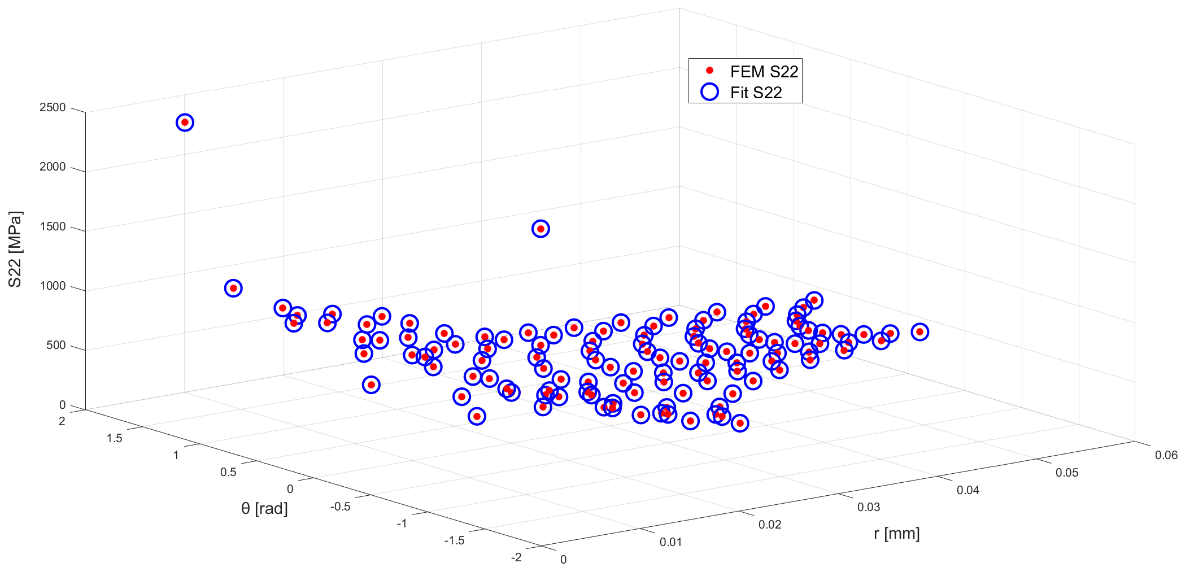

Figure 5.28. S_{22} in H=1250 MPa case for straight crack.

In Figure 5.29 to 5.31, the raw and fit stress components are plotted for a straight crack configuration, $\alpha = 10^o$.

In the following plots, the blue circles represents fit stress component values, meanwhile red points represent the raw stress component values collected from ABAQUS. The maximum absolute error between the fitting and full field finite element analyses data for each stress component is less than 2 MPa.

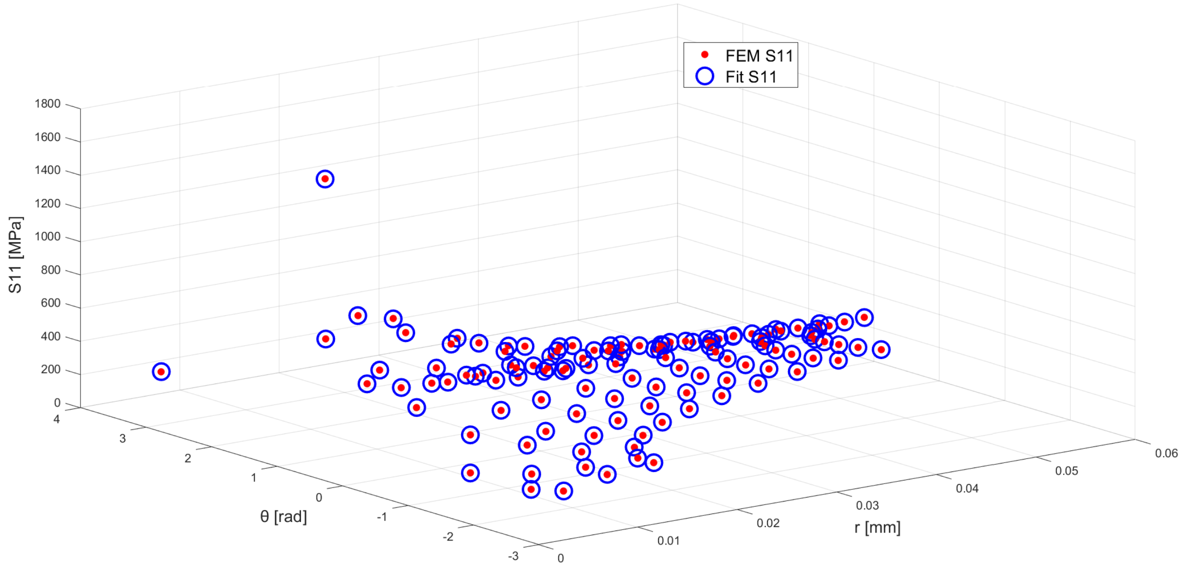

Figure 5.29. S_{11} in H=1250 MPa case for 10^o degrees inclined crack.

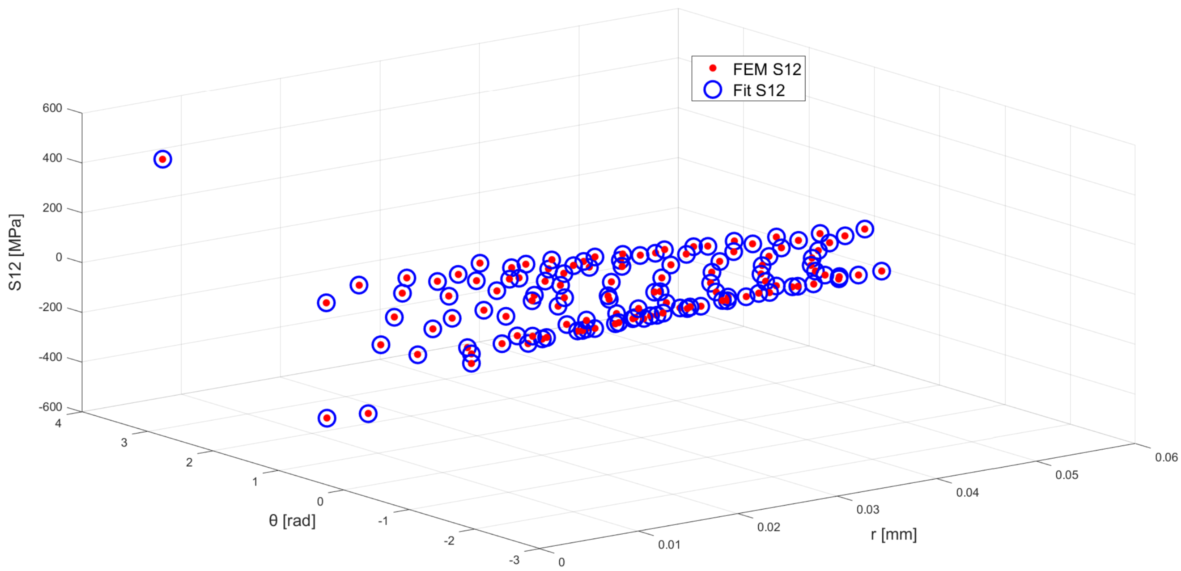

Figure 5.30. S_{12} in H=1250 MPa case for 10 degree inclined crack.

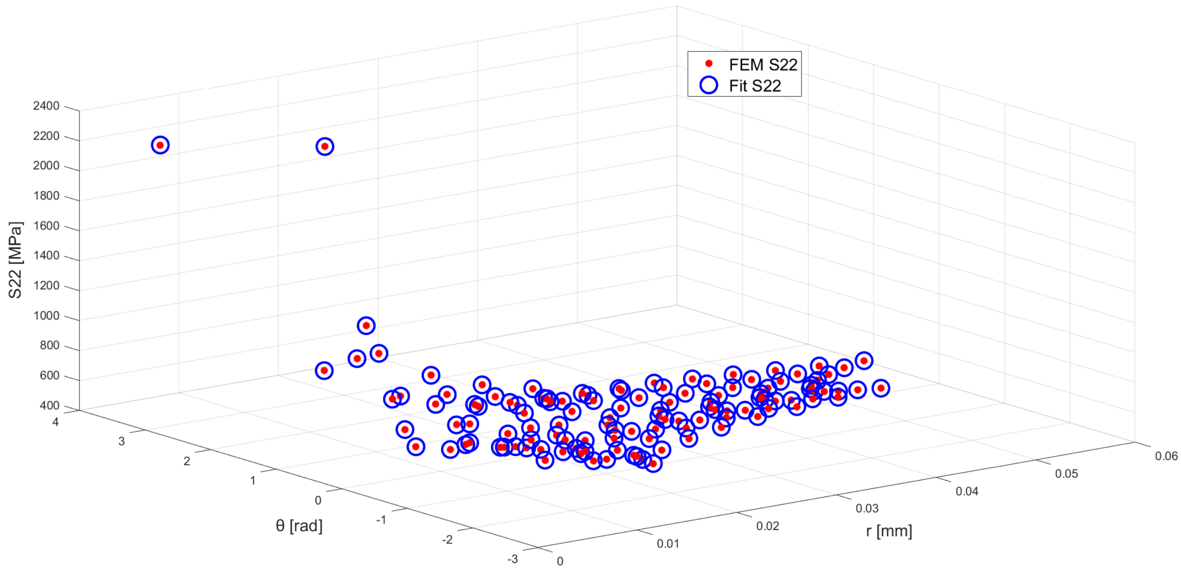

Figure 5.31. S_{22} in H=1250 MPa case for 10^o degrees inclined crack.

In Figure 5.32 to 5.34, the raw and fit stress components are plotted for a straight crack configuration, $\alpha = 20^o$. In the following plots, the blue circles represents fit stress component values meanwhile red points represent the raw stress component values collected from ABAQUS. The maximum error levels do not exceed 1 MPa between the collected S_{ij} and fitting values of S_{ij}^{fit}, for i, j = 1,2. This result ensures the accurate representation of crack tip stress field by the fitting function to be employed in the subsequent discussion.

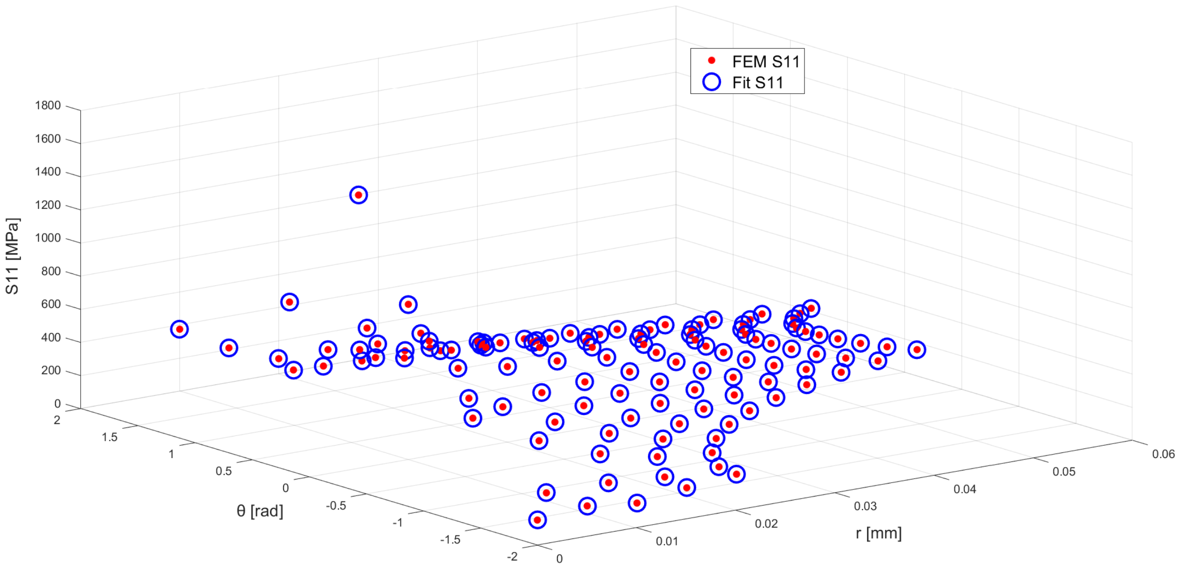

Figure 5.32. S_{11} in H=1250 MPa case for 20^o degrees inclined crack.

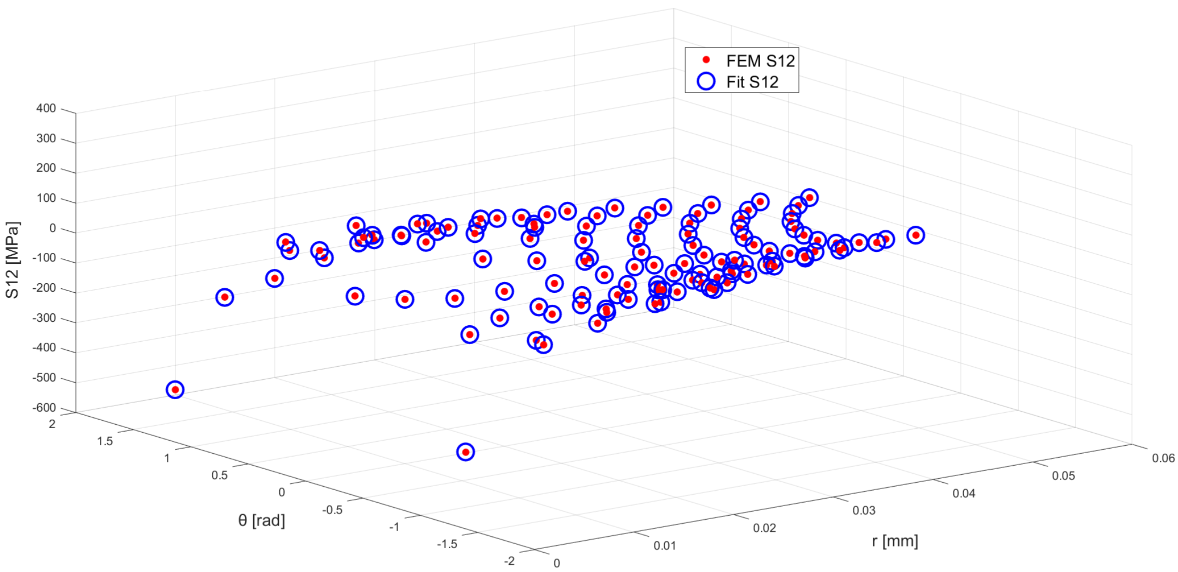

Figure 5.33. S_{12} in H=1250 MPa case for 20^o degrees inclined crack.

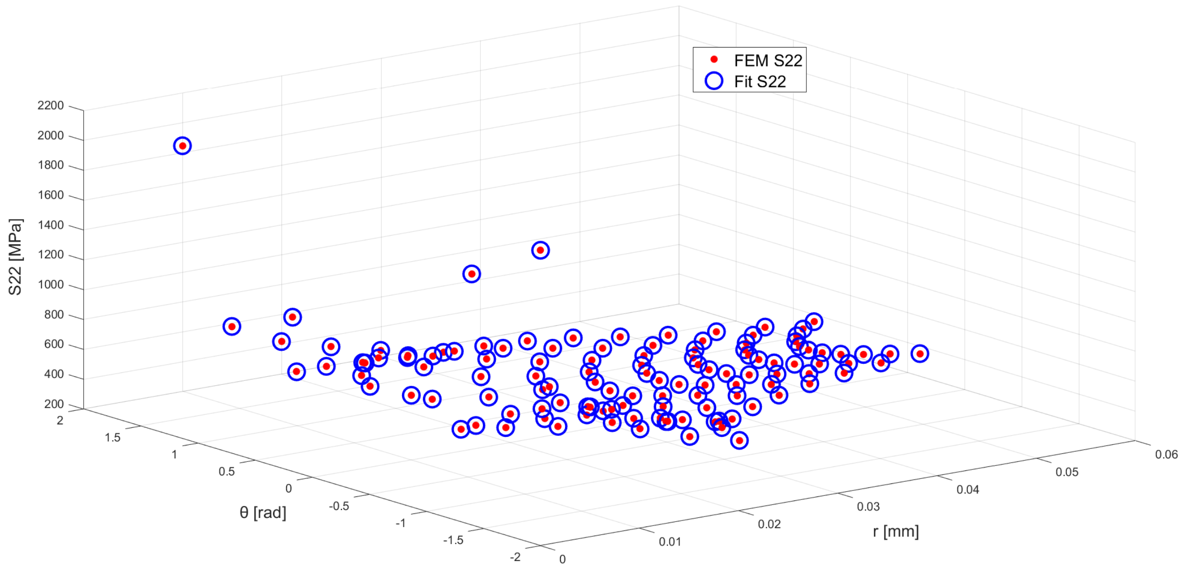

Figure 5.34. S_{22} in H=1250 MPa case for 20^o degrees inclined crack.

In Figure 5.35 to 5.37, the raw and fit stress components are plotted for a straight crack configuration, $\alpha = 30^o$. In the following plots, the blue circles represents fit stress component values meanwhile red points represent the raw stress component values collected from ABAQUS. In each of the regression plots, Figure 5.35 to 5.37, the absolute maximum difference between the finite element analysis and fitting functions is below 1 MPa.

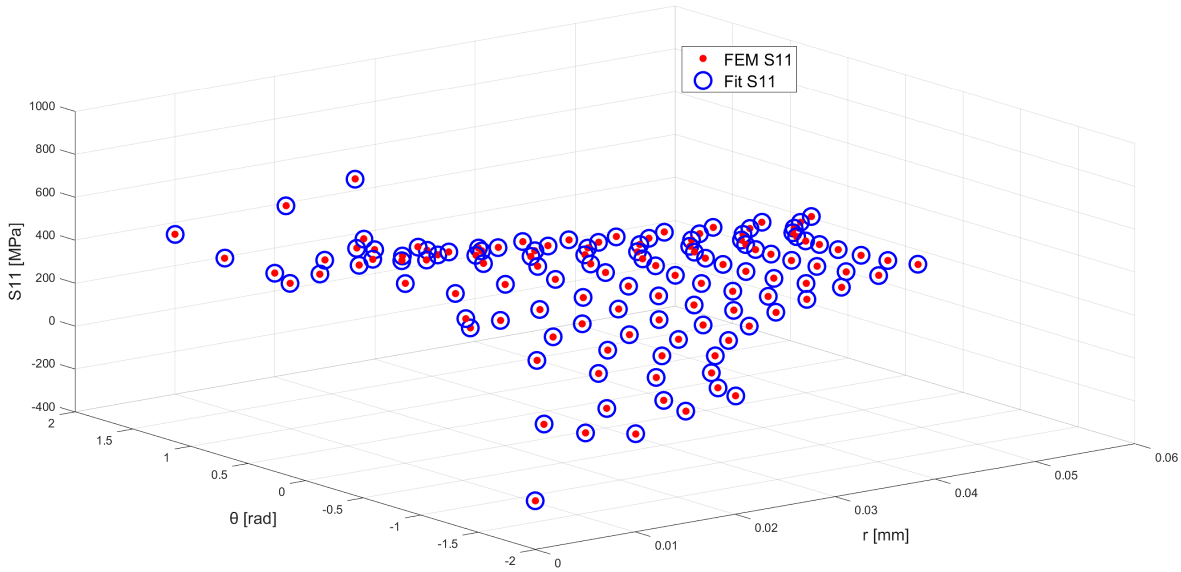

Figure 5.35. S_{11} in H=1250 MPa case for 30^o degrees inclined crack.

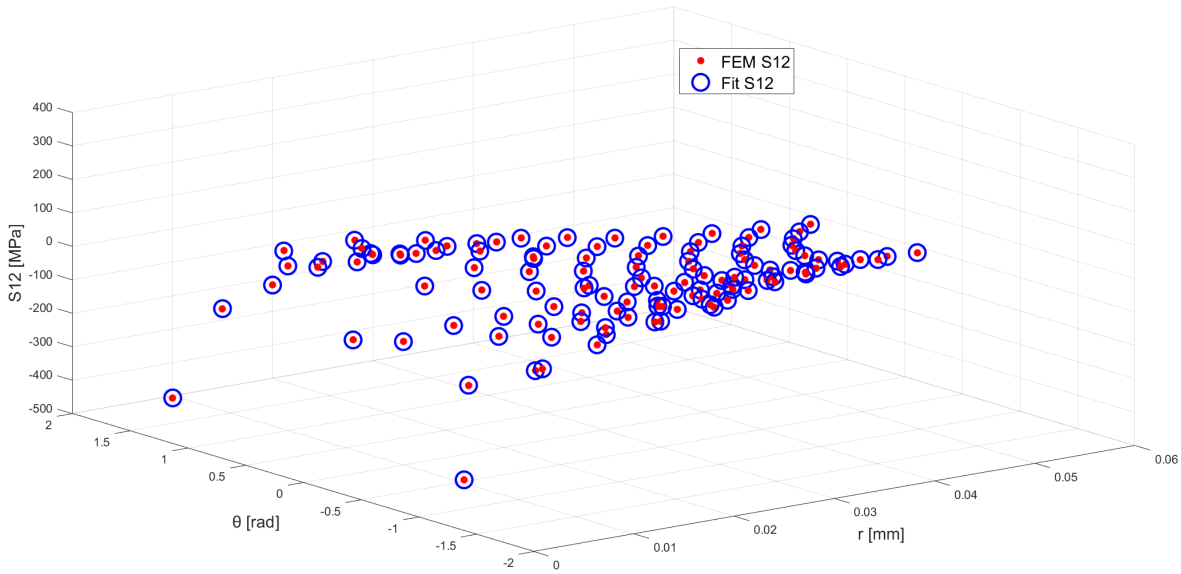

Figure 5.36. S_{12} in H=1250 MPa case for 30^o degrees inclined crack.

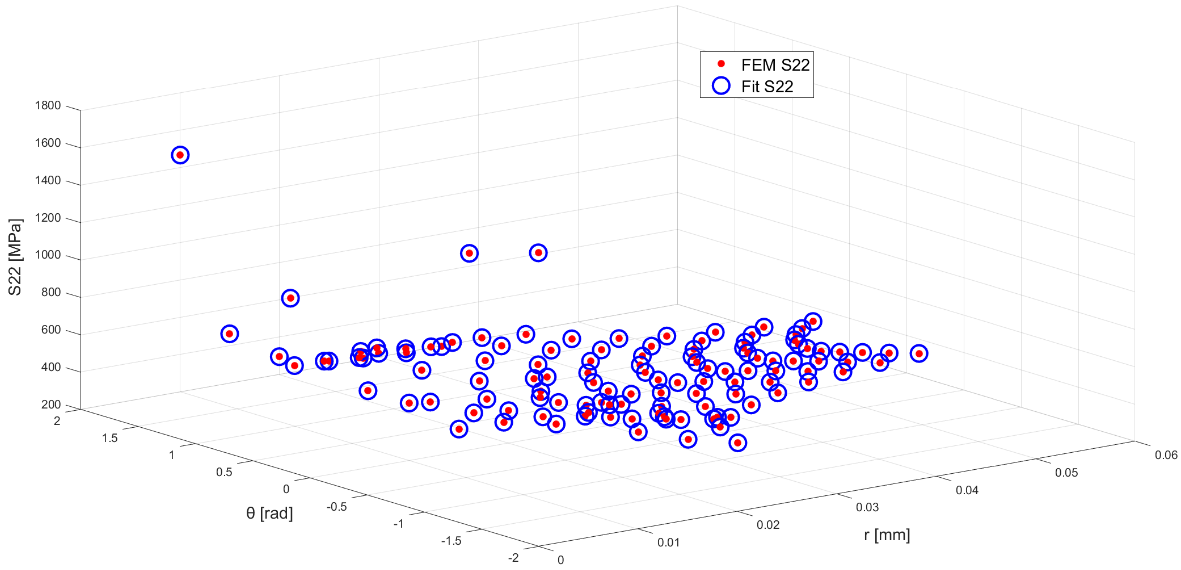

Figure 5.37. S_{22} in H=1250 MPa case for 30^o degrees inclined crack.

6. STRESS TRIAXIALITY CALCULATIONS

6.1. Adaptation of Triaxiality Formulation for SMAs

Stress triaxiality, Q, plays a decisive role on the extent of plastic deformation at the crack tip and in the following expression, it is expressed as

$$Q = \frac{S_m - (S_m)_{SSY}}{S_{MS}}. \tag{6.1}$$

In this expression, S_m and $(S_m)_{SSY}$ are mean stress levels under the presence of martensitic transformation and small scale yielding (SSY), respectively. The conditions of SSY basically employ the linear elastic fracture mechanics with a single asymptotic term neglecting any transformation effects. The mean stress levels are calculated by the arithmetic average of the corresponding stress tensor traces. The pertinent mean stress levels are evaluated at $\theta = 0$ and a radial coordinate, r^*, which is expressed as

$$r^* = \frac{2J}{S_{MS}}. \tag{6.2}$$

In general, r^* value is not coincident with the nodal points along $\theta = 0$; thus, linear interpolation is used for evaluating S_m and $(S_m)_{SSY}$ values. In linear elastic, homogeneous materials; J integral value is contour independent. On the other hand, for shape memory alloys related with the on-going martensitic transformation, the J integral values are contour dependent. For this purpose, J integral values at the tip, namely J^{tip}, are employed throughout the following triaxiality calculations in SMAs. Note that SSY formulation is based on a single parameter, i.e. K^{eq}, and excludes the contributions of high order terms in the asymptotic stress field expansion such as T stress. In this study, three different hardening moduli (H=625, 833 and 1250 MPa) are examined and stress triaxiality effects are calculated.

6.2. Variation of Stress Triaxiality with Hardening Modulus

6.2.1. 625 MPa Hardening Modulus Case

In this section, the triaxiality parameters Q are calculated and tabulated in Table 6.1 against J integral values at the crack tip, J^{tip}, the radial distance r^*, mean stress values, S_m and $(S_m)_{SSY}$. The martensite start stress, S_{MS} for NiTi is chosen as 200 MPa along with a hardening modulus H = 625 MPa which leads to a transformation strain ϵ^L equal to 0.08.

Table 6.1. J^{tip}, r^*, S_m, $(S_m)_{SSY}$ and Q values for hardening modulus H = 625 MPa.

Angle	0^o	10^o	20^o	30^o
J^{tip} J/mm^2	3.597	3.436	2.993	2.37
r^* mm	0.035	0.034	0.030	0.023
S_m MPa	431	403	312	66
$(S_m)_{SSY}$ MPa	922	887	761	265
Q	-2.45	-2.42	-2.24	-0.99

6.2.2. 833 MPa Hardening Modulus Case

In this section, the triaxiality parameters Q are calculated and tabulated in Table 6.2 against J integral values at the crack tip, J^{tip}, the radial distance r^*, mean stress values, S_m and $(S_m)_{SSY}$. The martensite start stress, S_{MS} for NiTi is chosen as 200 MPa along with a hardening modulus H = 833 MPa which leads to a transformation strain ϵ^L equal to 0.06.

Table 6.2. J^{tip}, r^*, S_m, $(S_m)_{SSY}$ and Q values for hardening modulus H = 833 MPa.

Angle	0^o	10^o	20^o	30^o
J^{tip} J/mm^2	3.595	3.430	2.990	2.37
r^* mm	0.036	0.034	0.030	0.023
S_m MPa	410	359	297	183
$(S_m)_{SSY}$ MPa	932	877	761	499
Q	-2.61	-2.59	-2.32	-1.58

6.2.3. 1250 MPa Hardening Modulus Case

In this section, the triaxiality parameters Q are calculated and tabulated in Table 6.3 against J integral values at the crack tip, J^{tip}, the radial distance r^*, mean stress values, S_m and $(S_m)_{SSY}$. The martensite start stress, S_{MS} for NiTi is chosen as 200 MPa along with a hardening modulus H = 1250 MPa which leads to a transformation strain ϵ^L equal to 0.04.

Table 6.3. J^{tip}, r^*, S_m, $(S_m)_{SSY}$ and Q values for hardening modulus H = 1250 MPa.

Angle	0^o	10^o	20^o	30^o
J^{tip} J/mm^2	3.592	3.431	2.990	2.37
r^* mm	0.036	0.034	0.030	0.023
S_m MPa	398	384	313	300
$(S_m)_{SSY}$ MPa	923	906	833	686
Q	-2.62	-2.61	-2.60	-1.93

6.2.4. Stress Triaxiality and Hardening Modulus Trend

The variation of stress triaxiality, Q, and hardening modulus, H, is plotted in Figure 6.1 for different crack angles, α. As a first insight, it is to be noted that the increase in crack angle α leads to a pronounced increase in stress triaxiality Q. This trend is closely related with the fact that K^{eq} levels increase with the angle α; and therefore, the martensitic transformation effects are restricted in response to increase in α magnitudes complying with the high transformation constraint measure Q. Furthermore, The increase in hardening levels, suppress the completion of the martensitic transformation leading to higher levels of elastic stress fields ahead of the crack tip. This retarded transformation effect with a high value of H promotes Q levels.

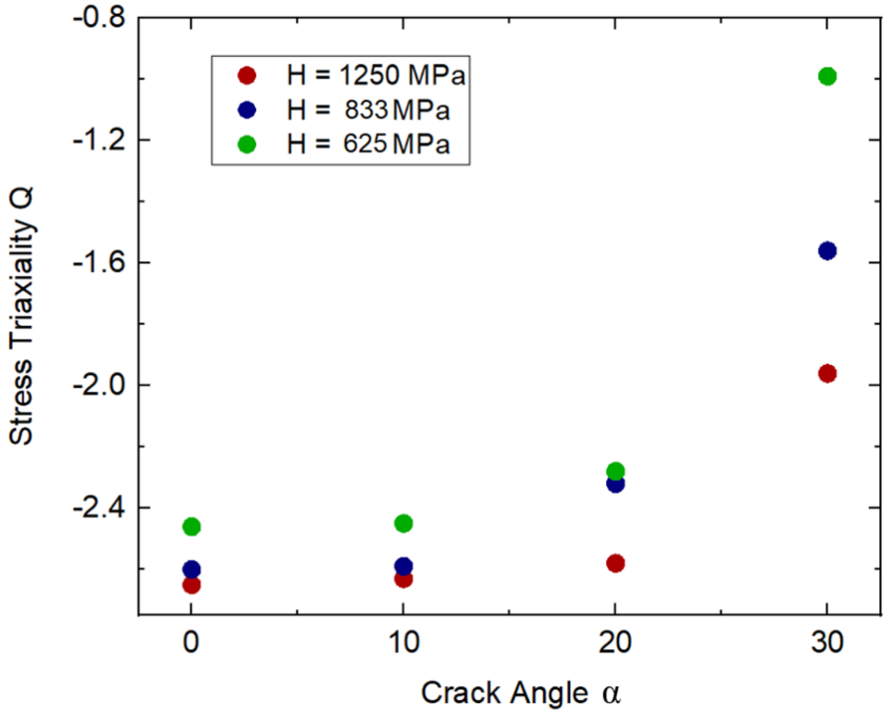

Figure 6.1. Stress triaxiality, Q, versus crack angle α is plotted as a function of hardening modulus, H = 650, 833 and 1250 MPa.

6.3. Variation of Stress Triaxiality with Transformation Strain

In order to clarify the effect of martensitic transformation strain on stress triaxiality parameter Q, the very same plane strain samples on ABAQUS are utilized. The transformation strain levels, ϵ^L, are varied from 0.04 to 0.08 with 0.02 increments. The forward martensitic transformation start and end stresses, S_{MS} and S_{MF} are set as 200 MPa and 205 MPa, respectively. These limiting stresses are chosen to minimize the hardening effect.

6.3.1. 4% Transformation Strain

The variation of stress triaxiality, Q, for 0.04 transformation strain scenario is illustrated under varying crack angles of $\alpha = \{0^o, 10^o, 20^o, 30^o\}$. The variables employed in calculations along with stress triaxiality ratio, Q, are tabulated in Table 6.4.

Table 6.4. J^{tip}, r^*, S_m, $(S_m)_{SSY}$ and Q values are listed for $\epsilon^L = 0.04$

Angle	0^o	10^o	20^o	30^o
J^{tip} J/mm^2	3.592	3.431	2.990	2.373
r^* mm	0.036	0.034	0.030	0.023
S_m MPa	398	373	297	180
$(S_m)_{SSY}$ MPa	923	839	761	262
Q	-2.62	-2.33	-2.32	-0.41

6.3.2. 6% Transformation Strain

The variation of stress triaxiality, Q, for 0.06 transformation strain scenario is illustrated under varying crack angles of $\alpha = \{0^o, 10^o, 20^o, 30^o\}$. The variables employed in calculations along with stress triaxiality ratio, Q, are tabulated in Table 6.5.

Table 6.5. J^{tip}, r^*, S_m, $(S_m)_{SSY}$ and Q values are listed for $\epsilon^L = 0.06$

Angle	0^o	10^o	20^o	30^o
J^{tip} J/mm^2	3.595	3.430	2.990	2.375
r^* mm	0.036	0.034	0.030	0.024
S_m MPa	420	400	297	188
$(S_m)_{SSY}$ MPa	923	838	761	265
Q	-2.51	-2.39	-2.28	-0.38

6.3.3. %8 Transformation Strain

The variation of stress triaxiality, Q, for 0.08 transformation strain scenario is illustrated under varying crack angles of $\alpha = \{0^o, 10^o, 20^o, 30^o\}$. The variables employed in calculations along with stress triaxiality ratio, Q, are tabulated in Table 6.6.

Table 6.6. J^{tip}, r^*, S_m, $(S_m)_{SSY}$ and Q values are listed for $\epsilon^L = 0.08$

Angle	0^o	10^o	20^o	30^o
J^{tip} J/mm^2	3.597	3.436	2.993	2.375
r^* mm	0.035	0.034	0.030	0.023
S_m MPa	431	403	312	207
$(S_m)_{SSY}$ MPa	922	838	761	265
Q	-2.45	-2.37	-2.24	-0.28

6.3.4. Stress Triaxiality and Transformation Strain Trend

Based on the data provided in Tables 6.4 to 6.6, the variation of stress triaxiality, Q, along with the transformation strain is illustrated as a function of crack angle α in Figure 6.2. As can be seen, the triaxiality parameter Q does not exhibit a strong dependence on the level of transformation strain.

This is expected as in all scenarios the applied far-field stress ensures the completion of transformation a head of the crack tip. Thus, the contour integral J^{tip} encloses a fully martensitic region irrespective of the extent of transformation. As a distinguishing remark, the triaxiality Q is dependent on the crack angle, α, strongly related with the stress intensity factor, K^{eq}, effect as discussed earlier on.

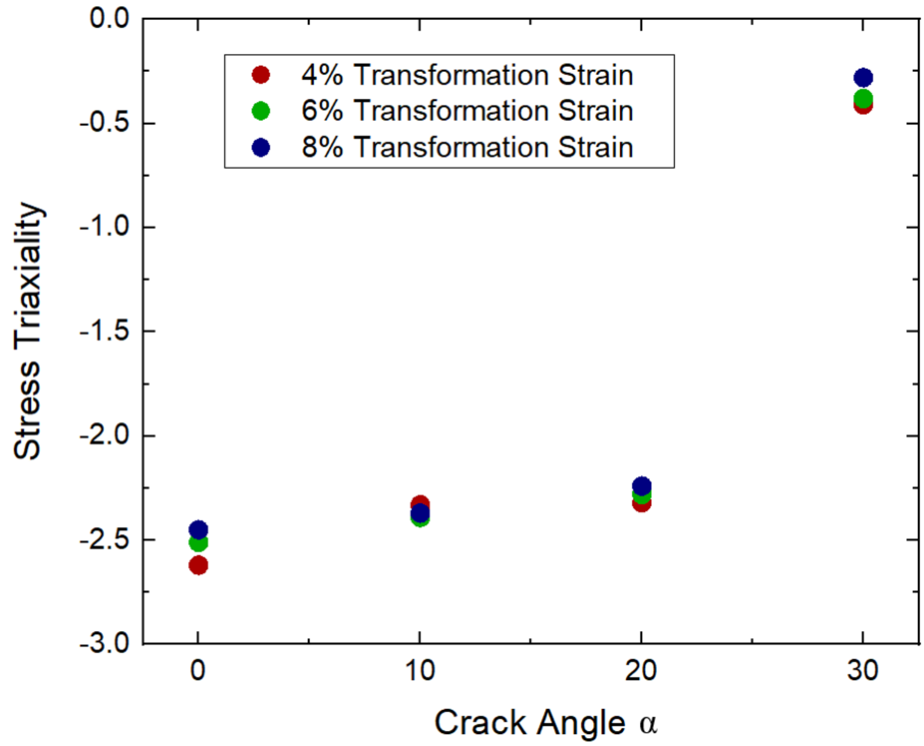

Figure 6.2. Stress triaxiality, Q, versus crack angle α is plotted as a function of transformation strain, ϵ_L.

6.4. Variation of Stress Triaxiality with Transformation Start Stress Level

In this section, the effect of transformation start stress level, S_{MS}, on stress triaxiality, Q, is examined. For this purpose a set of S_{MS} levels, $S_{MS} = \{300, 400, 500\}$ MPa, is employed. In order to disregard any possible hardening effects, the transformation end stress, S_{MF}, levels are chosen as only 5 MPa greater over the total extent of transformation strain with a magnitude of 0.06 such that $S_{MF} = \{305, 405, 505\}$ MPa.

The effect of stress triaxiality on transformation start stress levels are elaborated as a function of crack angles α similar to the previous discussion.

6.4.1. S_{MS} = 300 MPa

Below, J integral values at the crack tip, J^{tip}, the radial distance r^*, and the mean stress values, S_m and $(S_m)_{SSY}$, along with stress triaxiality, Q, values are incorparated into Table 6.7 for S_{MS} = 300 MPa.

Table 6.7. J^{tip}, r^*, S_m, $(S_m)_{SSY}$ and Q values are listed for S_{MS} = 300 MPa

Angle	0^o	10^o	20^o	30^o
J^{tip} J/mm^2	3.543	3.385	2.950	2.344
r^* mm	0.023	0.022	0.019	0.015
S_m MPa	267	147	-345	-1027
$(S_m)_{SSY}$ MPa	656	366	-1269	-932
Q	-1.295	-0.728	-0.401	-0.316

6.4.2. S_{MS} = 400 MPa

Below, J integral values at the crack tip, J^{tip}, the radial distance r^*, and the mean stress values, S_m and $(S_m)_{SSY}$, along with stress triaxiality, Q, values are incorparated into Table 6.8 for S_{MS} = 400 MPa.

Table 6.8. J^{tip}, r^*, S_m, $(S_m)_{SSY}$ and Q values are listed for S_{MS} = 400 MPa

Angle	0^o	10^o	20^o	30^o
J^{tip} J/mm^2	3.537	3.379	2.940	2.339
r^* mm	0.019	0.017	0.0147	0.011
S_m MPa	84.6	-418	-1000	-1416
$(S_m)_{SSY}$ MPa	143	-478	-1269	-2016
Q	-0.146	0.150	0.672	1.50

6.4.3. S_{MS} = 500 MPa

Below, J integral values at the crack tip, J^{tip}, the radial distance r^*, and the mean stress values, S_m and $(S_m)_{SSY}$, along with stress triaxiality, Q, values are incorparated into Table 6.9 for S_{MS} = 500 MPa.

Table 6.9. J^{tip}, r^*, S_m, $(S_m)_{SSY}$ and Q values are listed for S_{MS} = 500 MPa

Angle	0^o	10^o	20^o	30^o
J^{tip} J/mm^2	3.537	3.378	2.944	2.338
r^* mm	0.014	0.0135	0.0196	0.0093
S_m MPa	-6140	-893	-1422	-2441
$(S_m)_{SSY}$ MPa	-602	-980	-1802	-3420
Q	-0.024	0.173	0.759	1.95

Below, in Figure 6.3, the variation of stress triaxiality, Q, with the selected transformation start stress, S_{MS}, levels are ploted as a function of crack angle α. As can be seen, the increase in S_{MS} initially promotes Q levels significantly between 300 MPa to 400 MPa. This is expected due to the fact that increasing stress barrier against martensitic transformation suppresses transformation zone size evolution and related toughening effects.This behavior promotes elastic stress components following linear elastic Poisson effect. On the other hand, there is a saturation between 400 MPa to 500 MPa level. It is to be noted that crack angle α similar to the previous discussion increases the stress triaxiality, Q.

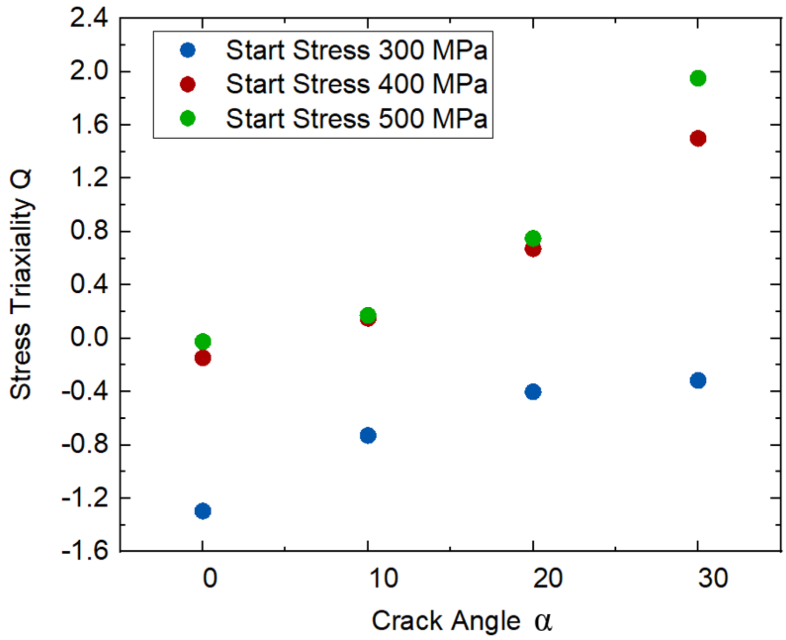

Figure 6.3. Stress triaxiality, Q, versus crack angle α is plotted as a function of transformation start stress, S_{MS}.

6.5. Variation of Stress Triaxiality with Transformation End Stress

In this section, the effect of transformation end stress level, S_{MF}, on stress triaxiality, Q, is examined. For this purpose, a set of S_{MF} levels, $S_{MF} = \{350, 400\}$ MPa, is employed for a given transformation start stress level, $S_{MS} = 300$ MPa. In the following analysis, the transformation strain of 0.06 is employed. The effect of stress triaxiality on transformation start stress levels are elaborated as a function of crack angles α similar to the previous discussion.

6.5.1. $S_{MF} = 350$ MPa

Below, in Table 6.10, J integral values at the crack tip, J^{tip}, the radial distance r^*, and the mean stress values, S_m and $(S_m)_{SSY}$, along with stress triaxiality, Q, values are incorparated for $S_{MF} = 350$ MPa as a function of crack angles α.

Table 6.10. J^{tip}, r^*, S_m, $(S_m)_{SSY}$ and Q values are listed for $S_{MF} = 350$ MPa

Angle	0^o	10^o	20^o	30^o
J^{tip} J/mm^2	3.542	3.384	2.95	2.344
r^* mm	0.0236	0.0225	0.0196	0.0156
S_m MPa	-3590	159	-381	-931
$(S_m)_{SSY}$ MPa	-1905	373	-386	-931
Q	-5.61	-0.713	0.016	0.31

6.5.2. $S_{MF} = 400$ MPa

Below, in Table 6.12, J integral values at the crack tip, J^{tip}, the radial distance r^*, and the mean stress values, S_m and $(S_m)_{SSY}$, along with stress triaxiality, Q, values are incorparated for $S_{MF} = 400$ MPa as a function of crack angles α.

Table 6.11. J^{tip}, r^*, S_m, $(S_m)_{SSY}$ and Q values are listed for $S_{MF} = 400$ MPa

Angle	0^o	10^o	20^o	30^o
J^{tip} J/mm^2	3.542	3.384	2.95	2.344
r^* mm	0.0236	0.0225	0.0196	0.0156
S_m MPa	-3579	164	-361	-1037
$(S_m)_{SSY}$ MPa	-1905	373	-386	-931
Q	-5.58	-0.69	0.08	0.35

Below, in Figure 6.4, the variation of stress triaxiality, Q, as a function of transformation end stress, S_{MF}, and crack angle α based on the examined numerical scenarios. The results show close resemblance to the observed increase trend with α angle in the previous cases. This is again associated with the increase in K^{eq} which suppresses the transformation effects if promoted. On the other hand, the pronounced increase in S_{MF} leads to only a very minor increase.

As under the applied far-field stress levels the martensitic volume fraction, ξ reaches 1 (complete transformation) in the simulations conducted, this result implies that the completion of the transformation is prominent instead of the numerical value of the end stress.

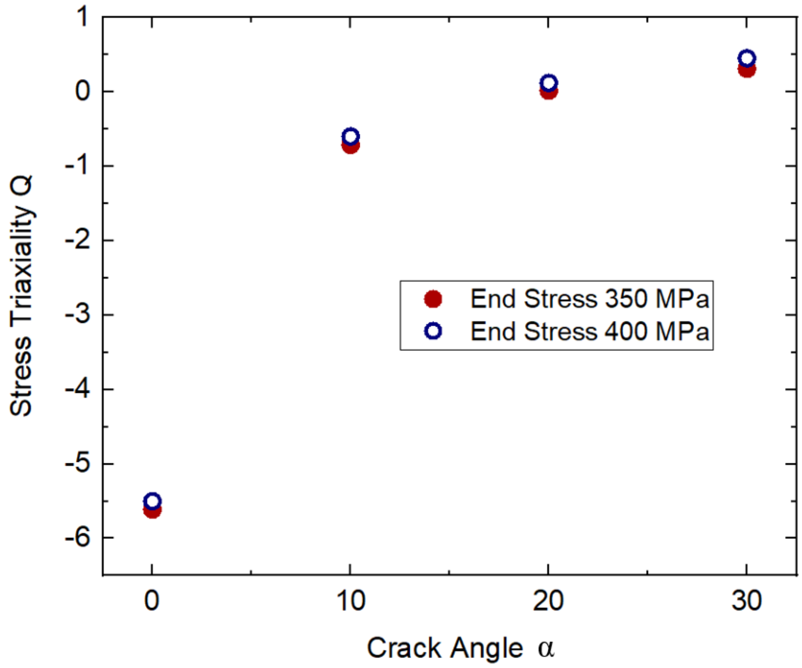

Figure 6.4. Stress triaxiality, Q, versus crack angle α is plotted as a function of transformation end stress, S_{MF}.

7. DISCUSSION

The single parameter approach (K field) to describe fracture response at the crack tip of SMAs have dominated the earlier literature. In small-scale yielding, there assumed to be a J dominant zone a head of the crack-tip and this relation is related by the elastic stress intensity parameter. Similarly J contour integral is also explicitly evaluated for deformation plasticity (no unloading) and linked with stress fields a head of the crack. Based on this perspective, under small scale yielding conditions, a single parameter (e.g., K, J, or CTOD) characterized crack tip conditions allowing to use single critical parameters such as K_c or J_c. In such a case, any one of several parameters (e.g., J, K, or CTOD) will suffice to characterize the crack tip conditions, provided the parameter can be defined unambiguously.

For the presence of significant plastic yielding a head of the crack tip in the case of incremental plasticity, stress values are supposed to be collected from a full field solution using finite element analysis. On the other hand, single-parameter fracture mechanics breaks down in the presence of excessive plasticity or transformation, and this leads to the fact that fracture toughness depends on the size and geometry of the test specimen. This acts as a motivation to develop a more elaborate approach to capture the conditions at the crack tip in a SMA system. The crack tip constraint linked with the thickness effects has a significant role in fracture response of SMAs in engineering applications similar to the samples exhibiting large plastic deformation in the earlier literature. The decrease of fracture toughness values with specimen thickness under excessive plastic deformation can be given as an example on that basis.

Current research aims to investigate constraint effects under Mode I (opening mode) and mixed mode in plane strain condition by using finite element analysis. In order to achieve this goal, two parameter fracture mechanics techniques were proposed to be used. As a major point to be emphasized, the present approach utilizes multi-parameter fracture mechanics methods and this is a novel step for SMAs.

The T stress approach, J–Q theory are examples of two-parameter fracture theories [46-48], and it these methods a secondary variable (e.g., T, Q) had been introduced to characterize the crack tip environment. In this methodology, the first parameter measures the degree of crack-tip deformation, as characterized by J (or equivalently CTOD). The second parameter, characterizes the degree of crack tip constraint, which quantifies the level of deviation of stress/strain fields from HRR fields. These approaches implicitly assume that the crack tip fields are characterized by two independent parameters in contrast to single-parameter fracture mechanics which employs either K^{eq} or J. It is to be noted that, a second parameter use (such as T stress) under large scale yielding/martensitic transformation conditions, does not reflect the full field stress around crack tip as T-stress originates from the linear elastic asymptotic expansion. On the other hand, large transformation or plastic strains violate the assumptions employed in linear elastic fracture mechanics.

In the present work, the full field stress field collected from finite element analysis have been fitted to a closed-form model for NiTi single edge cracked specimen such that the equivalent stress intensity factor, K^{eq}, and r^0 terms coefficients A_{ij} with (i, j = 1,2). In this scheme, the multi-parameter field has been observed to successfully capture the numerical stress component data around the crack tip. The parameter K^{eq} is employed to capture the asymptotic $r^{-1/2}$ field effects and has been invoked in the earlier studies in the literature primarily under fatigue loading in which case the principal axes of the stress field is subjected to changes in effect of cyclic plasticity [49,50]. On that basis, the cyclic plasticity effects around the crack tip resemble the transformation induced stress modifications as principal stress directions also exhibit change with the evolution of martensitic volume fraction, ξ. Following this rationale, the variation of K^{eq} parameter has been shown to strongly depend on the crack angle α. The results lead to the fact that K^{eq} decreases with increasing α indicating that the driving forces around the crack tip suppressed with the promoted sliding mode (Mode II).

Subsequently, the effects of hardening modulus H, transformation strain, ϵ_L, transformation start stress S_{MS}, transformation end stress S_{MF}, on crack tip stress triaxiality, Q, of are quantified in detail for NiTi. Stress triaxiality, Q, is a parameter dependent on the mean stress levels; with transformation S_m and without any transformation $(S_m)_{SSY}$, as well as the martensite start stress S_{MS}. The mean stress levels are calculated at a particular radial coordinate of r^* along the crack and depends on J integral. In the present work, as the martensitic transformation induces contour dependent J integrals, the tip value J^{tip} at the crack tip is calculated based on domain integral to determine r^*. On the other hand, in this work, we do note that the domain integral definition has to be modified for SMAs as the potential energy release rate depends on the motion of the crack tip singularity.

According to earlier works by Hutchinson [51], Rice and Rosengren [52], it is pointed out that as the stress triaxiality increases, described by a positive T stress in their discussions, the crack-tip field is likely to be captured by the HRR solution scaled by one parameter: the J integral; which implicitly indicates the presence of a J dominant zone. On the other hand, if stress triaxiality is reduced (means that the T stress gets more negative), the crack-tip fields deviate from HRR solution sharply and J dominance is lost. Thus, the asymptotic fields surrounding the crack tip can not be specified in detail by solely HRR fields. Therefore, utilizing T stress to quantify the triaxiality of the crack-tip stress state and using the J integral (obtained from finite element model based on the actual elastic-plastic deformation field) provides a two-parameter fracture mechanics theory to describe Mode I and mixed mode of an elastic-plastic crack-tip stresses in plane strain. Noting that the presence of martensitic transformation modifies the stress field and therefore introduces significant changes from single parameter fracture mechanics, in the current study the behavior of stress triaxiality effect is focused for SMAs.

Based on this motivation, stress triaxiality parameter denoted by Q is adapted to the present problem within the presence of martensitic transformation strain. O'Dowd and Shih approach is adopted for the calculation of the triaxiality parameter around crack tip at a particular location r^*.

They proposed a definition of stress triaxiality, named as Q, which is the normalized difference of hydrostatic mean stresses generated by fully yielding conditions (S_m) and linear elastic fracture mechanics solution with denoted small scale yielding $(S_m)_{SSY}$ that is driven by stress intensity factor, K [48]. Subsequently, Henry and Luxmoore employed Q parameter as a ductile fracture parameter for large plastic deformation [46]. They stated that the extent of maximum plastic strain and triaxiality parameter Q value exhibit inverse proportion for center edge crack samples. On the other hand, Bao et al. showed that the pronounced constraint effect following the plastic necking exhibits an opposite trend in aluminum alloys, such that the triaxiality values are promoted. This shows that the presence of necking instability changes the variation of parameter Q with plasticity.

In the present work, this definition is tailored for the martensitic transformation by replacing the normalization factor of yield strength Sy with martensitic transformation start stress, S_{MS}. As the data extracted from ABAQUS is not continuous, a 10 x 10 element set is formed around the crack tip and the collected nodal data are employed create a closed-form regression fit function of independent stress components $\{S_{11}, S_{22}, S_{12}\}$ with respect to θ and r coordinates employing MATLAB method lsqnonlin which depends on nonlinear least square regression. In fitting scheme, both asymptotic $r^{-1/2}$ and r^0 terms are included with their corresponding factors of K^{eq} and A_{ij} where i, j = 1, 2. As can be seen in the results presented in Chapter 5, the values of K^{eq} decrease with increasing crack angle α, on the other hand the parameters A_{ij} exhibit a more complex response. At this stage, it is emphasized that A_{ij} terms are of significant value and can not be neglected. The solution procedure clarifies that using only T stress component is not sufficient to fully describe the stress fields generated around the crack tips in SMAs. The hardening modulus, H, is observed to have an effect on K^{eq} not smaller than 5%. To this end, not only the transformation start stress is important, but also the hardening modulus H also plays a role in K^{eq} values. Similarly A_{11} values are sensitive to H values. A_{22} values exhibit considerable drop with promoted hardening. These indicate that higher order radial terms other than asymptotic $r^{-1/2}$ needs to be elaborated in quantification of stress field around crack tip in the NiTi SMA.

The stress triaxiality parameter Q varies with only slightly in negative regime with hardening modulus H as presented in Chapter 6. This effect is attributed to the completion of the martensitic transformation at the tip and therefore the elastic stresses generated in martensitic phase govern on the tip zone suppressing the contribution of H.

Another effect to be considered for the stress triaxiality, Q, constraint in SMAs is obviously martensitic transformation strain, ϵ_L. In Chapter 6, ϵ_L is varied between 0.04 to 0.08 by 0.02 increments and it Q exhibits a minor increase with ϵ_L. This trend is associated with the martensitic volume fraction, ξ evolution such that as ϵ_L increases, the constant far-field stress work can transform smaller levels of austenite to martensite completely. Thus, the constraint effect owing to elastic stresses persist for larger ϵ_L. This is reflected as a slight change in Q values considering the high stress gradient around the crack tip region. The values of Q are still in negative regime owing the relaxation effect of martensitic transformation.

The transformation start stress level, namely S_{MS}, play a critical role in stress triaxiality Q as shown in section 6.4 . An increase in S_{MS} from 300 MPa to 400 MPa, promotes Q from -1.295 to -0.146. This is an indication of pronounced crack tip constraint and it is related with the suppressed martensitic transformation by increasing the start stress barrier effect. On the other hand, there is no significant increase of constraint if S_{MS} changed from 400 MPa to 500 MPa. This saturation trend implies the martensitic transformation extent around the crack tip has already been highly impeded with the amplifying effect of high stress gradients. Therefore, increasing S_{MS} further has no effect in practice and the material behaves almost like an linear elastic austenite.

Lastly, the contribution of martensite finish stress level, S_{MF} on stress triaxiality Q is elaborated in section 6.5. As the results indicate S_{MF} has a negligible role in changing the crack tip constraint. To this end, the stress field in the tip zone exceeding S_{MF} acts as a linear elastic martensite phase and any transformation induced stress relaxation effects tend to vanish with the accumulation of linear elastic stresses.

8. CONCLUSION

In this dissertation, two parameter characterization of edge cracked NiTi shape memory alloy under plane strain conditions are elaborated using finite element analysis. Single edge notch specimen geometry of NiTi rectangular plate subjected to constant tensile far-field stress field is examined for a set of crack angles α varying as $\{0^o, 10^o, 20^o, 30^o\}$. Therefore, both pure Mode I and mixed mode configurations are analyzed. As a novel step, both asymptotic $r^{-1/2}$ and the following r^0 terms are employed in stress field expansions. Meanwhile the asymptotic term $r^{-1/2}$ is governed by K^{eq}, the higher order term r^0 is governed by A_{ij} where i,j varies from 1 to 2 in conjuction with stress component S_{ij}. In order to generate the governing terms, nonlinear least square regression analyses are conducted with high accuracy. This acts as a comprehensive approach in adapting multi-parameter fracture mechanics in SMAs.

The results can be clustered into two primary groups: (i) the effects of $r^{-1/2}$ and r^0 terms on the stress fields; (ii) the contributions of hardening modulus H, the transformation strain extent ϵ_L, the martensite start and end stresses, namely S_{MS} and S_{MF}. Among these items, the factors A_{ij} governing on r^0 is shown to be of significant magnitude. Conventional two parameters fracture mechanics dealing with only T stress component for r^0 term is observed to be insufficient as other terms such as A_{11}, A_{12} $(= A_{21})$ and A_{22} are substantial in magnitude. To this end, any effort to characterize the stress field governing around the crack tip in SMA NiTi is to consider these high order terms.

Among the material parameters, the hardening modulus H, the transformation strain ϵ_L and the martensite start stress S_{MS} promote crack tip constraint under constant applied far-field stress. This behavior confirms that any material parameter change suppressing the extent of martensitic transformation, obviously promotes the crack tip constraints. On the other hand, the martensite finish stress S_{MF} exhibits no significant effect on the crack tip constraint of SMA NiTi in our simulation results.

As a last remark, our study shows that further analyses are necessary to contemplate on the necking effects. As during necking the stress states change significantly and additional radial constraints come in to play, the results presented in this work are not able to capture the crack tip stress field in case of necking. To this end, large deformation and rotation effects are to be incorporated in any modelling efforts for NiTi SMA in presence of necking.

REFERENCES

1. Salman, O., A. Finel, R. Delville, D. Schryvers and K. Luo, "The Role of Phase Compatibility in Martensite", *Journal of Applied Physics*, Vol. 111, No. 10, 2012.

2. Worden, K., W. A. Bullough and J. Haywood, *Smart Technologies*, World Scientific, 2003.

3. Lecce, L. and A. Concilio, *Shape Memory Alloy Engineering: For Aerospace, Structural and Biomedical Applications*, Butterworth-Heinemann an Imprint of Elsevier, 2021.

4. Lagoudas, D. C. and P. Kumar, *Shape Memory Alloys: Modeling and Engineering Applications*, Springer, 2008.

5. Bhattacharya, K., "Self-Accommodation in Martensite", *Archive for Rational Mechanics and Analysis*, Vol. 120, No. 3, pp. 201–244, 1992.

6. Harrison, J. D. and D. E. Hodgon, *Shape Memory Effect in Alloys*, Plenum Publisher, 1975.

7. Stalmans, R., J. V. Humbeeck and L. Delaey, "The Two Way Memory Effect in Copper Based Shape Memory Alloys—Thermodynamics and Mechanisms", *Acta Materialia*, Vol. 40, No. 11, pp. 2921–2931, 1992.

8. Ziolkowski, A., *Pseudoelasticity of Shape Memory Alloys: Theory and Experimental Studies*, Butterworth-Heinemann an Imprint of Elsevier, 2015.

9. Choudhary, S., S. Kumarmodi and B. N. Roy, "Martensitic Transformation of Polycrystalline Shape Memory Alloy", *International Journal of Trend in Research and Development*, Vol. 4, No. 2, pp. 6–9, 2017.

10. Lexcellent, C., *Shape-Memory Alloys Handbook*, ISTE, 2013.

11. Wayman, C. M., "Shape Memory and Related Phenomena", *Progress in Materials Science*, Vol. 36, pp. 203–224, 1992.

12. Kumar, P., P. B. Entchev and D. C. Lagoudas, "Thermomechanical Characterization of SMA Actuators Under Cyclic Loading", *ASME International Mechanical Engineering Congress*, pp. 15–21, 2003.

13. Liu, Y. and P. McCormick, "Factors Influencing the Development of Two-Way Shape Memory in NiTi", *Acta Materialia*, Vol. 38, No. 7, p. 1321–1326, 1990.

14. Lu, Z. and G. Weng, "Martensitic Transformation and Stress-Strain Relations of Shape-Memory Alloys", *Journal of The Mechanics and Physics of Solids*, 1997.

15. Otsuka, K. and C. M. Wayman, *Shape Memory Materials*, Cambridge University Press, 1998.

16. Hamid, N. A. and A. Adnan, "Cyclic Tensile of Refurbish NiTi Reinforcement Bar for Seismic Mitigation", *IOP Conference Series: Materials Science and Engineering*, 2019.

17. Barenblatt, G. T., "On Some Basic Ideas of the Theory of Equilibrium Crack, Forming During Brittle Fracture", *Problems of Continuum Mechanics*, pp. 21–38, 1961.

18. Griffith, A. A., "The Phenomena of Rupture and Flow in Solids", *Philosophical Transactions*, Vol. 221, pp. 163–198, 1920.

19. Inglis, C. E., "Stresses in Plates Due to the Presence of Cracks and Sharp Corners", *Transactions of the Institute of Naval Architects*, Vol. 55, pp. 219–241, 1913.

20. Irwin, G., "Fracture Dynamics", *American Society for Metals*, pp. 147–166, 1948.

21. Orowan, E., “Fracture and Strength of Solids”, *Reports on Progress in Physics*, Vol. 12, No. 1, p. 185, 1948.

22. Westergaard, H. M., “Bearing Pressures and Cracks”, *Journal of Applied Mechanics*, Vol. 6, No. 2, pp. 49–53, 1939.

23. Williams, M. L., “Stress Singularities Resulting from Various Boundary Conditions in Angular Corners of Plates in Extension”, *Journal of Applied Mechanics*, Vol. 19, No. 4, pp. 526–528, 1952.

24. Williams, M. L., “On the Stress Distribuion at the Base of a Stationary Crack”, *Journal of Applied Mechanics*, Vol. 24, pp. 109–114, 1957.

25. Anderson, T. L., *Fracture Mechanics: Fundamentals and Application*, CRC Press, 2005.

26. Dugdale, D. S., “Yielding of Steel Sheets Containing Slits”, *Journal of the Mechanics and Physics of Solids*, Vol. 8, No. 2, pp. 100–104, 1960.

27. Rice, J. R., “A Path Independent Integral and the Approximate Analysis of Strain Concentration by Notches and Cracks”, *Journal of Applied Mechanics*, Vol. 35, No. 2, pp. 379–386, 1968.

28. Banks, T. M. and A. Garlick, “The Form of Crack Tip Plastic Zones”, *Engineering Fracture Mechanics*, Vol. 19, No. 3, pp. 571–581, 1984.

29. Cherepanov, G. P., *Mechanics of Brittle Fracture*, English Translation: Mcgraw-Hill, 1979.

30. Narasimhan, R. and A. J. Rosakis, “Three Dimensional Effects Near a Crack Tip in a Ductile Three Point Bend Specimen, Part I: A Numerical Investigation”, *Division of Engineering and Applied Science*, Vol. 57, No. 3, pp. 607–617, 1990.

31. Rice, J. R., “Some Remarks on Elastic Crack-Tip Stress Fields”, *International Journal of Solids and Structures*, Vol. 8, No. 6, pp. 751–758, 1972.

32. Barsom, J. M. and S. T. Rolfe, *Fracture and Fatigue Control in Structures: Applications of Fracture Mechanics*, American Society for Testing and Materials, 2006.

33. Larsson, S. G. and A. Carlsson, “Influence of Non-Singular Stress Terms and Specimen Geometry on Small-Scale Yielding at Crack Tips in Elastic-Plastic Materials”, *Journal of the Mechanics and Physics of Solids*, Vol. 21, No. 4, pp. 263–277, 1973.

34. Kirk, M. T., R. H. Dodds and T. L. Anderson, “A Framework to Correlate a/W Ratio Effects on Elastic-Plastic Fracture Toughness”, *Internal Journal of Fracture*, Vol. 48, pp. 1–22, 1991.

35. Shih, C. F. and N. P. O’Dowd, “Two-Parameter Fracture Mechanics: Theory and Applications”, *American Society for Testing and Materials*, pp. 21–47, 1994.

36. Shih, C. F., N. P. O’Dowd and M. T. Kirk, “”A Framework for Quantifying Crack Tip Constraint”, *American Society for Testing and Materials*, pp. 2–20, 1992.

37. Gollerthan, S., M. L. Young, A. Baruj, J. Frenzel, W. W. Schmahl and G. Eggeler, “Fracture Mechanics and Microstructure in NiTi Shape Memory Alloys”, *Acta Materialia*, Vol. 57, No. 4, pp. 1015–1025, 2009.

38. Maletta, C., A. Falvo, F. Furgiuele and A. Leonardi, “”Stress-Induced Martensitic Transformation in the Crack Tip Region of a NiTi Alloy”, *Journal of Materials Engineering and Performance*, Vol. 18, No. 5, p. 679–685, 2008.

39. Maletta, C. and F. Furgiuele, “Analytical Modeling of Stress-Induced Martensitic Transformation in the Crack Tip Region of Nickel Titanium Alloys”, *Acta Materialia*, Vol. 58, No. 1, pp. 92–101, 2010.

40. Broek, D., *Elementary Engineering Fracture Mechanics*, Kluwer Academic, 1986.

41. Young, M. L., M. F. Wagner, J. Frenzel, W. W. Schmahl and G. Eggeler, “Phase Volume Fractions and Strain Measurements in an Ultrafine-Grained NiTi Shape-Memory Alloy During Tensile Loading”, *Acta Materialia*, Vol. 58, No. 7, pp. 2344–2354, 2010.

42. Maletta, C. and F. Furgiuele, “Analytical Modeling of Stress-Induced Martensitic Transformation in the Crack Tip Region of Nickel–Titanium Alloys”, *Acta Materialia*, Vol. 58, No. 1, pp. 92–101, 2010.

43. Irwin, G., “Plastic Zone Near a Crack and Fracture Toughness”, *Proceedings of the Seventh Sagamore Ordnance Materials Research Conference*, pp. 63–78, 1960.

44. Tada, H., P. C. Paris and G. Irwin, *The Stress Analysis of Cracks Handbook*, American Society of Mechanical Engineers, 2000.

45. Henry, B. S. and A. Luxmoore, “The Stress Triaxiality Constraint and the Q-Value As a Ductile Fracture Parameter”, *Engineering Fracture Mechanics*, Vol. 57, No. 4, pp. 375–390, 1997.

46. Bao, Y. and T. Wierzbicki, “On the Cut-Off Value of Stress Triaxiality for Fracture”, *Engineering Fracture Mechanics*, Vol. 72, No. 7, pp. 1049–1069, 2005.

47. O’Dowd, N. P. and C. F. Shih, “Family of Crack-Tip Fields Characterized by a Triaxiality Parameter – I. Structure of Fields”, *Journal of the Mechanics and Physics of Solids*, Vol. 39, No. 8, pp. 989–1015, 1991.

48. Hutchinson, J. W., “”Singular Behaviour at the End of a Tensile Crack in a Hardening Material”, *Journal of Mechanics and Physics of Solids*, Vol. 16, No. 1, pp. 13–31, 1968.

49. Rice, J. R. and G. F. Rosengren, “Plane Strain Deformation Near a Crack Tip in a Power-Law Hardening Material”, *Journal of Mechanics and Physics of Solids*, Vol. 16, No. 1, pp. 1–12, 1968.